Diapycnal and along isopycnal mixing, estimated from the tracer release experiment, at the North Atlantic oxygen minimum zone

Dissertation
zur Erlangung des Doktorgrades
der Mathematisch-Naturwissenschaftlichen Fakultät
der Christian-Albrechts-Universität zu Kiel

vorgelegt von

Donata Banyte

Kiel 2012

Erster Gutachter:	Prof. Dr. M. Visbeck
Zweiter Gutachter:	Prof. Dr. R. Greatbatch
Tag der mündlichen Prüfung:	23.01.2013
Zum Druck genehmigt:	05.02.2013
Gez.:	Prof. Dr. rer. nat. W. J. Duschl, Dekan

Eidesstattliche Versicherung

Ich versichere an Eides statt, dass ich die von mir vorgelegte Dissertation - abgesehen von der Beratung durch meinen Betreuer - selbstständig und ohne unerlaubte Hilfe angefertigt habe und alle benutzten Quellen und Hilfsmittel vollständig angegeben habe. Die Zusammenarbeit mit anderen Wissenschaftlern habe ich kenntlich gemacht. Die Arbeit ist unter Einhaltung der Regeln guter wissenschaftlicher Praxis der Deutschen Forschungsgemeinschaft entstanden. Ferner habe ich weder diese noch eine ähnliche Arbeit an einer anderen Abteilung oder Hochschule im Rahmen eines Prüfungsverfahrens vorgelegt, veröffentlicht oder zur Veröffentlichung vorgelegt.

Kiel, 12.11.2012 Donata Banyte

Statement of Co-authorship

Chapters 2-3: These chapters were prepared as scientific manuscripts as identified at the beginning of each chapter. In the case of each of these two chapters the candidate had the primary responsibility for constructing the methods of dealing with the data and performing the numerical calculations. The supervisors Prof. Martin Visbeck and Dr. Toste Tanhua assisted the candidate with the interpretation of the results.

Chapters 4: The candidate performed oxygen flux and flux divergence computations, did uncertainty analysis, checked the influence of different spatial averaging methods to the final results. The candidate assisted Dr. Tim Fischer with the interpretation of the results and revision. Dr. Tim Fischer wrote the manuscript, did comparison of diapycnal mixing coefficients, estimated from microstructure and vmADCP data, with the mixing coefficient obtained from the tracer release experiment. Dr. Tim Fischer also modified all of the figures for the publication.

Martin Visbeck

Zusammenfassung

Die Ergebnisse eines von 2008 bis 2010 durchgeführten Guinea Upwelling Tracer Release Experiments (GUTRE) wurden benutzt, um die diapyknische Vermischung und das laterale Verteilen in der Thermokline des tropischen Nordatlantiks zu bestimmen. Hauptaufgabe dieser Arbeit war die Untersuchung der Versorgungswege des Sauerstoffs am oberen Rand der nordatlantischen Sauerstoffminimumzone.

Die gemittelten diapyknischen Mischungskoeffizienten wurden für ein Tracergebiet berechnet, welches 30 Monate untersucht wurde. Die starke Schichtung im Gebiet des Tracers, wenn die diapyknische Streuung dieses erforscht werden soll, hat die Benutzung der Advektions-Diffusions-Gleichung in Dichtekoordinaten mit Schichtdickenmittelung vorteilhaft erscheinen lassen. Verglichen mit Ergebnissen des North Atlantic Tracer Release Experiment (NATRE), welches ca. 15° nördlicher stattgefunden hat, waren die Abschätzungen der vertikalen Vermischung ca. 30% kleiner. Im Allgemeinen sagen Modelle, welche das Zusammenspiel von internen Wellen untersuchen, eine verringerte Vermischung aufgrund von brechenden internen Wellen in niederen Breiten voraus. Die GUTRE-Ergebnisse sind grösser als die parametrisierten Ergebnisse in niederen Breiten in der Region 4°N−12°.

Der mittlere isopyknische Vermischungskoeffizient wurde über das Wachstum des zweiten Moments der Tracer-Wolke berechnet. Die zonale Komponente der lateralen Vermischung ist mehr als zweimal grösser als die meridionale Komponente. Das spiegelt den “Dehnungs-Effekt” der, im tropischen Atlantik vorherrschenden, zonalen Strmungsbnder (Jets) wider. Die Anwendung eines konzeptionellen Jet-Modells erlaubte die Bestimmung der mittleren zonalen Geschwindigkeiten,

welche eine Erhöhung der Vermischung in zonale Richtung zur Folge haben. Zusätzlich wurde der effektive Vermischungskoeffizient bestimmt, welcher heraushebt, dass die zonalen Jets den Tracer nicht nur in zonale Richtung ausdehnen, sondern auch, dass die Vermischung durch Erhöhen der Tracergradienten erhöht wird. Die Unsicherheit der Abschätzung wurde mit einem hochaufgelösten Ozeanzirkulationsmodell bestimmt, in dem ein künstlicher Tracer freigesetzt wurde.

Im Endeffekt erlaubt ein einzigartiger Datensatz, bestehend aus vertikalen Sauerstoffprofilen in der Sauerstoffminimumzone und hochaufgelöste Abschätzungen der diapyknischen Vermischung, eine aussagekräftige Bestimmung des diapyknischen Eintrages von Sauerstoff durch den oberen Rand der Sauerstoffminimumzone. Im Vergleich zu einem Modell, welches den Sauerstoffverbrauch mit der Tiefe bestimmt, wurde der Beitrag des diapyknischen Sauerstoffeintrags als ungefähr halb so gross, wie der des lateralen Eintrags, berechnet. Desweiteren wurde in der Region der Sauerstoffminimumzone ein weiteres flaches Sauerstoffminimum in ca. 100 m Tiefe gefunden. Dieses Minimum zeigt, dass kein direkter vertikaler Nettosauerstofffluss von der Oberflächenschicht zur Sauerstoffminimumzone existiert. Der komplette Eintrag von Sauerstoff wird deswegen mit einem Eintrag über entferntere Wege in Verbindung gebracht.

Abstract

A deliberate Guinea Upwelling Tracer Release Experiment (GUTRE) in $2008-2010$ was used to study diapycnal mixing and lateral stirring in the thermocline of tropical northeastern Atlantic. The ultimate goal of this work was to investigate oxygen supply pathways at the upper boundary of North Atlantic oxygen minimum zone.

The mean diapycnal mixing coefficients were computed for a tracer patch integrated over 30 months. The strong variation of stratification in the tracer occupied area offered the advantage of using the advection-diffusion equation in isopycnal coordinates with the thickness-weighted averaging, when analyzing the diapycnal tracer spread. Overall, the vertical mixing estimates were found about 30% smaller than estimates in North Atlantic Tracer Release Experiment (NATRE), performed about 15° to the north from our experiment. In general, the internal wave-wave interaction models predict reduced mixing from the breaking of internal waves at low latitudes. Thus, GUTRE results are larger than parametrized by the low latitude of the site ($4°\text{N}-12°\text{N}$).

The mean isopycnal mixing coefficient was estimated by computing the growth of the second moment of a cloud of tracer. The zonal component of lateral mixing was found more than two times larger than the meridional component. The finding reflects the stretching effect of zonal jets prevalent in the tropical Atlantic Ocean. The application of conceptual jet model allowed to evaluate the mean zonal jet velocities which cause an enhancement of mixing in zonal direction. Additionally, the effective mixing coefficient was computed which indicated that zonal jets do not merely stretch the tracer patch in zonal

directions, but increase mixing by increasing tracer gradients. The uncertainties of the estimates were inferred from synthetic particle release using a high resolution ocean circulation model.

Finally, a large database of vertical oxygen profiles in oxygen minimum region and high precision diapycnal mixing estimates allowed for a good estimate of diapycnal oxygen supply through the upper boundary into the oxygen minimum zone. In comparison to conceptual model of oxygen consumption with depth, the diapycnal oxygen supply was estimated to be as large as about half of the lateral oxygen supply. Furthermore, in the oxygen minimum region, the separate shallow oxygen minimum was found at about 100 m depth. The finding indicates that there is no direct net vertical oxygen flux from the surface layer into the oxygen minimum zone. All of oxygen supply, hence, is associated with remote pathways.

Contents

Acknowledgements

And I would like to thank several people who helped to come to the finish line after three years of PhD:

Thank you, Martin and Toste, for incredible ability to catch the essence out of sometimes entangled strings of scientific thoughts, to offer hundreds of suggestions for improvement, for seeing not only difficulties and 'things-to-do', but also appreciating the work done, for encouragement to try the things out and so fostering self-confidence for the research.

Thank you, Richard, for showing interest on the work progress, for offering slightly different point of view or a new reference, which at least once led to a breakthrough.

Thank you, Marcus, for eagerly listening and discussing even the strangest of my scientific ideas, paving the way into better understanding.

Thank you, my colleagues: Rebecca, Johannes, Sven, Michael, and Sandra, for creating a great working atmosphere in the office, for sharing the knowledge and many discussions, but also introducing into subtle German ways and language.

Thank you, PO secretary, Nadira and Sigrun, for helping to find the way in the woods of administrative paperwork.

Thank you, Jenny, Geraldine, Wanling, Jin and Steffi , for keeping a really interdisciplinary and multicultural spirit in a group, for being a great company during many lunches eaten together, and for organizing many great social after-work events.

CONTENTS

Chapter 1

Introduction

1.1 Mixing in the ocean

The transport of tracers in the ocean is typically described by the mean advection and turbulent mixing. In the stratified ocean, however, the scales of the processes are highly depend on the spatial direction with respect to density surfaces. In the open ocean, where turbulent mixing across density layers is mainly controlled by breaking of internal waves at the scales of several meters, along the density layers, the turbulent mixing is carried by eddies at the scales of up to several hundreds of kilometers. As a result, the gradients of the tracers are much weaker along density surfaces than across them.

An efficient tracer mixing along isopycnals is an interplay between advective stirring and small scale mixing. Stirring stretches tracer parcells, increasing the tracer gradients, while small scale mixing constantly reduces the gradients leading to irreversible mixing of the tracer [*Eckart*, 1948]. There are many scales across which mixing happens: from molecular mixing and small scale instabilities to mesoscale eddies of several hundreds of kilometers in diameter. Observing the large scale spread of the tracer offers an integrated over time perspective on the mixing process, where complicated interaction of advection and turbulent mixing can be parametrized by a single mixing coefficient. Often though, as well as in this thesis, mixing coefficients are computed for meridional and zonal directions: across and along the prevelant mean zonal flow. The mixing by mesoscale eddies

is parametrized by eddy diffusion coefficient of the order of 10^3 m^2 s^{-1}.

The small scale mixing of tracers across isopycnals in the subsurface is thought to be attributed mainly to the breaking of internal waves or to double diffusion processes. Double diffusion describes the mixing when warm and salty waters overly colder and fresher waters. The instability arrises from a difference in the diffusivities for heat and salt [e.g., *Schmitt*, 1994]. The several decades of observations of small scale instabilities in the ocean interior have shown that diapycnal mixing events are random, spontaneous, and locally confined. However, observing the tracer patch spread across isopycnals over time offers an integrated result of many local diapycnal mixing events. After about 20 to 30 months the diapycnal extent of the tracer is found to be very similar between the tracer profiles taken hundreds of kilometers apart (Chapter 2). The small scale mixing is parametrized by diapycnal diffusion coefficient of the order of 10^{-5} m^2 s^{-1}.

1.1.1 Measuring mixing in the ocean

Diapycnal mixing in the ocean, since already '70s, has been inferred from microstructure shear and temperature measurements which show instantaneous and locally confined turbulent mixing events [e.g., *Gregg et al.*, 1973; *Osborn*, 1980; *Schafstall et al.*, 2010; *Toole et al.*, 1994]. Diapycnal mixing can also be inferred from measurements of vertical shear at scales of tens of meters using lowered ADCP [e.g., *Kunze et al.*, 2006], or from measurements of strain using Conductivity, Temperature, Depth (CTD) sensor data [e.g., *Kunze et al.*, 2006; *Wu et al.*, 2011]. However, the above mentioned methods rely on the parametrizations relating internal wave characteristics and dissipation rates, or diapycnal diffusivity, and hence, are subject to approximations [*Gregg et al.*, 2003; *Kunze et al.*, 2006]. The resulting uncertainty of such estimates is at least of a factor of two [*Polzin et al.*, 1995].

Lateral mixing in the ocean is inferred from observations in also a number of different ways, for example: 1) from observations of instantaneous velocity and tracer, e.g. temperature, fluctuations using mooring data [e.g., *Bryden and Heath*, 1985], 2) from observations of dispersion of floats and drifters [e.g., *Davis*, 1991; *LaCasce*, 2008], 3) by using 2D non-divergent flow derived from altimetry

data and driving an advection-diffusion equation for idealized tracers [*Klocker et al.*, in press; *Marshall et al.*, 2006], 4) by tracer release experiments [*Ledwell et al.*, 1998]. The advantage of tracer release experiments is that the method provides time and space integrated mixing coefficients; the spread of a cloud of the tracer is analyzed both in vertical and in horizontal, where various mixing processes leave the trace in the spatial tracer distribution.

The technological challenges of the tracer release experiments are however significant, such as the accurate injection of the tracer, detection of the tracer concentrations months after the injection in the long-term experiments, or large sampling area coverage [*Watson and Ledwell*, 2000]. As a result, the first open ocean tracer release experiment,the North Atlantic Tracer Release Experiment (NATRE), was performed in 1992 southwest from the Canary islands. The depth of the experiment and stratification conditions were similar between NATRE and Guinea Upwelling Tracer Release Experiment performed about 15° southward. For this reason, the results of the two experiments were often compared in this thesis. In the years following NATRE, two more large scale open ocean tracer release experiments were performed: the Brazil Basin tracer release experiment at a depth of about 4000 m to observe the mixing near rough topography, and the Diapycnal and Isopycnal Mixing Experiment in the Southern Ocean (DIMES) at a depth of about 1500 m to observe the mixing at mid-depth of strongly wind-driven Antarctic Circumpolar Current.

The Guinea Upwelling Tracer Release Experiment was performed in the special location of the tropical ocean, where very low oxygen concentrations are observed. The motivation of all three individual studies described in chapters 2-4 is finding the relative contribution of lateral and diapycnal oxygen supply pathways into the region of low oxygen content. A diapycnal supply of oxygen by small diapycnal mixing is of the similar order as lateral supply, because the same variation of oxygen concentrations are distributed only over several hundreds of meters in the vertical, as compared to the thousands of kilometers in the horizontal [*Brandt et al.*, 2010]. The introduction further briefly reviews: 1) the low oxygen environments and necessary conditions for them to appear, 2) observed and modeled oceanic deoxygenation and its consequences, and finally 3) the need to know vertical and lateral mixing for the future projections of the fate of oxygen

minimum zones in the warming climate.

1.2 Oxygen minimum zones

The low oxygen environments are called Oxygen Minimum Zones (OMZ). They often occur in coastal waters, or at the bottom of closed basins, such as the Black sea and the Baltic sea (review by *Keeling et al.* [2010]). However, it is the open ocean OMZs that have the largest volume and global importance. They are situated at the eastern boundaries of the tropical oceans and in the depth range of 100 to 900 m [*Karstensen et al.*, 2008]. Defined by the oxygen level of 90μmol kg^{-1}, a stressful environment for most of marine macro-organisms, the total volume of OMZs in relation to the global oceanic volume is about 3% and the surface area about 8% [*Karstensen et al.*, 2008]. Different oceans show different intensities of oxygen minimum: in the Pacific, levels of as low as 0.1μmol kg^{-1} are reached, in the Indian ocean - about 0.3μmol kg^{-1}, in the South Atlantic - about 20μmol kg^{-1}, while in the North Atlantic concentrations are higher, at about 40μmol kg^{-1}. Hence, the Pacific Ocean has the most intense and largest open ocean OMZs in the world. Yet, the largest negative oxygen trend was observed in the reasonably well ventilated North Atlantic OMZ [*Stramma et al.*, 2008], which is the focus of the thesis.

The oxygen minimum zones are formed as a consequence of weak ventilation and significant oxygen consumption [*Sverdrup*, 1938; *Wyrtki*, 1962]. In general, oxygen enters the ocean at the surface by air-sea gas exchange or is produced at the surface by marine phytoplankton as a result of photosynthesis reaction. When water is subducted to the subsurface, oxygen is constantly consumed by all the living organisms, mainly by bacteria. In the very simplified model, oxygen content anywhere in the ocean can be described by: 1) the oxygen levels at the water mass formation site; 2) the time elapsed since water left the surface; and 3) the oxygen consumption rate. All three conditions explain why oxygen levels are high in the shallow part of the ocean as well as in the deep part, while oxygen minimum zones form at their boundary, at about 500 m depth.

For example, the deep waters are the oldest and they form at high latitudes, slowly filling the deep ocean basins as part of the deep circulation cycle. The ages

of the water at the bottom of the Atlantic Ocean reaches 500 years, while in the Pacific they are even older, on the order of millennium [*England*, 1995]. However, even in the Pacific the bottom waters have relatively large oxygen concentrations of mostly more than 150μmol kg^{-1}. One of the reasons is the higher oxygen solubility at the cold surface waters of high latitudes, but more importantly, the oxygen consumption rates are very low at greater depths. Oxygen consumption decreases with depth by a factor of 10-50 between 100-1000 m [*Feely et al.*, 2004; *Jenkins*, 1987; *Karstensen et al.*, 2008; *Martin et al.*, 1987].

The shallow thermocline waters, on the other hand, are ventilated by so called subtropical cell circulation: a shallow, meridional circulation cell consisting of subtropical subduction, equator-ward advection of cool subsurface water into the tropics, upwelling at the equator, and poleward advection of warm surface water back to mid-latitudes [e.g., *McCreary and Lu*, 1994]. They extend to the depth of about 1000 m in the subtropics, but only to about 300 m at the equator. Moreover, the total volume involved in the shallow oceanic circulation is only about 10%. Volumetrically small, the thermocline waters are well-ventilated and young. However, being shallow, the oxygen consumption rates are also much larger than in the deep ocean. In general, ventilation is strong enough to compensate for the higher oxygen consumption and oxygen levels are large in the shallow part of the ocean. However, in special locations in the thermocline, where ventilation is exceptionally weak, but oxygen consumption rates are higher, the necessary conditions appear to create the low oxygen environments.

In the Atlantic and the Pacific oceans, the oxygen minimum zones form in the subsurface layers in relatively stagnant cyclonic gyres at the eastern side of the tropical basins. They are situated in the so-called "shadow zones" of the subtropical gyres [*Luyten et al.*, 1983]. The return flow of subtropical gyres in the thermocline are deflected to the southwest following the basic principles of thermocline circulation. Essentially, there is no meridional flow from the subtropics to the tropics and the transport is limited to the complicated system of zonal currents, i.e. the ventilation by long pathways. The two most pronounced eastward flowing current branches are the North Equatorial Undercurrent (NEUC) located at about 5°N and the northern branch of the North Equatorial Countercurrent (nNECC) located at about 9°N [*Stramma et al.*, 2005]. They transport

oxygen-rich waters from the east side of the basin to the North Atlantic OMZ [*Brandt et al.*, 2008]. The oxygen supply pathways, however, are not limited to just the mean advection; the turbulent mixing plays an equally important role.

1.3 Observed and modeled oceanic deoxygenation

1.3.1 Observed oxygen loss in the ocean

Historical oxygen records are commonly sparse and sporadic as reviewed by *Keeling et al.* [2010]. There are however two stations in the North Pacific, where mid-depth oxygen levels were recorded with annual or better resolution over as long as 50 years: Oyashio current region off Japan [*Ono et al.*, 2001; *Watanabe et al.*, 2003] and Station P in the Alaskan gyre [*Whitney et al.*, 2007]. The records show long term declines of order 7μmol kg^{-1} decade^{-1} superimposed on a bidecadal oscillation. Recently, *Stramma et al.* [2012b] combined a huge database of individual measurements since 1960s to compute the global distribution of linear oxygen trend at 300 m depth. The average over 50°N and 50°S region resulted in -0.6μmol kg^{-1} decade^{-1}. The similar patterns were reported also by *Helm et al.* [2011], who used different data averaging method. His global oxygen decrease was estimated to be 0.4μmol kg^{-1} decade^{-1}. Especially strong decrease in oxygen levels was observed in the oxygen minimum zones. *Stramma et al.* [2012b] reports a negative trend of order 8μmol kg^{-1} decade^{-1} in the tropical oceans. The oxygen minimum zones not only are becoming more intense, but their expansion laterally as well as in the vertical were also reported [*Stramma et al.*, 2010].

The relatively shallow position of oxygen minimum zones and their expansion strongly affect the marine organisms living at their boundaries. Marine macro-organisms show different sensitivity to low oxygen levels, but most of them have lethal threshold of oxygen levels. Fish and crustaceans tend to be the most sensitive [e.g., *Vaquer-Sunyer and Duarte*, 2008]. The expanding oxygen minimum zones therefore compress the habitat of marine macro-organisms into narrower surface layers, where they are susceptible to increased predation and competi-

tion. The reduced diving depth was shown for the tropical pelagic fishes such as marlins, sailfish and tuna [*Prince et al.*, 2006; *Stramma et al.*, 2012a].

Furthermore, the important changes in biogeochemical cycles take place at the oxygen levels, which drop below 20μmol kg^{-1} [*Wright et al.*, 2012]). At such low oxygen concentrations, bacteria instead of using oxygen start to consume organic nitrate (NO_3^-) and nitrite (NO_2^-) in their metabolic reactions and release nitrous oxide (N_2O). Nitrous oxide gas is a powerful greenhouse gas with radiative forcing effect that is about 300 times the effect of CO_2 [*Wright et al.*, 2012]. In total, the ocean emits at least 30% of all natural N_2O to the atmosphere, most of which comes from the oxygen minimum zones [*Naqvi et al.*, 2010]. Moreover, nitrate is a main limiting nutrient for the primary productivity of organic matter and the OMZs are estimated to account for up to 50% of oceanic fixed-nitrogen loss [*Wright et al.*, 2012].

1.4 Sensitivity of ocean models to mixing coefficients

There is no simple answer why the OMZs are observed to be expanding and how they would behave in the future. In a global mean, most of the general ocean circulation models are showing the oxygen decrease in the warming climate [*Matear and Hirst*, 2003; *Schmittner et al.*, 2008]. About 25% of that decrease is a result of the reduction in the solubility of oxygen in warmer water. The rest comes from changes in ocean circulation and biology. In the warming climate, models predict slower ventilation of water-masses, either because of reduced meridional overturning circulation, or because of increased stratification. The changes in stratification, on the other hand, have a biological response. The higher stratification reduces the amount of nutrients reaching the productive surface waters, thus, limiting the primary productivity. When less organic matter is produced at the surface, less is exported to the subsurface, where oxygen consumption rate also drops. Hence, even though higher stratification reduce the vertical oxygen supply, the biological processes counteract. Nonetheless, the models consistently predict that decrease in ventilation, by higher stratification, exceeds the effect

of reduced oxygen consumption [*Bopp et al.*, 2002]. In consequence, most of the general ocean circulation models suggest an overall decrease in oceanic oxygen levels with the warming climate.

The models and observations, however, do not agree on the fate of oxygen minimum zones. Despite observational evidence of intensification and expansion of the zones, most models predict increasing oxygen levels and shrinking volume of the zones [e.g., *Bopp et al.*, 2002; *Matear and Hirst*, 2003]. Several explanations are given for the mismatch between models and observations, such as: 1) the coarseness of the models [*Keeling et al.*, 2010], 2) the need for the more elaborate biogechemical models [*Oschlies et al.*, 2008], 3) reduction of upwelling of deep old waters [*Gnanadesikan et al.*, 2007], but also 4) the sensitivity of the model output to the diapycnal mixing coefficient [*Duteil et al.*, 2011], and 5) the poor representation of zonal jets: oxygen advection pathways to the OMZs [*Keeling et al.*, 2010].

The last two points indicate that the observational turbulent mixing parameters are required for realistic representation of oxygen minimum zones in the models. Even more so, they are required for the future projections of oxygen concentrations in those regions in the warming climate. *Duteil et al.* [2011] have already shown that the simulated extent of marine suboxia is very sensitive to the specific choice of the diapycnal mixing parameters within the range of observational estimates. One of the reasons is that especially large vertical oxygen gradients in oxygen minimum zones, and consequently large vertical oxygen inflow, make a significant contribution to the total oxygen budget. In chapter 4, we estimate about one third of the total oxygen supply coming by vertical pathways. The vertical and lateral inflow of oxygen respond to the changing climate differently: one through changes in the strength of zonal jets and lateral eddy kinetic energy, the other through changes in stratification, where higher stratification corresponds to lower vertical mixing coefficient. In conclusion, the vertical and lateral mixing parameters, and associated differentiation between two oxygen supply pathways, are especially important in the future projections of the fate of oxygen minimum zones.

1.5 The scope of the thesis

The main goal of the thesis is the analysis of oxygen supply into the North Atlantic oxygen minimum zone. During three cruises in the time period of 2008-2010 we extensively surveyed the oxygen minimum region southwards from Cape Verde islands. The tracer release experiment provided with vertical diffusivity and vertical advection estimates integrated over large spatial scales and over long time period. The lateral spread of the tracer was analyzed to estimate the lateral mixing by mesoscale eddies and the mean advection of zonal jets. In addition, a large number of microstructure profiles and shipboard acoustic current measurements were gathered. They allowed for a comparison of three different methods to estimate vertical mixing coefficient. Finally, an extensive database of oxygen profiles collected during the surveys, allowed a good estimate of vertical oxygen supply into the oxygen minimum zone region through the upper boundary. Also, a relative contribution between vertical and lateral oxygen supply pathways was estimated. The thesis is organized as follows:

Chapter 2

Diapycnal diffusivity at the upper boundary of the tropical North Atlantic oxygen minimum zone
Banyte, D., T. Tanhua, M. Visbeck, D. W.R. Wallace, J. Karstensen, G. Krahmann, A. Achneider, L. Stramma, J. Geophys. Res., 117, C09016, 2012

Describes in detail the Guinea Upwelling Tracer Release Experiment (GUTRE) and how the tracer data is prepared to compute mixing coefficients. The study focuses on the vertical mixing coefficient and its variability between the regions. The differences between two coordinate systems, Cartesian and isopycnal, used for the data analysis are discussed.

Chapter 3

Lateral diffusivity from tracer release experiments in the tropical north Atlantic thermocline

Banyte, D., M. Visbeck, T. Tanhua, T. Fischer, G. Krahmann, J. Karstensen, prep. for submition to J. Geophys. Res., 2012

The tracer data, prepared as described in chapter 2, is used to compute the lateral mixing coefficients. The irregular sampling strategy of GUTRE is applied to synthetic tracer releases using either conceptual jet model or general ocean circulation model (FLAME). The comparison of the results obtained using GUTRE sampling strategy with the full field estimates in the model helps to assess the quality of the mixing coefficient estimates in the observations.

Chapter 4

Diapycnal oxygen supply to the tropical North Atlantic oxygen minimum zone

T. Fischer, D. Banyte, P. Brandt, M. Dengler, G. Krahmann, T. Tanhua, and M. Visbeck, submitted to Biogeosciences Disc., October 2012

The mixing coefficients are computed and compared using three methods: from local observations of turbulent small-scale mixing using microstructure profiler and shipboard acoustic current profiler. Then, the mixing coefficients are applied to compute the vertical oxygen supply into the oxygen minimum zone and assess the relative distribution between vertical and lateral oxygen supply pathways.

Chapter 2

Diapycnal diffusivity at the upper boundary of the tropical North Atlantic oxygen minimum zone

D. Banyte, T. Tanhua, M. Visbeck, D. W.R. Wallace, J. Karstensen, G. Krahmann, A. Achneider, L. Stramma, and M. Dengler, *J. Geophys. Res.*, *117*, C09016, 2012

2.1 Abstract

A deliberate tracer release experiment in $2008-2010$ was used to study diapycnal mixing in the tropical northeastern Atlantic. The tracer (CF_3SF_5) was injected on the isopycnal surface $\sigma_\Theta = 26.88$ kg m^{-3}, which corresponds to about 330 m depth. Three surveys, performed 7, 20, and 30 months after the release, sampled the vertically and laterally expanding tracer patch. The mean diapycnal mixing estimate over the entire region occupied by the tracer and the period of 30 months was found to be $(1.19 \pm 0.18) \times 10^{-5}$ m^2 s^{-1}, or, alternatively, $(3.07 \pm 0.58) \times 10^{-11}$ (kg m^{-3})^2 s^{-1} as computed from the advection-diffusion equation in isopycnal coordinates with the thickness-weighted averaging. The latter method is preferable in the regions of different stratification for it yields local diapycnal

mixing estimates varying less with stratification than their Cartesian coordinate counterparts. Results of this study are comparable to the results of the North Atlantic tracer release experiment (NATRE). However, the internal wave-wave interaction models predict reduced mixing from the breaking of internal waves at low latitudes. Thus, the diapycnal diffusivity found in this study is higher than parametrized by the low latitude of the site (4°N−12°N).

2.2 Introduction

Diapycnal fluxes of heat, salt, or other dissolved elements (e.g. nutrients, oxygen) are small in comparison to the contribution from advection and along isopycnal mixing in budgets and mass balances. However, in regions with sluggish lateral circulation, the role of vertical mixing in tracer transport can be significant. Such weak horizontal circulation appears, for instance, in the eastern boundary thermocline of the tropical oceans, so-called "shadow zones" of the subtropical gyres [*Luyten et al.*, 1983]. A recent study by *Brandt et al.* [2010], employing a simple ventilation model, showed that the diapycnal mixing could contribute up to 25% of the total oxygen flux into the oxygen minimum zone located in the tropical northeastern Atlantic thermocline. Therefore, it is important to accurately determine diapycnal diffusivity coefficient in order to quantify its contribution to the ventilation of these "shadow zones" and appropriately represent the vertical transport in ocean models.

Direct measurement of turbulent diapycnal mixing in the open ocean is extremely challenging. Most commonly, it is estimated from microstructure shear and temperature measurements which show instantaneous and locally confined turbulent mixing events [e.g., *Gregg et al.*, 1973; *Osborn*, 1980; *Schafstall et al.*, 2010; *Toole et al.*, 1994]. Diapycnal mixing can be also inferred from measurements of vertical shear at scales of tens of meters using lowered ADCP [e.g., *Kunze et al.*, 2006], or from measurements of strain using Conductivity, Temperature, Depth (CTD) sensor data [e.g., *Kunze et al.*, 2006; *Wu et al.*, 2011]. However, the above mentioned methods rely on the parametrizations relating internal wave characteristics and dissipation rates, or diapycnal diffusivity, and hence, are subject to approximations [*Gregg et al.*, 2003; *Kunze et al.*, 2006]. The resulting

uncertainty of such estimates is at least of a factor of two [*Polzin et al.*, 1995]. However, since turbulent dissipation typically varies over several orders of magnitude in time and space, those derived methods are invaluable in establishing the local variation in diapycnal diffusivity in the ocean.

A more accurate method to estimate the time-averaged diapycnal mixing is the use of tracer release experiments, where a tracer is released on an isopycnal surface and the diapycnal spread of the tracer is documented with time. The vertical tracer expansion includes all different processes contributing to turbulent mixing and yields a diffusivity estimate integrated over long timescales and large space scales. Despite the simple concept, the technological challenges of the tracer release experiments are significant, such as the accurate injection of the tracer, detection of the tracer concentrations months after the injection in the long-term experiments, or large sampling area coverage [*Watson and Ledwell*, 2000].

The first large scale tracer release experiment in the open ocean was performed in May 1992. The experiment was led by Ledwell and Watson in the southeastern part of the subtropical gyre, in the region of 20°N−26°N and 30°W−45°W, and was called the North Atlantic Tracer Release Experiment (NATRE) [*Ledwell et al.*, 1993, 1998]. About 140 kg of the tracer, sulfur hexafluoride (SF_6), was released on an isopycnal surface near 300 m depth and was surveyed over a period of 30 months as it dispersed across and along isopycnal surfaces. During the 30-month time span, the originally 20-km-wide patch had spread 1000 km horizontally and from about 20 m to 150 m vertically, yielding a vertical diffusivity estimate of $(1.7 \pm 0.2) \times 10^{-5}$ m^2 s^{-1}.

NATRE results confirmed the estimates obtained from microstructure or fine-scale shear and strain measurements that turbulent diffusivity in the mid-latitude thermocline is of the order of 10^{-5} m^2 s^{-1} [*Gregg*, 1987; *Kunze and Sanford*, 1996; *Kunze et al.*, 2006]. One to two orders of magnitude larger diapycnal diffusivities have been found near boundaries, especially near rough topography [e.g., *Kunze and Sanford*, 1996; *Munk and Wunsch*, 1998; *St. Laurent and Thurnherr*, 2007]. Topographical enhancement of diapycnal mixing was also confirmed by the second large-scale tracer release experiment in the abyssal Brazil basin (BBTRE) on the western flank of the Mid-Atlantic Ridge [*Ledwell et al.*, 2000; *Polzin et al.*, 1997]. Furthermore, several studies show that diapycnal diffusivity varies with latitude

		Survey	Date	No.(all)	No.(tracer)
Injec.	—	MSM08/1	Apr 23 - Apr 26, 2008	—	—
I	7 months	MSM10/1	Oct 31 - Dec 06, 2008	223	107
II	20 months	M80/2	Nov 28 - Dec 22, 2009	94	80
III	30 months	M83/1	Oct 14 - Nov 13, 2010	72	72

Table 2.1: Details of the three tracer sampling surveys. The second column states the time after tracer injection. The last two columns state the number of CTD casts taken and on how many of these the tracer was found.

and that diffusivity near the equator is less than 10% of that at mid-latitudes for a similar background of internal waves [*Gregg et al.*, 2003; *Henyey et al.*, 1986; *Kunze et al.*, 2006].

This study reports on the diapycnal diffusivity estimate from the Guinea Upwelling Tracer Release Experiment (GUTRE) which contributes to the knowledge of mixing processes at low latitudes (4°N−12°N). In the Guinea upwelling region, elevated biological productivity at the surface and weak mean circulation create a low oxygen environment at about 400 m depth and a density level of $\sigma_\Theta = 27.1$ kg m^{-3}. The oxygen levels there drop to as low as 40 μmol kg^{-1} [*Stramma et al.*, 2009], compared to a surface oxygen concentration of about 200 μmol kg^{-1}. The accurate estimate of the diapycnal oxygen supply to the oxygen minimum zone requires the accurate diapycnal mixing estimate, where the vertical oxygen gradient is the largest. Hence, tracer was injected at the upper boundary of the absolute oxygen minimum. 92 kg of the tracer were released on April 2008 at 8°N, 23°W on a density surface $\sigma_\Theta = 26.88$ kg m^{-3} with a mean depth of 330 m. Three tracer sampling surveys followed (Table 2.1).

Section two describes the experimental setup of GUTRE. Section three discusses the experimental strategy and the associated data analysis methods. In particular, the advantage of estimating vertical exchange rates in density coordinates is discussed. Section four presents the results from the three tracer surveys and their analysis. Finally, section five briefly discusses the main results.

2.3 Experimental Setup

2.3.1 The Site: Guinea Upwelling Region

The study region (Figure 2.1) is located in the eastern "shadow zone" of the subtropical gyre where the thermocline is ventilated by zonally aligned alternating eastward and westward current branches. The most pronounced eastward flowing current branches transport oxygen-rich waters [*Brandt et al.*, 2008; *Stramma et al.*, 2005]: the North Equatorial Undercurrent (NEUC) and the northern branch of the North Equatorial Countercurrent (nNECC), located at about 5°N and 9°N [*Stramma et al.*, 2005], respectively. On the eastern side of the basin, however, the circulation is weak and the mean flow is not well defined. The tracer injection site, 8°N, 23°W, is located in this region of sluggish circulation. Therefore, the tracer was expected to be confined to the region for the experiment's planned duration of 30 months.

The climatological depths of the tracer target density surface $\sigma_\Theta = 26.88$ kg m^{-3}, as well as shallower ($\sigma_\Theta = 26.8$ kg m^{-3}) and deeper ($\sigma_\Theta = 27.0$ kg m^{-3}) isopycnals, are illustrated in Figure 2.2. The shallower isopycnals are gradually deepening from northwest to southeast affecting the stratification at the tracer target isopycnal. As diapycnal diffusivity estimates might be affected by stratification, two distinctly different regions of stratification were defined (Figure 2.2): low stratification region (region 1s), and high stratification region (region 2s).

2.3.2 Tracer Release

The tracer released in GUTRE was the halocarbon trifluoromethyl sulfur pentafluoride (CF_3SF_5). In earlier tracer release experiments, e.g. NATRE, sulfur hexafluoride (SF_6) was used, but recently its use as a purposeful tracer has been discouraged due to its significant and growing global background concentration and use as a transient tracer of ocean ventilation [e.g., *Bullister et al.*, 2006; *Law and Watson*, 2001; *Tanhua et al.*, 2004]. CF_3SF_5 has similar properties to SF_6, such as very low detection limit, relative ease of analysis, and lack of toxicity but it also has no detectable background concentrations in the ocean [*Ho et al.*, 2008]. It was also chosen as the tracer for an experiment in the Baltic Sea [*Holtermann*

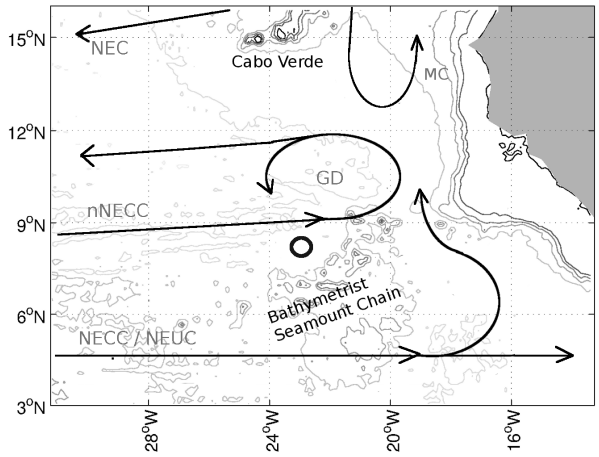

Figure 2.1: Map of the study area, where contours outline the bathymetry above 6000 m depth (contour interval 1000 m). Solid lines mark the schematics of large scale flow field in the thermocline (after *Stramma et al.* [2008b]). Shown are the North Equatorial Current (NEC), the Mauritania Current (MC), the North Equatorial Countercurrent (NECC) connected to the North Equatorial Undercurrent (NEUC), the northern NECC (nNECC) as well as the Guinea Dome (GD). The circle at 8°N, 23°W marks the tracer injection position.

et al., 2012] and for the Diapycnal and Isopycnal Mixing Experiment (DIMES): a large scale tracer release experiment in the Southern Ocean at about 1500 m depth [*Ledwell et al.*, 2011].

In GUTRE, CF_3SF_5 was released with the Ocean Tracer Injection System (OTIS) developed at Woods Hole Oceanographic Institution [*Ledwell and Watson*, 1991]. In total, 92 kg, or 470 mol, of tracer was injected in a set of five streaks, within a 20 km by 20 km area, between April 23 and 26, 2008, from R/V *Maria S. Merian*. During the injection, OTIS was towed along the target isopycnal $\sigma_\Theta = 26.88$ kg m^{-3} (Figure 2.3). A winch control system automatically responded to the deviation from the target density measured by its built-in CTD (Seabird 911plus CTD). In this way, the root mean square (rms) potential density error in the CTD data for the entire injection was calculated to be only 0.002 kg m^{-3}, equivalent to a depth precision of 1.2 m given the mean vertical potential density gradient of 0.0017 kg m^{-4}. In addition to the tracer injection uncertainty, turbulent mixing behind the injection sled increased the thickness of the initial tracer layer. During NATRE the initial survey performed 37 hours after tracer

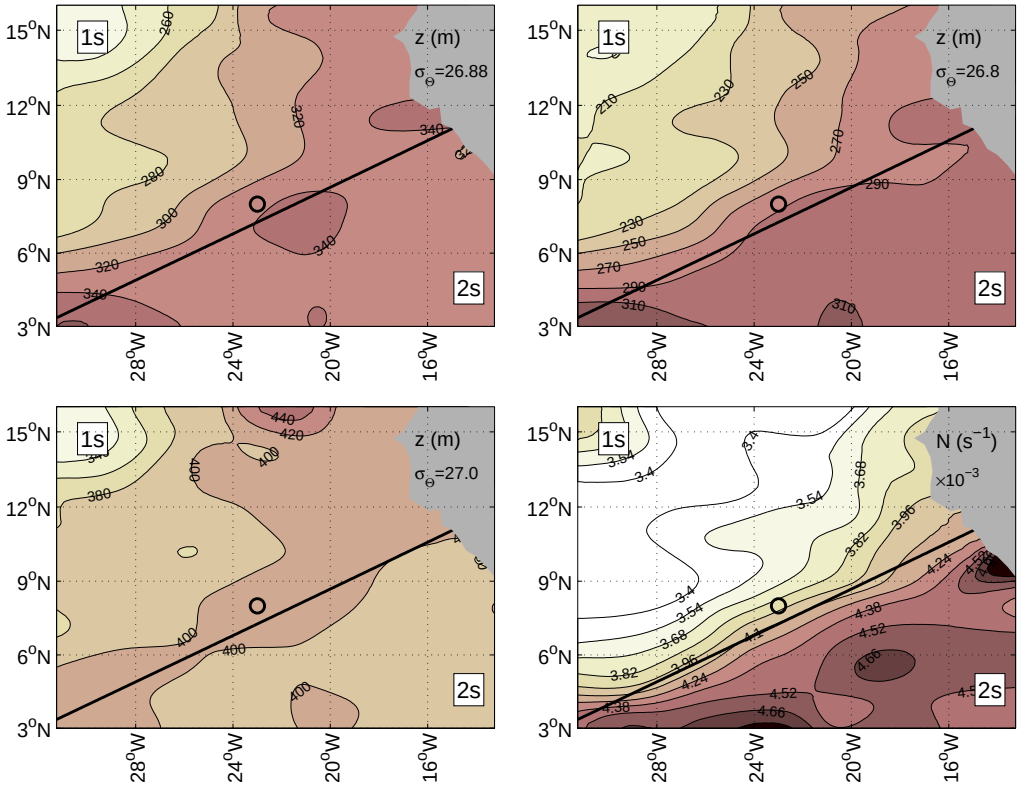

Figure 2.2: Depth of isopycnals $\sigma_\Theta = 26.88$ kg m^{-3}, $\sigma_\Theta = 26.8$ kg m^{-3}, $\sigma_\Theta = 27.0$ kg m^{-3} and strength of stratification (N), where N is the buoyancy frequency. Here N was computed as $N^2 = (g/1026.88)(0.2/(z_{27.0} - z_{26.8}))$. The line separates low (1s) and high (2s) stratification regions. The circle at 8°N, 23°W marks the tracer injection position. The climatology is calculated using the HydroBase2 database of hydrographic profiles [*Curry et al.*, 2003].

injection revealed an initial rms spread of the tracer of about 2 m [*Ledwell et al.*, 1998]. The rms potential density error of the tracer injection, as well as the mean vertical potential density gradient and the use of the OTIS system were all similar for GUTRE. Hence, we assumed that the initial rms width of the tracer injection cloud was 2 m (or 0.0034 kg m^{-3}).

During the campaign, two CTD systems were used: one was mounted on OTIS during injection and the other, a regular profiling CTD, recorded water column profiles in between the injections. The regular profiling CTD was calibrated with more than 180 salinity samples taken along the survey and measured on board using a Guildline Autosal 8400B salinometer. The salinometer was regularly calibrated using IAPSO Standard Seawater. The uncertainty of the calibrated temperature was less than 0.002°C and the uncertainty of the calibrated salinity was less than 0.003, resulting in overall absolute density error from the regular CTD of about 0.004 kg m^{-3}. It is equivalent to a depth error of 2.5 meters.

OTIS built-in CTD was calibrated to accurately estimate the injection location in density space. The instrument was calibrated by comparison with the calibrated regular CTD data taken in the injection area in between the injections (Figure 2.3). With the assumption that temperature sensor mounted on OTIS CTD did not require calibration, only conductivity sensor data was compared. The small correction of 0.036 mS cm^{-1} was added to OTIS CTD conductivity sensor data, such that the differences between the temperature data from both instruments were minimized. Taking into account the regular CTD calibration error of 2.5 m and OTIS CTD calibration method, we estimated the absolute depth uncertainty of the tracer injection to about 3 m, equivalent to 0.005 kg m^{-3}. Thus, the injection isopycnal was $\sigma_\Theta = 26.881 \pm 0.005$ kg m^{-3}.

2.3.3 Tracer Measurements

The tracer (CF_3SF_5) samples were taken using a conventional CTD rosette and measured on-board the research vessels within a few hours of sampling. We used three different purge-and-trap gas chromatographic systems equipped with electron capture detectors for the analysis. Two of these systems were slightly modified versions of the set-up described by *Bullister and Weiss* [1988], and *Bullister*

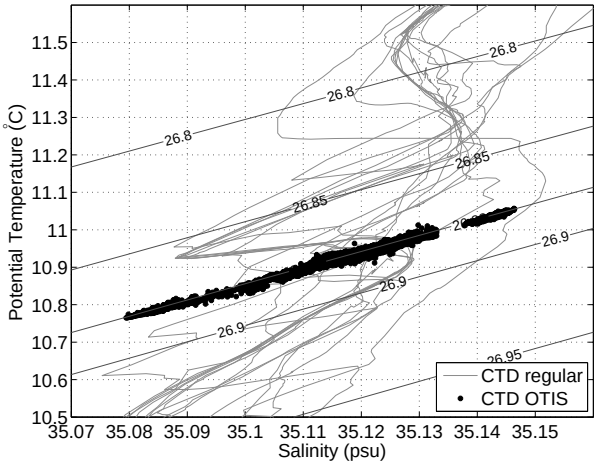

Figure 2.3: TS diagram of water properties during tracer injection at $\sigma_\Theta = 26.881 \pm 0.005$ kg m^{-3} (dots). Regular CTD casts (thin gray lines) were used for calibration of salinity sensors of CTD mounted on OTIS.

and Wisegarver [2008]. Samples were collected in either 100 or 250 ml ground glass syringes from which volumes of 21, 100, or 200 ml, depending on the survey (Table 2.2), were injected into a purge vessel. For the trap we used a 12 cm long 1/8″ stainless steel (SS) tube packed with Haysep D kept at −30°C during the purge phase. The gases in the trap were desorbed at 120°C onto the pre-column. The third system operated with a vacuum-sparge technique [*Law et al.*, 1994] where the sample was sucked into the purge vessel from an ampule of either 350 or 1400 ml volume. The tracer was trapped within 100 cm of 1/16″ tubing packed with Haysep D and desorbed at 160°C . The chromatographic system was the same: 30 cm 1/8″ SS tube packed with Porasil C kept at 50° − 60°C as a pre-column, followed by a 200 cm 1/8″ main-column packed with 180 cm Carbograph 1AC (60-80 mesh) and a 20 cm molecular sieve 5$\mathring{A}$ tail end. The sparging efficiency was continuously checked to ensure 100% (the efficiencies were 93% − 96% during the last survey). The sparging times are given in Table 2.2. This set-up allowed efficient analysis of both CF_3SF_5 and dichlorodifluoromethane or CFC-12 (that elutes slightly after, but well separated from, CF_3SF_5). Standardization was performed by injecting small volumes of a commercially prepared gaseous standard containing CF_3SF_5, but the accuracy of the CF_3SF_5 standard is only ±10%, and no other reference standards exist today for CF_3SF_5. Hence, the

		V_s (ml)	V_a (ml)	Precision (fmol kg^{-1})	Det. lim. (fmol kg^{-1})	T_s (min)
I	7 months	100 (S)	21	0.9	1	4
II	20 months	250 (S)	100	0.16	0.2	7
		350 (A)	306	0.05	0.05	20
III	30 months	250 (S)	200	0.06	0.1	10
		1400 (A)	1000	0.02	0.02	20

Table 2.2: Water sample sizes used to measure CF_3SF_5 during each subsequent survey. Water samples (V_s) were collected either with the ground glass syringes (S) or with glass ampules (A). The volume of the analyzed water sample (V_a) influenced both the precision and detection limit (Det. lim.) of the measurement. A sparging time (T_s) is given in the last column.

absolute values of the measured tracer concentrations were given relative to the biased reference standard, which was the same for all three surveys. However, the absolute value of the CF_3SF_5 measurement is not important for the calculations presented in this manuscript.

The precision and detection limit of CF_3SF_5 measurements depended on the analyzed sea water volume injected into the purge vessel. Ever decreasing concentrations of the spreading tracer patch, over the course of the 30 month experiment, required ever-larger water volumes to be analyzed (Table 2.2). During the later surveys, the analyzed sea water volumes varied with depth: larger volumes were used away from the tracer peak isopycnal. The achieved detection limit was about 1 fmol kg^{-1} during the first survey and as low as 0.02 fmol kg^{-1} during the last survey.

2.4 Data analysis method

The released tracer dispersed with time along and across isopycnals. In GUTRE, three tracer sampling surveys followed the release.

2.4.1 Averaging vertical tracer profiles

For each survey, a mean tracer profile was constructed similar to *Ledwell et al.* [1998]: (1) the tracer concentration measurements in each cast were 'cubic spline'

interpolated over depth onto a one meter bin; (2) density values on one meter intervals were extracted from CTD profile data and binned; (3) alternatively, tracer concentrations were thickness-weighted in each density bin; (4) finally, all individual profiles were interpolated on the same density bin and averaged. The third step, thickness-weighting, is performed to prepare the profiles for the isopynal analysis as described later. In detail, the thickness of each individual profile and each density bin was computed from the density-depth relation smoothed over 0.1 kg m^{-3} density steps. Then the thickness was multiplied by the mean tracer concentration in the density bin to yield tracer (thickness-concentration)-density profile.

The uncertainty ranges of the mean profile were calculated differently from *Ledwell et al.* [1998]. Instead of computing the variance in the shapes of the individual profiles, we used a Monte Carlo method. In detail, the average was calculated for 1000 subsets, each of them consisting of a randomly-selected sample of 50% of the vertical tracer profiles from the survey. The 50% range is chosen to represent uncertainty of the bootstrap procedure, where the synthetic dataset is generated randomly sampling with replacement. Two standard deviations were taken for the 95% confidence interval of the mean tracer profile. The uncertainty takes into account the variability in the shapes of individual profiles.

2.4.2 Advection-diffusion equation in Cartesian coordinates

The mean tracer spread across isopycnals can be described by the advection-diffusion equation in Cartesian coordinates as

$$\frac{\partial \bar{c}}{\partial t} + w^z \frac{\partial \bar{c}}{\partial z} = \frac{\partial}{\partial z}\left(D^z \frac{\partial \bar{c}}{\partial z} \right), \tag{2.1}$$

where D^z is the diapycnal diffusion coefficient of the tracer, w^z is vertical velocity, and $\bar{c}$ represents the regional average of the tracer concentration. In this study, we also used the expanded version of equation (2.1), as adopted from *Ledwell*

et al. [1998] (their equation (7)):

$$\frac{\partial \bar{c}}{\partial t} + \left(w^z - \frac{\partial D^z}{\partial z} \right) \frac{\partial \bar{c}}{\partial z} = D^z \frac{\partial^2 \bar{c}}{\partial z^2}. \tag{2.2}$$

The quantity $((\partial z/\partial t)^\sigma)$, which represents the vertical movement of isopycnal surfaces relative to the target density surface from survey to survey, was omitted in equation 2.1. In GUTRE, a large spatial variation in stratification (Figure 2.2) did not allow to observe its temporal changes.

When tracer spreads in the field, where stratification regionally varies, the equation in Cartesian coordinates must, however, be used with care. In special situations, the tracer analysis in Cartesian coordinates may lead to the paradox of negative diapycnal diffusion rates. As a thought experiment, lets assume that the evolving tracer patch is advected over time from low to high stratification regions. In density space, the mean tracer thickness is always increasing with time, but in Cartesian space, thickness is decreasing due to compression of the isopycnals, which leads to the negative D^z estimate.

2.4.3 Advection-diffusion equation in isopycnal coordinates

It is helpful to apply advection-diffusion equation written directly in isopycnal coordinates. Especially, when tracer profiles are initially averaged over density to avoid the effect of transient isopycnal displacements due to internal waves and other oceanic variability. Following [*de Szoeke and Bennett*, 1993], the advection-diffusion equation in isopycnal coordinates is written as:

$$z_\rho \left(\frac{\partial \bar{c}}{\partial t} + w^\rho \frac{\partial \bar{c}}{\partial \rho} \right) = \frac{\partial}{\partial \rho} \left(D^z \frac{1}{z_\rho} \frac{\partial \bar{c}}{\partial \rho} \right), \tag{2.3}$$

where $z_\rho = \partial z/\partial \rho$ is the spacing of isopycnals per unit density and is often termed the "thickness"; w^ρ is the diapycnal velocity, which is the difference between vertical velocity w^z and the vertical motion of an isopycnal surface. Note, that the units of w^ρ are kg m^{-3} s^{-1}, which when multiplied by the "thickness", z_ρ, converts to Cartesian units of m s^{-1}.

Before equation (2.3) is applied to the regionally averaged tracer profiles,

the method of averaging becomes important. Commonly, the individual tracer profiles are averaged over isopycnals resulting in a mean tracer concentration-density profile. *de Szoeke and Bennett* [1993] discusses thickness-weighted average for the macroscales, which can be written as $\langle c \rangle = \overline{z_\rho c}/\overline{z_\rho}$. The quantity $\overline{z_\rho c}$ defines the mass of c in the isopycnic volume, i.e., volume between isopycnals of thickness z_ρ and a unit area. Hence, $z_\rho c$ assures that with varying isopycnal thickness from one region to the other, volumetric concentration of c stays the same.

The advection-diffusion equation in isopycnal coordinates with thickness-weighted average is written as:

$$\overline{z_\rho}\left(\frac{\partial\langle c\rangle}{\partial t} + \langle w^\rho\rangle\frac{\partial\langle c\rangle}{\partial\rho}\right) = \frac{\partial}{\partial\rho}\left(D^z\frac{1}{\overline{z_\rho}}\frac{\partial\langle c\rangle}{\partial\rho}\right), \tag{2.4}$$

where the diapycnal diffusion coefficient is parametrized as [*de Szoeke and Bennett*, 1993; *Osborn and Cox*, 1972]: $D^z = \kappa^\rho \cdot \langle\overline{|\partial\rho_*|^2}\rangle\overline{z_\rho}^2$, where κ^ρ is molecular diffusivity of density, considered to be a constant, and $\overline{|\partial\rho_*|^2}$ is the mean square density variance. Introducing a new quantity $D^\rho = \kappa^\rho \cdot \overline{|\partial\rho_*|^2}$, the diapycnal diffusion coefficient D^z in equation (2.4) can be rewritten as $D^z = \langle D^\rho\rangle\overline{z_\rho}^2$. Expanding all of the thickness-weighted averaging operators gives:

$$\left(\frac{\partial\overline{z_\rho c}}{\partial t} + \frac{\overline{z_\rho w^\rho}}{\overline{z_\rho}}\frac{\partial\overline{z_\rho c}}{\partial\rho}\right) = \frac{\partial}{\partial\rho}\left(\frac{\overline{z_\rho D^\rho}}{\overline{z_\rho}}\frac{\partial\overline{z_\rho c}}{\partial\rho}\right), \tag{2.5}$$

or

$$\left(\frac{\partial\overline{z_\rho c}}{\partial t} + \langle w^\rho\rangle\frac{\partial\overline{z_\rho c}}{\partial\rho}\right) = \frac{\partial}{\partial\rho}\left(\langle D^\rho\rangle\frac{\partial\overline{z_\rho c}}{\partial\rho}\right). \tag{2.6}$$

Advection-diffusion equations written in terms of Cartesian coordinates (equation (2.1)) and isopycnic coordinates (equation (2.6)) are comparable when w^z is exchanged with $\langle w^\rho\rangle$, D^z with $\langle D^\rho\rangle$, and $\overline{c}$ is exchanged with $\overline{z_\rho c}$. The units of all the quantities in equation (2.6) are all isopycnic: $\langle w^\rho\rangle$ has units of kg m^{-3} s^{-1}, $\langle D^\rho\rangle$ has units of (kg m^{-3})^2 s^{-1}, and $\overline{z_\rho c}$ units of mol m kg^{-1}. From here on we omit the averaging brackets for the simplicity, bearing in mind that all isopycnal analysis is done with the applied thickness-weighted average.

The newly defined D^ρ has a meaning of diapycnal diffusion coefficient ex-

pressed in isopycnic units. In literature, various symbols are used to indicate the diapycnal diffusion coefficient expressed in Cartesian units, most commonly: K_z, K_ρ, D_z. In this study, we use the superscript instead of the subscript to mark the choice of coordinate system to distinguish it from the notation of the derivative. Thus, D^z refers to Cartesian units of $m^2\ s^{-1}$ and D^ρ to isopycnic units of $(kg\ m^{-3})^2\ s^{-1}$.

2.4.4 Discretization of advection-diffusion equation

Equations (2.1) and (2.6) are identical in the form and can be expanded the same way as equation (2.2). The same discretization algorithm was applied for both equations. Equation (2.2) was discretized using a forward-time, centered-space algorithm as in [*Glover et al.*, 2011]:

$$c_i^{n+1} = a_- c_{i-1}^n + a_0 c_i^n + a_+ c_{i+1}^n, \tag{2.7}$$

where $a_- = b/2 + d$, $a_0 = 1 - 2d$, and $a_+ = -b/2 + d$, defining a dimensionless advection number as $b = [(w^z - \partial D^z/\partial z)\Delta t]/\Delta z$, and a dimensionless diffusion number as $d = [(D^z + z \times (\partial D^z/\partial z) + z_0)\Delta t]/(\Delta z)^2$. Here z is the vertical coordinate and z_0 - its first (and lowest) value. Thus, positive $\partial D^z/\partial z$ indicates a diapycnal diffusivity that decreased with increasing depth.

The numerical solution of the advection-diffusion equation with three adjustable parameters: D^z, $\partial D^z/\partial z$, and w^z, was fitted to the mean vertical tracer profile of each survey. The equation used an initial Gaussian tracer distribution with a second moment of 2 m, or 0.0034 kg m^{-3} (the precision of the tracer injection). The optimal set of adjustable parameters was found by maximum likelihood estimate, which minimized χ^2 defined as:

$$\chi^2 = \sum_i [(c_i' - \bar{c}_i)/\delta_i]^2 \tag{2.8}$$

where the prime indicates model results, $\bar{c}$ the observations, and δ the observational uncertainty of the vertical tracer profile.

The uncertainty of the vertical mixing parameters was evaluated using the Monte Carlo method. In detail, the maximum likelihood estimate (χ^2) and cor-

responding numerical best-fit solution were computed with a generated set of 1000 mean vertical tracer profiles for each survey. Each profile in a set was averaged over the 50% randomly-selected profiles in a survey. Two standard deviations in parameters D^z, $\partial D^z/\partial z$, and w^z defined the 95% confidence interval.

2.4.5 Gaussian fit approach

When the mean vertical tracer profiles closely resemble Gaussian shapes, the simple diffusion model fully describes the vertical widening of a tracer. Then, the diapycnal diffusion coefficients (D^z and D^ρ) can be directly estimated from the time series of the second moments, while the diapycnal velocities (w^z and w^ρ) can be calculated from the corresponding first moments. The Gaussian fit was applied both to the mean tracer concentration-density and (thickness-concentration)-density profiles. In the first case, the estimated parameters had Cartesian units (D^z and w^z) and in the second case - isopycnic units (D^ρ and w^ρ).

The uncertainties of the diapycnal diffusion coefficient and the diapycnal velocity were computed following a similar procedure as above. In detail, the Gaussian was fitted and, thus, D^z and w^z calculated, for each averaged vertical tracer profile of 1000 subsets. Two standard deviations in D^z and w^z variation were set for the 95% confidence interval.

2.5 Results

The three major tracer surveys followed 7, 20, and 30 months after the injection. The individual tracer profiles in each survey were averaged over density to obtain the mean tracer concentration-density or mean tracer (thickness-concentration)-density profile. Then, for the Cartesian coordinate analysis, the density coordinate was transformed to the height coordinate using the mean density-depth relation. Finally, the diapycnal mixing parameters were estimated by solving advection-diffusion equations both in Cartesian and in isopycnal coordinates.

2.5.1 Spreading of the tracer

The first survey after tracer injection was performed in November 2008 (after 7 months) from R/V *Maria S. Merian* (Table 2.1). The biggest challenge was to capture the narrow streaks of the spreading tracer patch. The tracer concentrations between the casts varied significantly, even when separated by distances as small as 30 km (Figures 2.4a and 2.4b). In total, the tracer was detectable in about 50% of the casts (Table 2.1) and most of it was found in the region 20°W−24°W, 6°N−11°N.

The second survey followed in December 2009 (after 20 months) from R/V *Meteor*. In the sampled region of 4°N−14°N, 15°W−30°W (Figure 2.4c), the tracer was detected in about 85% of all casts. The third survey was performed in October-November 2010 (after 30 months) from R/V *Meteor* in the region of 3°N−15°N, 15°W−28°W (Figure 2.4d). Here, the tracer was detected in all of the casts and the tracer inventory distribution shows that the tracer patch expanded farther to the west than the westernmost sampled longitude of 28°W.

The contour maps of the tracer column integrals (Figure 2.4) illustrate the lateral tracer patch distribution for each survey. The contours were interpolated using Gaussian weights, where the meridional radius of influence is chosen arbitrarily to be 25 km (first survey) and 100 km (second and third surveys). The zonal radius of influence was twice as large. Furthermore, the zeros were assigned at a cut-off radius distance from the nearest cast position; cut-off radius being two times the radius of influence. The sum of the smoothed tracer inventories for the first, second, and third surveys roughly indicate that about 50%, 60%, and 70% of all the injected tracer was found, respectively. It is important to note that the uncertainties of such inventory calculations are large and the estimates must be used with care. Overall, the visual inspection of the lateral tracer patch distribution suggests a large amount of tracer clustered near the injection site for all three surveys and implies little mean lateral advection in the region.

The tracer patch expanded vertically from a thickness of about 80 m in seven months to almost 200 m in thirty months after injection. The individual tracer concentrations, as measured in water samples taken from the Niskin bottles, are shown in Figure 2.5. During the first survey, the maximum tracer concentrations

peaked at 230 fmol kg^{-1}, but half of the profiles had peak concentrations in the range of 10 to 70 fmol kg^{-1}. In the second survey, the peak concentrations dropped significantly: mostly in the range of 2 to 4 fmol kg^{-1}, while the largest overall measured concentration reached 6.5 fmol kg^{-1}. The third survey, which was carried out ten months later, had largest concentrations of about 4 fmol kg^{-1} and half of the peak concentrations varied in the range of 1 to 2.5 fmol kg^{-1}.

Several examples of the individual tracer concentration-height profiles for each subsequent survey are shown in Figures 2.6, 2.7, and 2.8, respectively. The tracer profiles in the first survey mostly had narrow single peaks located at different densities. The mean vertical profile, respectively, had large uncertainty ranges. In the second survey, the vertical tracer profiles were broader and better resolved by imposed minimum sampling distance of 10 m. A bimodal distribution was often found in the vertical tracer profiles resulting in high variability in the shapes of the profiles. In the third survey, the individual vertical tracer profiles started to resemble Gaussian distribution with fewer low concentration intrusions.

In summary, the spatial and vertical distribution of the tracer patch found in three surveys agrees with the previously suggested image of how the tracer evolves with time [*Ledwell et al.*, 1998]. In the beginning, the tracer patch is comprised of a number of streaks as narrow as tens of kilometers. The vertical tracer profiles are strongly distorted. However, after 30 months the streaks have merged and individual vertical tracer profiles start to resemble a Gaussian distribution. Also the higher tracer column inventories were found near the injection site for each survey, indicating a weak mean advection of the center of mass of the evolved tracer patch. We conclude, that in agreement with the expected weak lateral circulation of the "shadow zone" thermocline, the tracer patch stayed on the eastern side of the basin for the whole period of 30 months and was first streaked, but later homogenized by the lateral eddies.

2.5.2 Density-depth relation

The mean density-depth profile enables the conversion of vertical coordinates from density to height above the tracer injection isopycnal. The profile and its error ranges were computed from the data merged from the three tracer surveys

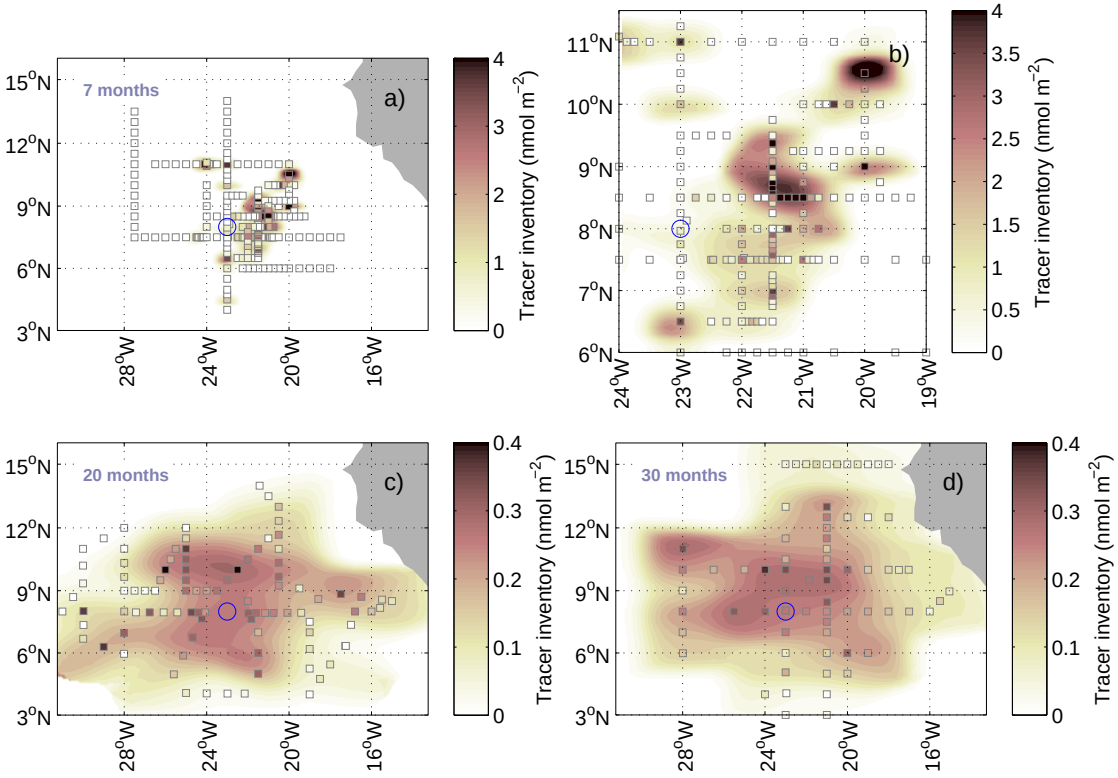

Figure 2.4: Horizontal tracer patch distribution during three surveys: a) and b) in November 2008 (7 months after tracer release) c) in December 2009 (20 months after tracer release) d) in October–November 2010 (30 months after tracer release). The color of the squares represents the tracer column integral; the same colorbar applies to the filled contours. The blue circle at 8°N, 23°W marks the tracer injection position, but the symbol is larger than the 20 km by 20 km area of the injection.

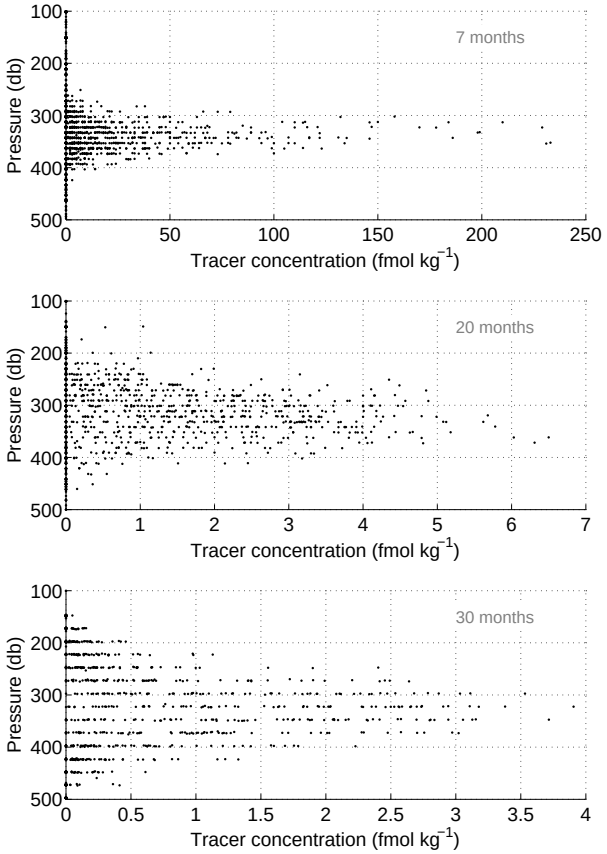

Figure 2.5: Tracer concentrations sampled at discrete depth levels for three surveys: 7, 20, and 30 months after the tracer injection. The detection limits of the surveys were 1 fmol kg^{-1}, $0.05 - 0.2$ fmol kg^{-1}, and $0.02 - 0.1$ fmol kg^{-1}, respectively.

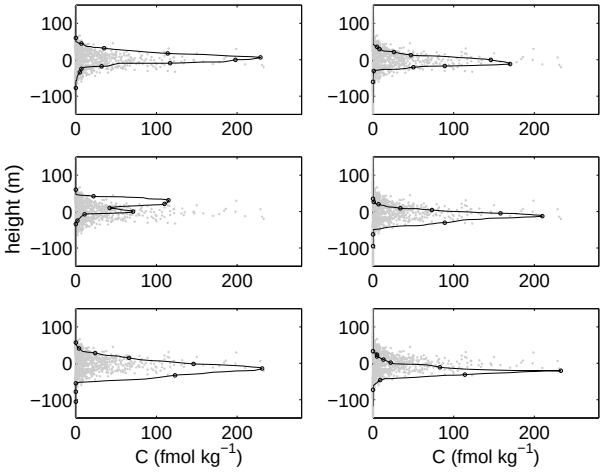

Figure 2.6: Six individual tracer profiles with the largest vertical tracer concentration integral value during the first survey in November 2008 (7 months after tracer release). The ordinate is height above the target density surface in the mean potential density gradient of 0.0017 kg m^{-4}. Grey dots in the background mark all of the measured data in the survey.

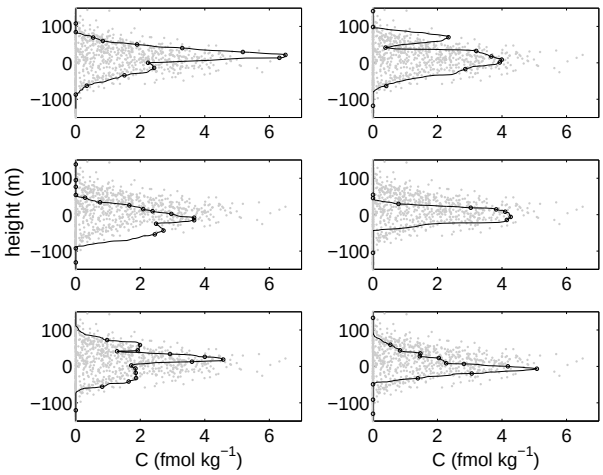

Figure 2.7: Same as in Figure 2.6, but during the second survey (20 months after tracer release).

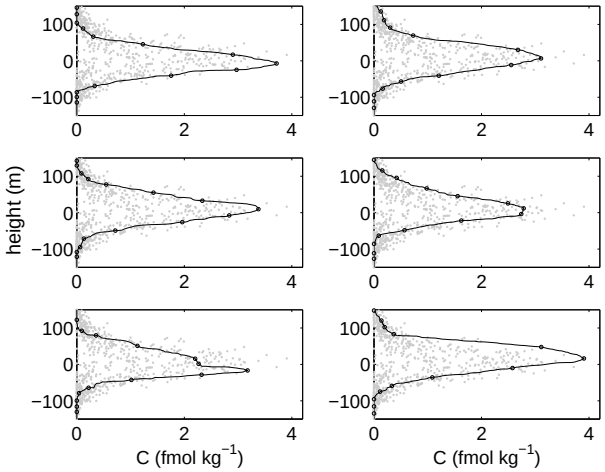

Figure 2.8: Same as in Figure 2.6, but during the third survey (30 months after tracer release).

and binned in a $1° \times 1°$ grid (Figure 2.9). Individual profiles revealed a large variation in the depth of the isopycnals above the target density $\sigma_\Theta = 26.88$ kg m^{-3}. This corresponds to the systematic variability of stratification in the region (Figure 2.2). To investigate the influence of stratification on our calculations, we separately computed the diapycnal diffusion coefficient in two regions of distinctively different stratification (1s and 2s in Figure 2.2) using the corresponding local mean density-depth profiles as marked in Figures 2.9b and 2.9c.

The mean density gradient was computed in the density range of ± 0.05 kg m^{-3} around the tracer target isopycnal both locally and over the whole region. The density gradient in region (1s) was 0.0015 kg m^{-4} resulting in the buoyancy frequency of $N = 3.8 \times 10^{-3}$ s^{-1}. Region (2s) had about a 30% larger stratification ($N = 4.7 \times 10^{-3}$ s^{-1}) corresponding to the mean density gradient of 0.0023 kg m^{-4}. Over the entire region, the mean buoyancy frequency was $N = 4.0 \times 10^{-3}$ s^{-1} with the mean density gradient of 0.0017 kg m^{-4}.

2.5.3 Diapycnal diffusion coefficient estimate

The diapycnal diffusion coefficient was estimated by numerically solving advection-diffusion equation (2.7) or by the Gaussian fit applied to the regionally averaged vertical tracer profiles (Figures 2.10 and 2.11). For the Cartesian coordinate

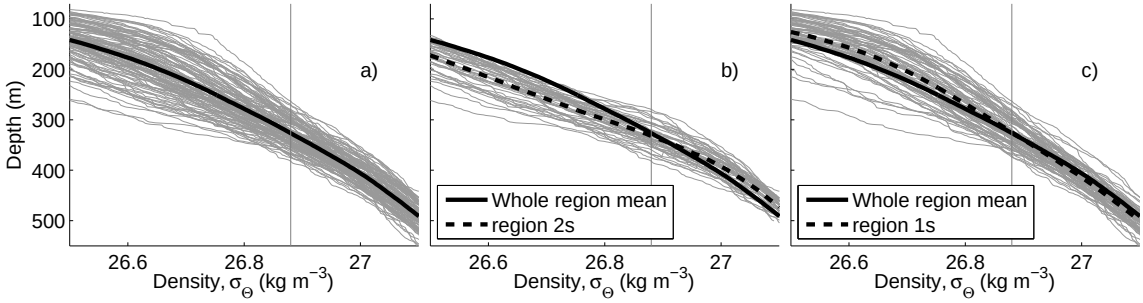

Figure 2.9: Density-depth profiles (thin gray lines) from the three tracer sampling surveys, binned over $1^\circ \times 1^\circ$ grid: a) over the whole region, b) in high stratification region (2s), c) in low stratification region (1s). The vertical line indicates the isopycnal of the tracer injection. The solid line (same in all three graphs) represents the mean vertical density profile for the whole region. The dashed line represents the local mean vertical density profile.

analysis tracer concentration-height profiles were used (Figure 2.12), while for the isopycnal coordinate analysis thickness weighted tracer concentration-density profiles were analyzed (Figure 2.11).

The mean diapycnal diffusion coefficient estimate from the two methods and over the whole region and the period of 30 months was $D^z = (1.19 \pm 0.18) \times 10^{-5}$ m^2 s^{-1}, or $D^\rho = (3.07 \pm 0.58) \times 10^{-11}$ (kg m^{-3})^2 s^{-1}. The result is an average of estimates from the three surveys (Table 2.3), each computed starting with the time of injection. As expected, D^z and D^ρ estimates from both Gaussian fit approach and numerical solution of the advection-diffusion equation were similar (Figure 2.13), since the mean vertical tracer profiles closely resembled Gaussian shapes (Figure 2.12). Between the two coordinate systems in which parameters were estimated, the results differ by only 0.13 m^2 s^{-1} and the difference is not significant in the range of uncertainties. D^ρ converted to Cartesian units using density-depth gradient averaged over the whole region (0.0017 kg m^{-4}) results in $(1.06 \pm 0.2) \times 10^{-5}$ m^2 s^{-1} estimate.

The diapycnal diffusion coefficient estimates differed only slightly from survey to survey given the range of uncertainties. The main source of uncertainty arose from the distortions of the individual vertical tracer profiles, and hence the homogeneity of the tracer patch. However, the time errors due to the duration of the tracer sampling survey and the precision of the tracer injection have also been

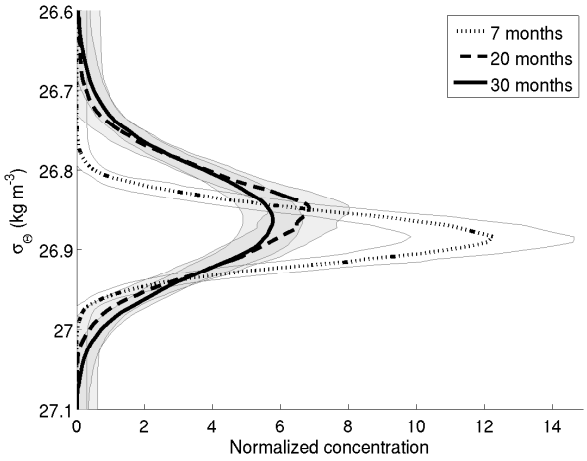

Figure 2.10: Normalized mean vertical tracer profiles for each of the three surveys. Uncertainty represents the variability in the shapes of the individual tracer profiles and the detection limit.

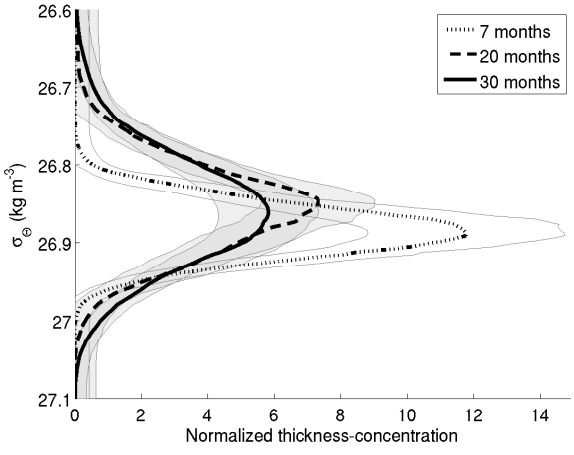

Figure 2.11: Normalized thickness-weighted average tracer profiles for each of the three surveys. Uncertainty represents the variability in the shapes of the individual tracer profiles and the detection limit.

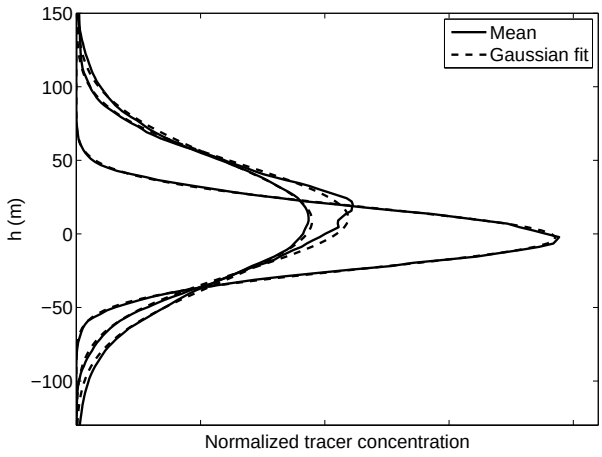

Figure 2.12: Normalized mean vertical tracer profiles for each of the three surveys, as in Figure 2.10, but ordinate is converted to height above the target density surface using the mean density-depth profile (Figure 2.9a). The Gaussian distributions fitted to the profiles are marked by the dashed lines.

accounted for. All of the errors decreased significantly with time: the sampling error due to the increasing homogeneity of the tracer patch, the other two errors due to the increasing time interval between the tracer injection and the survey. The survey's sampling time period of about one month increased the diapycnal diffusivity estimate error in the first survey, contributing almost the same as all other error sources together. After 30 months, the error associated with survey's duration accounted for about 20% of the overall error.

2.5.4 Diapycnal velocity and diapycnal diffusivity gradient

The diapycnal velocity estimate over the period of 30 months was $w^z = (0.5 \pm 1.5) \times 10^{-7}$ m s^{-1}, or $w^\rho = (1.5 \pm 2.7) \times 10^{-10}$ kg m^{-3} s^{-1}, but a large variation of estimates from survey to survey was observed (Table 2.3). During the first survey, the peak of the mean tracer profile was located below the injection density by about 2 m. This resulted in a negative diapycnal velocity estimate of $(-1.5 \pm 2.6) \times 10^{-7}$ m s^{-1}. Deepening of the tracer patch has been observed in previous tracer release experiments [*Ledwell and Bratkovich*, 1995; *Ledwell and Watson*,

	time	$D^\rho \times 10^{-11}$	$w^\rho \times 10^{-10}$	$D^z \times 10^{-5}$	$w^z \times 10^{-7}$
	(months)	$((\text{kg m}^{-3})^2\ \text{s}^{-1})$	$(\text{kg m}^{-3}\ \text{s}^{-1})$	$(\text{m}^2\ \text{s}^{-1})$	(m s^{-1})
I	6.8	3.14 ± 0.68	-2.5 ± 4.5	1.17 ± 0.21	-1.5 ± 2.5
II	19.5	3.13 ± 0.60	4.5 ± 2.0	1.28 ± 0.21	2.0 ± 1.2
III	30.1	2.91 ± 0.33	2.4 ± 1.2	1.13 ± 0.11	1.0 ± 0.7
	Average	$\mathbf{3.07 \pm 0.58}$	$\mathbf{1.5 \pm 2.7}$	$\mathbf{1.19 \pm 0.18}$	$\mathbf{0.5 \pm 1.5}$

Table 2.3: Diapycnal diffusivity and diapycnal velocity for each survey.

1991; *Ledwell et al.*, 1998]. This was attributed either to the sinking of the tracer droplets before dissolving, or to the adsorption of tracer onto the sinking particulates, or salt finger fluxes. In GUTRE, however, the tracer patch was found to have risen during the two later surveys, 20 and 30 months after tracer injection. The tracer peak during both surveys was located about 10 m above the target isopycnal. When calculated over the last two surveys, the mean diapycnal velocity was $w^z = (1.5 \pm 1.0) \times 10^{-7}$ m s^{-1} (i.e., approximately 5 m yr^{-1}). The vertical gradient of the diapycnal mixing coefficient ($\partial D^z/\partial z$) was analyzed as one of the mechanisms which might explain the observed tracer peak rising through the isopycnals.

The vertical gradient of diapycnal mixing coefficient ($\partial D^z/\partial z$) skews the tracer profiles. A constant positive $\partial D^z/\partial z$ would cause the peak of a Gaussian distribution to migrate downwards with velocity $-2\partial D^z/\partial z$, while the center of mass of the distribution would migrate upwards with velocity $\partial D^z/\partial z$, resulting in a distorted profile [*Ledwell et al.*, 1998]. However, the evaluated vertical gradient of the diapycnal diffusion coefficient for all three surveys was nearly zero within the uncertainty range: $(-1.2 \pm 4.9) \times 10^{-8}$ m s^{-1}. The negative sign indicates the downward increase of the diapycnal mixing coefficient. The very small estimate of skewness justifies the fitting of a Gaussian distribution model to the data. Consequently, the $\partial D^z/\partial z$ estimate is too small to account for the ascent of the tracer patch through the isopycnals.

2.5.5 Regional Variation of Diapycnal Diffusivity

The thickness of a tracer patch in Cartesian coordinates depends on the local stratification, because an isopycnally homogeneous tracer patch appears thinner

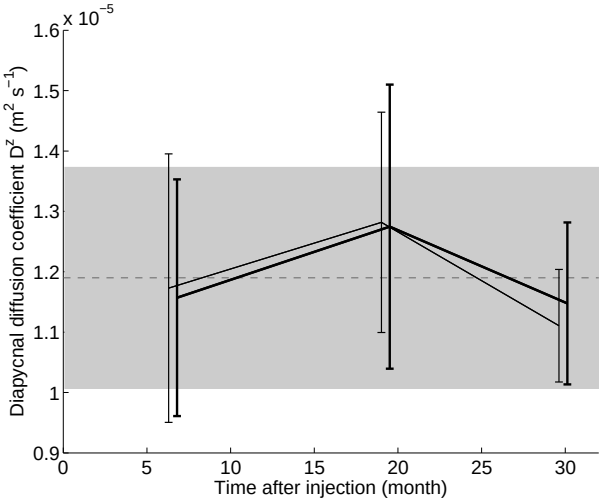

Figure 2.13: Diapycnal diffusivity in Cartesian coordinates for each of the three surveys, computed starting with the initial tracer injection profile. The thin line (shifted in time for better visibility) marks the result from the Gaussian fit method, and the thick line is the numerical solution. The whole region mean (dashed line) and uncertainty ranges (gray patch) are computed using Monte Carlo method, where subsets are randomly picked from the uncertainty ranges of each survey.

in high than in low stratification regions. Thus, differences in the diapycnal mixing estimate derived in Cartesian and in isopycnal coordinates are to be expected between the regions of different stratification. In GUTRE, two distinct regions of different stratification allowed for the comparison of the local D estimates solving the advection-diffusion equation both in Cartesian and in isopycnal coordinates.

A spatial distribution of the thicknesses of the individual tracer profiles was analyzed with respect to the spatial distribution of stratification (Figure 2.2). The Gaussian distribution was fitted to each individual tracer concentration-depth profile for the Cartesian estimate and to each individual tracer (thickness - concentration) - density profile for the isopycnal estimate. The thickness of each profile was then converted using Fick's law to D^z or D^ρ, respectively. The conversion allowed to merge the two last surveys. The data of the first survey was omitted in Figure 2.14 for simplicity and its limited spatial extent. The color ranges of the maps of D^z (Figure 2.14 left) and D^ρ (Figure 2.14 right) were adjusted by using relation: $D^\rho = D^z\overline{\rho_z}^2$, where $\overline{\rho_z}$ is the density gradient averaged over the whole region (0.0017 kg m^{-4}). The visual inspection of the diapycnal mixing estimates from the the noisy individual profiles indicated that the vertical tracer profiles expressed in meters were found often wider in the low stratification region. D^ρ differences between the regions were less obvious, but a number of large values were found in the high stratification region.

The more stringent analysis of the regional differences between D^z and D^ρ was carried by averaging the tracer profiles in each of the two different stratification regions (denoted 1s and 2s in Figure 2.2) by the similar procedure as used for the whole region. For Cartesian coordinates, however, the density coordinate was converted to Cartesian coordinate using the regionally averaged density-depth relation (Figure 2.9 b and c). In Cartesian coordinates, regional mean D^z estimates were nearly a factor of 2 larger in the low (1s) than in the high (2s) stratification regions, the difference being statistically significant (Table 2.4, Figure 2.15). The analysis carried out in the isopycnal coordinate system, however, yielded a much more similar D^ρ between the two regions. In the low stratification region, the D^ρ estimate was about 25% smaller, but the difference was not significant. In conclusion, instead of reporting two local diapycnal diffusion coefficients (D^z) and corresponding mean local stratification, a single D^ρ estimate suffices.

Region		$\overline{\rho_z}$ kg m^{-4}	D^ρ $\times 10^{-11}$ ((kg m^{-3})^2 s^{-1})	$D^\rho/\overline{\rho_z}^2$ $\times 10^{-5}$ (m^2 s^{-1})	D^z $\times 10^{-5}$ (m^2 s^{-1})
Low strat.	(1s)	0.0015	2.72 ± 0.68	0.94 ± 0.24	1.26 ± 0.24
High strat.	(2s)	0.0023	3.48 ± 0.94	1.20 ± 0.33	0.74 ± 0.15

Table 2.4: Local diapycnal diffusion coefficients averaged over all three surveys. D^ρ was converted to Cartesian units using the whole region's mean density-depth gradient of $\overline{\rho_z} = 0.0017$ kg m^{-4}. D^z was estimated using local mean density-depth relation (as in Figure 2.9).

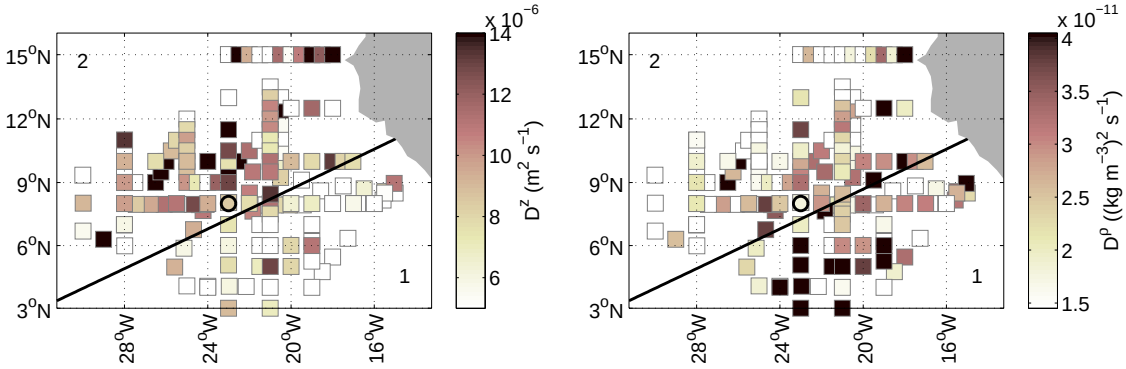

Figure 2.14: Regional variability of the diapycnal diffusion coefficient in Cartesian units (left) and in isopycnic units (right). The coefficients where computed for each individual vertical tracer profile of the last two surveys. The colorbar ranges are adjusted to be comparable using the mean density gradient of 0.0017 kg m^{-4}.

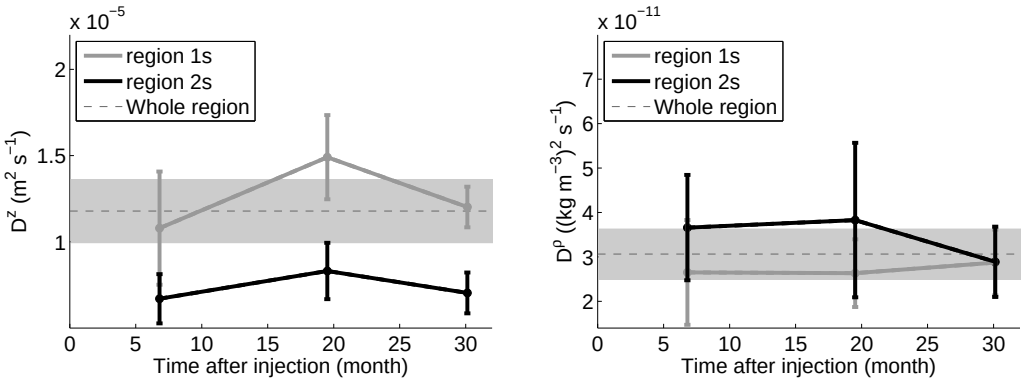

Figure 2.15: Diapycnal diffusivity for each of the three surveys averaged over low (1s) or high (2s) stratification regions. Left: in Cartesian coordinates (D^z), computed using the respective local mean density-depth profiles (Figures 2.9b and 2.9c). Right: in isopycnal coordinates (D^ρ). The gray shading marks the whole region mean estimate of D^z and D^ρ, respectively (Table 2.3).

2.6 Discussion

A deliberate tracer release experiment, carried out during the years $2008-2010$, was used to study diapycnal mixing in the tropical northeastern Atlantic. We have chosen two ways to present the resulting diapycnal mixing estimates: in Cartesian units of $\mathrm{m}^2\ \mathrm{s}^{-1}$ (D^z) and in isopycnic units of $(\mathrm{kg\ m}^{-3})^2\ \mathrm{s}^{-1}$ (D^ρ). D^ρ represents the tracer spreading rate in density coordinates, while D^z is the Cartesian coordinate counterpart. The alternative approach to investigate the tracer spread in isopycnal coordinates follows the method outlined by *de Szoeke and Bennett* [1993] and is motivated by the special stratification conditions; two large permanent regions of distinctive stratification were found in the GUTRE region.

When tracer spreads along isopycnals, it looks thinner in high stratification region, when expressed in Cartesian coordinates. This then translates to a smaller diapycnal mixing coefficient. In GUTRE, the local D^z estimate was nearly a factor of 2 smaller in the high stratification region, while the local D^ρ estimate was more similar between the two regions: $\sim 25\%$ larger and not significant in the range of uncertainties. In general, when a tracer is moving from one region to the other, it is difficult to assess diapycnal diffusion coefficient locally. However, local values of D are needed to calculate the local diapycnal fluxes. One can, similarly, conceive a situation where the tracer distribution was only measured in one of the two density-gradient regions. The diapycnal diffusivity constant in Cartesian coordinates (D^z) would then be well determined for this region, but would result in erroneous fluxes if applied to the region with different stratification. The use of the universally determined D^ρ facilitates the local calculations of fluxes, by being less correlated with the local stratification conditions.

The small differences between local D^ρ estimates is a result of the similarity between the thickness-weighted tracer profiles, or the similarity of the diapycnal tracer fluxes in the two regions of different stratification. Considering constant stratification over each of the two regions, differences in the diapycnal tracer flux are expressed through the differences in the diapycnal flux of density ($D^z\overline{\rho_z}$ or $D^\rho/\overline{\rho_z}$). Taking local D^z or D^ρ estimates and corresponding local mean stratification, the local diapycnal density flux differed by less than 20%, which is not

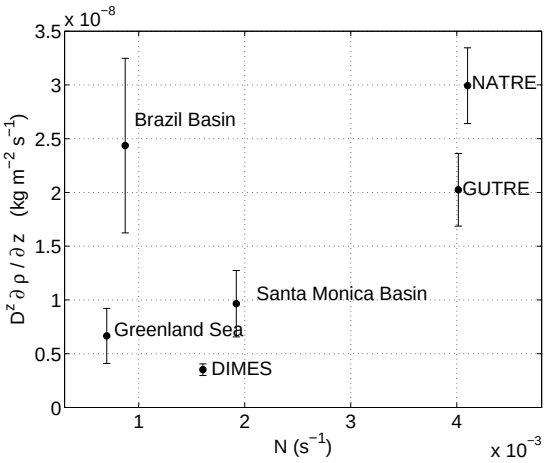

Figure 2.16: Diapycnal flux of density for five earlier tracer release experiments in comparison with the present study (GUTRE) plotted as a function of buoyancy frequency (N)

significant at the 95% confidence interval. Hence, the diapycnal density flux is a good quantity to compare GUTRE diapycnal mixing results with other tracer release experiments performed under various stratification conditions (Figure 2.16). The comparison shows that the diapycnal density flux near the rough topography of the Brazil basin (BBTRE [*Polzin et al.*, 1997; *Rye et al.*, 2012]) is similar to the fluxes in the subtropical thermocline (NATRE [*Ledwell et al.*, 1998], GUTRE). They are, however, at least three to four times larger than the fluxes in the high latitude regions of very weak stratification (Greenland Sea [*Watson et al.*, 1999], DIMES [*Ledwell et al.*, 2011]).

In many ways, GUTRE results are comparable to the results of NATRE, performed at a latitude range of 20°N−26°N. Both experiments were carried out at similar depths and had similar mean stratification. GUTRE, however, was the first tracer release experiment performed in the thermocline at low latitudes (4°N−12°N). Internal wave-wave interaction model [*Henyey et al.*, 1986], recently validated by the observations [*Gregg et al.*, 2003], predicts reduced mixing from the breaking of internal waves at low latitudes. Assuming comparable stratification, internal wave shear levels, and their frequency content at both sites, the diapycnal diffusivity can be parametrized as $K_{pG} = (f_G \cdot arccosh(N_0/f_G))/(f_N \cdot arccosh(N_0/f_N))$ [*Gregg et al.*, 2003; *Kunze et al.*, 2006], where f_G and f_N are

Coriolis parameters at the GUTRE and NATRE sites, respectively. In this way, the diapycnal diffusivity at GUTRE site was expected to be smaller by about 60% as compared to the NATRE estimate of $(1.7 \pm 0.2) \times 10^{-5}$ m^2 s^{-1}. However, the diapycnal diffusivity in GUTRE is only 30% smaller than the estimate of NATRE. This indicates an enlarged background internal wave field in GUTRE region. Indeed, the hypothesis was confirmed by the accompanying shear microstructure and shipboard ADCP measurements [*Fischer*, 2011].

The larger than expected background internal wave field found in GUTRE could be evidence of a rough topography effect. The Bathymetrist Seamount Chain located near the tracer release site (Figure 2.1) has several peaks reaching the depth of the experiment (e.g. Arrayo seamount of 284 m). The presence of rough bottom topography enhances the diapycnal diffusivity by up to one order of magnitude [e.g., *Kunze and Sanford*, 1996; *Polzin et al.*, 1997; *St. Laurent and Thurnherr*, 2007]. Hence, the seamount chain could have acted as a "hot-spot" for enhanced diapycnal mixing in GUTRE experiment. However, as the tracer release method is inherently dependent on the entire history of mixing events since the release, the presence of the "hot-spot" can only be speculated about.

2.7 Acknowledgments

We would like to thank all persons involved in the measurement of the tracer as well as the captains, crews and technicians on R/V *Maria S. Merian* and R/V *Meteor* and their home institutions for their support. We thank Jim Ledwell and Richard Greatbatch for the valuable discussions and suggestions. Support for this work came from Deutsche Forschungsgemeinschaft as part of the Sonderforschungsbereich 754 "Climate-Biogeochemistry Interactions in the Tropical Ocean"

Chapter 3

Lateral diffusivity from tracer release experiments in the tropical north Atlantic thermocline

D. Banyte, M. Visbeck, T. Tanhua, T. Fischer, G. Krahmann, J. Karstensen, prep. for submition, 2012

3.1 Abstract

Lateral diffusivity is computed from a tracer release experiment in the northeastern tropical Atlantic thermocline. The uncertainties of the estimates are inferred from synthetic particle release using a high resolution ocean circulation model. The main method employed to compute zonal and meridional components of lateral diffusivity is the growth of the second moment of a cloud of tracer. The application of an areal comparison method for tracer-based 'effective diffusivity' in the field experiments is also discussed. The best estimate of eddy diffusivity in the Guinea Upwelling region at about 300 m depth and across the mean flow is estimated to be $K_y \sim 500$ m^2 s^{-1} $(300 - 700)$. The zonal component of

lateral diffusivity is estimated to be $K_x = 1200$ m^2 s^{-1} $(600 - 1800)$. Almost twice larger K_x, in comparison to K_y, reflects the effect of zonal jets. The areal comparison method yields effective diffusivity of $K_e = 700$ m^2 s^{-1} $(500 - 900)$; the areas of tracer concentration classes increase as described by simple diffusion with diffusion coefficient of K_e. Taking into account the mean estimate of eddy diffusivity across the mean flow (K_y) and effective eddy diffusivity estimate (K_e), the effective zonal diffusivity results in about 1000 m^2 s^{-1}. The enhancement of the zonal component corresponds to the zonal jet velocities of about 0.01 m s^{-1} $(0.005 - 0.02)$, as estimated by a conceptual jet model. Finally, different sampling strategies are tested on synthetic tracer release experiments. They indicate that the best sampling strategy is a sparse regular sampling grid covering most of the tracer patch.

3.2 Introduction

The lateral dispersion of tracers in the ocean can be attributed to the interaction of molecular diffusion and 'eddy' stirring. Imposing shear and strain on a given tracer patch result in significant increase in tracer gradients [*Eckart*, 1948]. The stirring processes occur on different scales which have been grouped into three distinct stages when: 1) the tracer patch is much smaller, 2) is similar, or 3) is much larger than the size of the straining eddies [*Garrett*, 1983]. The combination of the two types of processes and different scales of eddies invoke the parametrization of lateral mixing in terms of an eddy diffusivity.

Here we estimate the integrated lateral eddy diffusivity from a tracer release experiment in the northeastern tropical Atlantic thermocline. The Guinea Upwelling Tracer Release Experiment (GUTRE) was performed in $2008 - 2010$ [*Banyte et al.*, 2012] with the injection cruise in 2008 and three tracer sampling cruises: 7, 20, and 30 months after injection. The integral timescales of the tracer used in this study are 20 and 30 months, and the spatial scales are of about 2000 km in the zonal direction and 1000 km in the meridional direction. The scales are large enough that the growth of the tracer patch can be modeled as a simple diffusive process [e.g., *Garrett*, 1983; *Ledwell et al.*, 1998; *Sundermeyer and Price*, 1998]. However, the mean velocity field prevalent in the tropical Atlantic makes

the diffusive tracer dispersion asymmetric with respect to zonal and meridional directions.

The mean circulation in the tropical North Atlantic is complicated by the alternating eastward and westward current branches, so called zonal jets, extending through the thermocline. The most pronounced eastward flowing current branches are the North Equatorial Undercurrent (NEUC) and the northern branch of the North Equatorial Countercurrent (nNECC), located at about 5°N and 9°N [*Stramma et al.*, 2005], respectively. The circulation on the eastern side of the basin, the "shadow zone region [*Luyten et al.*, 1983], however, is weaker with a prevalent anticyclonic circulation, called Guinea dome. The weak inflow of young, oxygen rich waters into the region is reflected in the older water ages found within the Guinea dome region [*Karstensen et al.*, 2008; *Schneider et al.*, 2012], especially at a depth of about 500 m. Moreover, the oxygen consumption rate is much larger at the surface than in the deep; it falls off with depth by a factor of 10-50 between 100-1000 m [e.g. *Jenkins*, 1987; *Karstensen et al.*, 2008]. The sluggish circulation at relatively shallow depths, where oxygen consumption is large, results in regions of especially low oxygen levels, so called, oxygen minimum zones (OMZ).

The zonal jets in combination with mesoscale eddies play an important role in transporting oxygen rich waters into the region. In the wake of significant deoxygenation observed in the zone [*Stramma et al.*, 2008], the estimation of lateral eddy diffusivity and zonal advection are required to project the future oxygen development. *Fischer* [2012 submitted], after computing the vertical oxygen influx and comparing it with the conseptual oxygen consumption model by *Karstensen et al.* [2008], suggests that about 70% of the total oxygen supply is coming by lateral pathways.

There are no observationally based lateral eddy diffusivity estimates in the Guinea Upwelling region thermocline up to date. However, in the neighboring region to the north, at about 25°N, the North Atlantic Tracer Release Experiment [*Ledwell et al.*, 1998] was carried out in $1991-93$ to estimate lateral eddy diffusivities in the thermocline. The tracer release experiment was accompanied by the subsurface floats, resulting in meridional diffusivity component (K_y) of 650 $m^2\ s^{-1}$ (200 to 1200) from the tracer [*Ledwell et al.*, 1998] and 700 ± 400 m^2

s^{-1} from the floats [*Sundermeyer and Price*, 1998]. Zonally, the estimates were larger: 2300 m^2 s^{-1} (1000 to 4000) from the tracer and 1500 ± 700 m^2 s^{-1} from the floats. However, the high-resolution models suggest that in the tropical ocean the eddy diffusivities should be substantially smaller [*Eden and Greatbatch*, 2008; *Eden et al.*, 2007].

The paper is organized as follows: section 2 describes the three methods applied to the tracer patch to estimate lateral eddy diffusivity coefficient, section 3 lists three datasets, one of which is observational and two are modeled tracer releases. Finally, the results are given in section 4 and discussed in section 5.

3.3 Methods

In this study, three methods are employed to estimate lateral eddy diffusivity. All analyze a tracer distribution after spreading from a point source and estimate an average lateral diffusivity at a specific time moment. Two methods describe the growth of the second moment of a cloud of tracer while they differ only in the way the second moment is estimated: either from the Gaussian distribution fit to the data [e.g., *Ledwell et al.*, 1998], or by the computation of the centered second moment of particles weighted by the amount of tracer [e.g., *Klocker et al.*, in press; *Sundermeyer and Lelong*, 2005]. Both methods yield the zonal and meridional components of lateral diffusivity. The third method is an areal comparison method for tracer-based 'effective diffusivity'. It relies on the comparison of areas of the tracer classes between the observed tracer field with that described by an isotropic Gaussian distribution.

All three methods applied to estimate lateral eddy diffusivity rely on the assumption that on large scales, the second moment of the tracer cloud increases linearly in time [*Garrett*, 1983]. Along-isopycnal two-dimensional dispersion (variance) is then described by Fick's diffusion: $var(C)|_{x,y} = 2K_{x,y}t$, where C is the tracer concentration, i.e., tracer column inventory in units of mol m^{-1}, K_x and K_y are zonal and meridional components of lateral eddy diffusivity. The effective eddy diffusivity, assumed to be isotropic, is labeled as K_e.

3.3.1 Second moment of a cloud of tracer

3.3.1.1 The Gaussian Fit Method

The growth of the second moment of a cloud of tracer can be estimated by fitting a Gaussian distribution to the tracer patch: $var(C) = \sigma_{x,y}^2$, where σ_x and σ_y represent the half widths along zonal and meridional directions, respectively. The method was, for example, applied in the North Atlantic tracer release experiment (NATRE [*Ledwell et al.*, 1998]). In this study, to obtain the mean lateral diffusivity estimates, we first averaged the tracer patch either zonally or meridionally, and then applied a 1D Gaussian fit to each of the mean curves. In the tropical Atlantic, where zonal jets elongate the tracer patch in x direction, the zonal component (σ_x) is expected to be much larger than its meridional counterpart (σ_y). The results of this technique will be labeled G (for Gaussion fit) in the following.

3.3.1.2 The Weighted Particle Method

An alternative way to estimate the second moment of a cloud of tracer is via weighted particle dispersion. For example, in the zonal direction:

$$\sigma_x^2 = \frac{\sum_{i=1}^{N}(x_i - x_c)^2 C(x_i)}{\sum_{i=1}^{N} C(x_i)},$$

where N is the number of particles, $C(x_i)$ is the weight (tracer amount found in the location), and x_c is the center of mass in the zonal direction of the tracer patch:

$$x_c = \frac{\sum_{i=1}^{N} x_i C(x_i)}{\sum_{i=1}^{N} C(x_i)}.$$

The results of this technique will be labeled P for Particle method.

Both ways to compute the second moment of a tracer patch are compared because it is expected that the Gaussian fit method is less sensitive to gaps in the data and to possible outliers. On the other hand, the assumption that a tracer patch distribution is Gaussian might be too restrictive and therefore the fit is less robust and associated uncertainties are larger.

3.3.2 Effective eddy diffusivity

The computation of tracer-based 'effective diffusivity' in this study uses the 'area comparison' method based on the ideas of *Nakamura* [1996], who introduces an area coordinate and takes into account the increasing gradients along the tracer contour stretched by advection, when computing an effective diffusivity. The method was used in previous studies for the particle release simulations [e.g., *Klocker et al.*, in press; *Marshall et al.*, 2006]. In sparsely sampled field experiments, the *Nakamura* [1996] method cannot be directly applied. Instead, effective eddy diffusivity (K_e) is computed by comparing areas of tracer concentration classes in the tracer patch with those of the idealized tracer patch described by Fickian diffusion with an isotropic diffusion coefficient.

Depending on the sampling frequency, either 50 or 20 tracer concentration classes are chosen ranging from zero to the maximum concentration in the studied tracer patch. The area-concentration function ($A(C)$) is described as:

$$A(C) = \sum_{C_{max}}^{C} a(c),$$

where C_{max} is a maximum tracer concentration found in the patch, $a(c)$ is the area of c concentration class. Hence, function $A(C)$ is a cumulative area distribution of tracer concentration classes; it describes the total area of the tracer patch with higher concentrations than a chosen limit (C). The inverse of the function indicates the total amount of tracer found in the chosen area. The inverse function might be however more difficult to compute directly.

After constructing the area-concentration function ($A(C)$) for the tracer patch, we compare it with the range of functions computed for the idealized tracer patch described by Fickian diffusion with an isotropic diffusion coefficient. The best fit is searched in the range of isotropic diffusivities (K_e) from 140 $m^2\ s^{-1}$ to 1560 $m^2\ s^{-1}$ with a step of 20 $m^2\ s^{-1}$. A rather large diffusivity step is chosen because the uncertainty of the estimates is expected to be much larger for the sparsely sampled tracer patch.

The advantage of the method is that it is less sensitive to the geometrical shape of the tracer patch than are the previously discussed methods to estimate

lateral diffusivities. In general, the K_e estimates are expected to be in the range between meridional and zonal estimates of lateral diffusivity. Moreover, when tracer distribution is described by Fickian diffusion but with $K_x \neq K_y$, the relation holds: $K_e^2 = K_x K_y$, as derived from the area of ellipse formulation. In cases where K_e^2 is smaller than $K_x K_y$, estimated using other two methods, we expect that estimates of K_x and K_y are affected by tracer patch geometry. Similarly, having K_e and K_y, effective K_x can be computed, which is an effective mixing caused by zonal jets stretching tracer patch, increasing tracer gradients, and hence increasing mixing.

3.4 Data

The main objective of this study is to estimate lateral eddy diffusivity from the observations of the tracer release experiment, where tracer sampling was irregular and spatially limited. In order to estimate uncertainties in the results, two synthetic tracer releases were modeled and analyzed.

Three datasets were used in the study: 1) from synthetic tracer release in conceptual jet model, 2) from synthetic particle release in high-resolution ocean circulation model, and 3) from the observations of the tracer release experiment conducted in the northeast tropical Atlantic in the Guinea upwelling region. The details of these experiments are given below.

3.4.1 Conceptual jet model

The tracer release experiment is simulated using a conceptual jet model, which is described by the advection-diffusion equation as follows:

$$\frac{\partial C}{\partial t} + u\frac{\partial C}{\partial x} + v\frac{\partial C}{\partial y} = K_x\frac{\partial^2 C}{\partial x^2} + K_y\frac{\partial^2 C}{\partial y^2}, \tag{3.1}$$

where C is tracer concentration and the value of the isotropic eddy diffusivity coefficient is chosen as $K_x = K_y = 400$ m^2 s^{-1}. The non-divergent velocity field is defined as $u = -\partial\psi/\partial y$ and $v = \partial\psi/\partial x$, where the streamfunction ψ is

$$\psi = u_0 sin(2\pi y/l_y) sin(2\pi x/l_x).$$

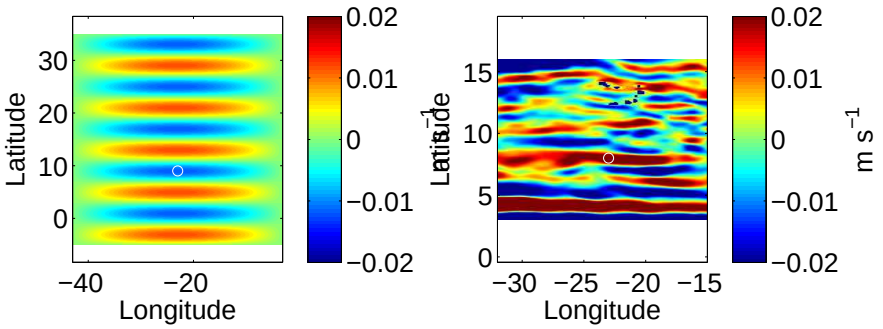

Figure 3.1: Velocities in conceptual jet model (left) and in FLAME model (right), averaged over 53 instanteous velocity fields, each - one week apart.

Here, the velocity at the center of the zonal jet was chosen to be $u_0 = 0.01$ m s^{-1}, while l_x and l_y represent the period of periodically alternating jets in the zonal and meridional directions, respectively. In the boundary range of $x = [3°\text{W}\ 43°\text{W}]$ and $y = [12°\text{S}\ 28°\text{N}]$, we chose $l_x = 40°$ and $l_y = 4°$. In this way, there were ten stacked zonal jets in the domain (Figure 3.1). The tracer release position was either at 8°N 23°W or at 7°N 23°W corresponding to either the location directly between the two jets or in the middle of a jet.

3.4.2 General circulation model (FLAME)

The particle releases were simulated using output of the high-resolution ($\frac{1°}{12}$) ocean model FLAME (Family of Linked Atlantic Model Experiments) [*Dengg et al.*, 1999]. FLAME is based on a modified version of the $z-$coordinate Modular Ocean Model (MOM2) [*Pacanowski et al.*, 1995] and has been set up for the Atlantic Ocean between 70°N and 18°S [e.g., *Eden and Böning*, 2002]. The particle release simulations used a horizontal grid of $\frac{1°}{12}$ and 45 vertical levels with a resolution decreasing towards greater depths. More detailed information of the model configuration is given in the work of *Hüttl-Kabus and Böning* [2008].

The model has been used previously for several studies in the Tropical Atlantic, e.g., in the works of *Hüttl and Böning* [2006], *Kirchner et al.* [2009], *Brandt and Eden* [2005]. The study of *Kirchner et al.* [2008] included a detailed model data comparison, indicating realistic model behavior with respect to the observed mean tracer transport and its variability. Furthermore, FLAME reproduces the

zonal current bands reasonably well (Figure 3.1), even though modeled velocities of the current bands fall below observed velocities at greater depths [*Stramma et al.*, 2005].

The tracer patch was represented by an ensemble of particles passively transported by the FLAME velocity output at a depth of 250 m [*Fischer*, 2007]. A typical tracer release simulation consisted of about 10,000 particles whose position and velocities were traced over almost 30 months (132 weeks). Overall, 53 particle releases were used in this study, each of them starting at the same position of 8°N 23°W. Different particle releases were performed a week apart in response to the different instantaneous flow conditions. Examples of the two, out of 53, tracer patch simulations at time intervals of 20 and 30 months after the tracer release are shown in Figure 3.2. Chosen time periods correspond to the two surveys of the observed tracer release experiment in the northeastern tropical Atlantic (GUTRE).

3.4.3 The Guinea Upwelling Tracer Release Experiment

The Guinea Upwelling Tracer Release Experiment started with 92 kg of tracer, halocarbon trifluoromethyl sulfur pentafluoride (CF_3SF_5), being released at 8°N 23°W in April 2008. The release isopycnal was $\sigma_\Theta = 26.88$ kg m^{-3}, corresponding to a depth of about 350 m. The spreading tracer was sampled during three subsequent surveys: 7, 20, and 30 months after the tracer release. The experiment was primarily designed to estimate the diffusivity across the isopycnals, results of which are described by *Banyte et al.* [2012]. In this study, however, we estimate the large scale, time integrated, eddy diffusivity parameters. Respectively, we analyzed only the surveys performed 20 and 30 months after tracer release, where tracer patch extent reached more than 1,000 km (Figure 2.4) and patches were well spatially homogenized.

The contour maps of the tracer column integrals (Figure 3.3) were interpolated using Gaussian weights, where the meridional radius of influence was chosen arbitrarily to be 25 km (first survey) and 100 km (second and third surveys); correlation scales are expected to be larger than 100 km in the 20-30 months old tracer patch [*Ledwell et al.*, 1998]. The zonal radius of influence was twice as

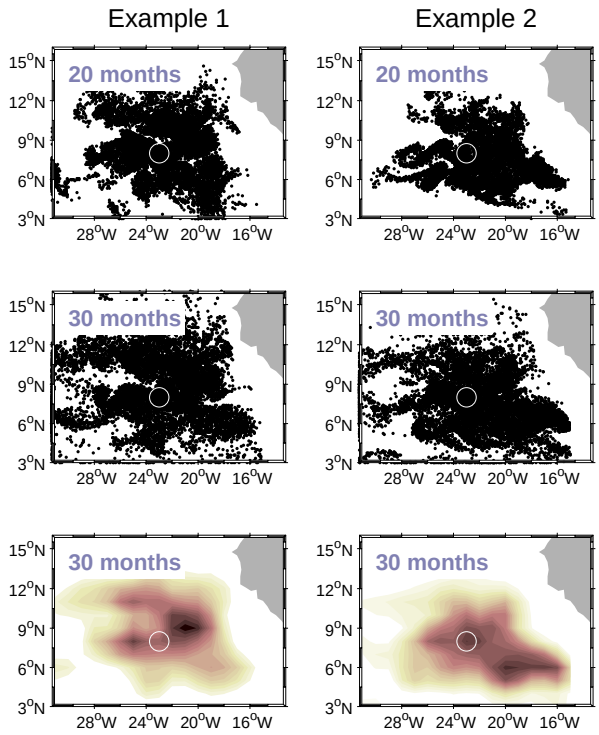

Figure 3.2: Examples of two particle releases at 250 m depth in high resolution ocean model FLAME at time intervals: 20, and 30 months after the tracer release. Bottom: the same examples at 30 months interpolated with Gaussian weights as was applied for GUTRE data.

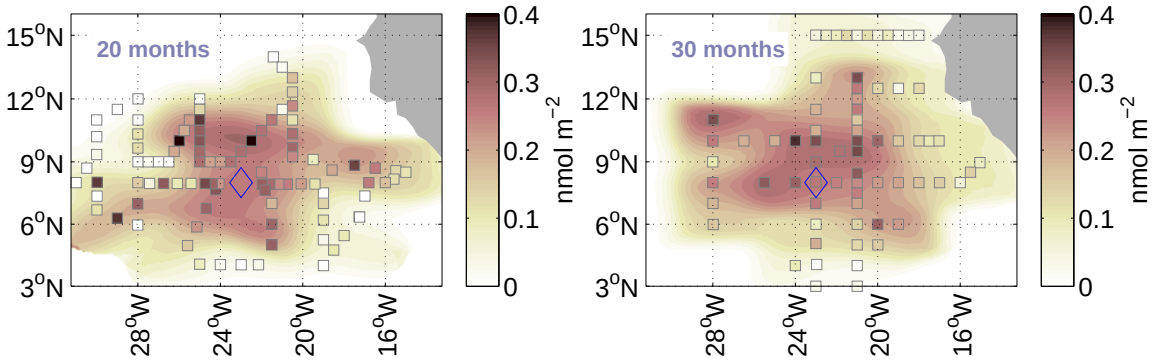

Figure 3.3: Horizontal tracer patch distribution during three surveys: (left) in December 2009 (20 months after tracer release) and (right) in October–November 2010 (30 months after tracer release). The color of the squares represents the tracer column integral; the same colorbar applies to the filled contours. The blue circle at 8°N, 23°W marks the tracer injection position, but the symbol is larger than the 20 km by 20 km area of the injection.

large. Furthermore, the zeros were assigned at a cut-off radius distance from the nearest cast position; the cut-off radius being two times the radius of influence.

A visual inspection of the tracer patch during the second and third surveys indicates that the center of mass of the tracer patch is not significantly shifted with respect to the tracer release position (Figure 3.3). This finding agrees with the notion of the shadow zone, or entrapment of the tracer in the region. The zonal extent of the tracer patch is larger than the meridional extent in both surveys. Furthermore, the high tracer column inventories found at 28°W during the 30 months survey indicate that the patch extended westward beyond the farthest sampled longitude. The limited spatial extent of the sampled tracer region is expected to have an influence to the zonal eddy diffusivity estimates.

3.4.4 Sampling strategies

In this study, several tracer sampling grids are used. The fine resolution grid applied for the modeled data is $0.3° \times 0.3°$. In the case of the particle release in the FLAME model, we converted particles to concentrations by averaging the number of particles over the grid size. A fine sampling resolution of 0.3° is not possible to achieve in the field experiments because of time limitations, therefore,

coarser sampling resolution strategies were tested.

The partial dataset in modeled tracer releases was constructed by resampling the original fine resolution grid using $1° \times 1°$ grid, $2° \times 2°$ grid, or applying the sampling strategy of the GUTRE to the FLAME experiments. In the case of regular partial dataset, we used to shift the 1° or 2° sampling grid over the fine grid to get the uncertainty of the mean diffusivity estimates. The two standard deviations were chosen as uncertainty ranges of the estimates.

The lateral diffusivities were also computed along separate transects of the tracer patch. For the fine resolution data the transects were computed along the cross-section of each longitude and latitude 0.3° appart, for the sparse resolution - each 1° or 2° appart. In GUTRE experiment, only several well sampled transects are available.

3.5 Results

3.5.1 Conceptual jet model

The tracer release is simulated in the velocity field with parametrized isotropic eddy diffusivity of $K_x = K_y = 400$ m^2 s^{-1} and overlaid alternating zonal advection with the meridional period of 4° and maximum velocity in the middle of the jet of 0.01 m s^{-1}. The tracer spread is described by equation 3.1. There are two examples compared: when the tracer is released in the middle of the zonal jet and in between the zonal jets.

3.5.1.1 Full dataset

The Gaussian fit and weighted particle methods yield similar mean eddy diffusivity estimates in zonal (K_x) and meridional (K_y) directions. Furthermore, the meridional result corresponds well with the imposed eddy diffusivity in the model of 400 m^2 s^{-1}, the difference being only about 10 m^2 s^{-1} (Table 3.1). The zonal component (K_x) affected by the zonal advection is, on the other hand, at least three times larger (about 1300 m^2 s^{-1}).

How much the zonal diffusivity estimate is a result of geometric stretch of the patch, as compared to the enhanced mixing in zonal direction by increasing

tracer gradients, can be answered by computing effective eddy diffusivity (K_e). K_e estimate computed for the two examples is about $K_e = 750$ m^2 s^{-1} (Table 3.1). Comparing the results of different methods: $K_e^2 \approx K_x K_y$, from which we conclude that in the two examples the zonal jets do not simply stretch the tracer patch, but enhance mixing in the zonal direction.

Additionally, we employ the Gaussian fit and weighted particle methods to estimate diffusivity parameters along each longitudinal or latitudinal transect of the gridded tracer patch. The transect analysis shows that K_x and K_y estimates vary significantly (Figure 3.4 c-f). As the tracer patch is constantly advected by the alternating mean flow, the tracer at some places stays longer than in the others. For example, K_x differs by at least 3 times (K_y vary even up to 5 times) from the center of the patch to the boundaries. Hence, trying to avoid underestimation, the best is to choose such transects, which cross the areas where the tracer stayed the longest: in this case, the transects crossing the tracer release position.

3.5.1.2 Partial dataset

The tracer field was partially sampled using a sparse regular grid of 1° or 2°. All three methods were found to be robust enough to recover the diffusivity parameters in the range of uncertainties (Table 3.1). The uncertainty was slightly increasing with the sparser grid. However, even with the sampling grid of 2° the uncertainty of the estimates is small: often only 1% of the value.

Even with the sparse sampling of the 1° grid, the number of stations required to cover the full tracer patch in the two examples are about 140. The rule of the thumb is that about 100 measurement casts spaced over regular 2° grid require about a month to complete. Here it is taken into account that the ship driving speed is about 10 kn and the time spent over a measurement cast is about 1.5 hours. Hence, to cover a full tracer patch is a challenge for an open ocean survey of about one month length. Decreasing the size of the studied area, however, significantly effects the mean eddy diffusivity estimates (Figure 3.5).

The sampling area enclosing about 90% of the total tracer amount results in about 10% deviation in diffusivity estimate. The area can be covered with 80

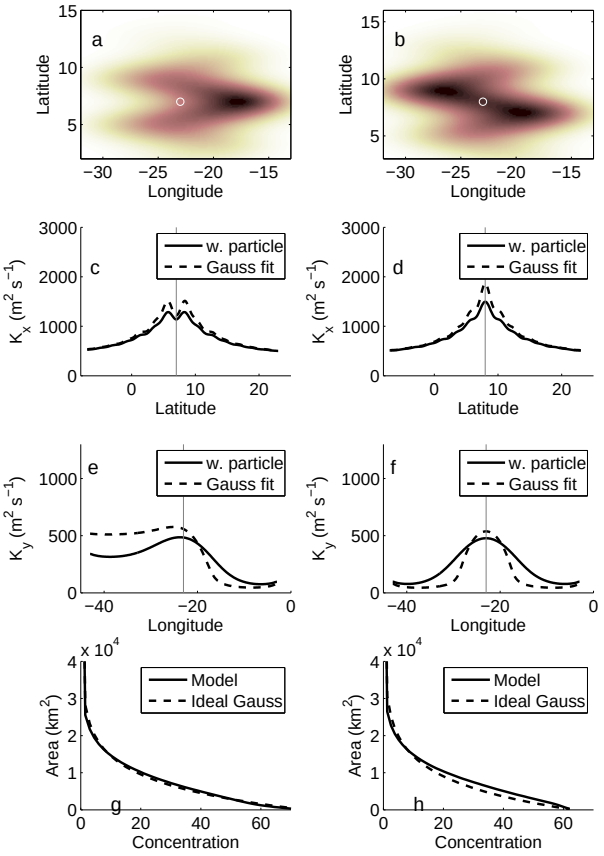

Figure 3.4: Two examples of synthetic tracer release in conceptual jet model at 30 months, where a tracer is released in a) the middle of the zonal jet, b) in between of two zonal jets. The tracer release position is marked by a white circle. The zonal (c - d) and meridional (e - f) components of the eddy diffusivity are computed along each transect line. Cumulative area-concentration function (g-h) computed for the synthetic tracer release (thick black line) and its best fit computed for the isotropic Gaussian distribution (dashed line).

	Full		1°		2°	
(m^2 s^{-1})	MJ	BJ	MJ	BJ	MJ	BJ
K_{xP}	1230	1300	1229	1298	1246 ± 12	1315 ± 12
K_{xG}	1410	1510	1411	1506	1434 ± 16	1515 ± 16
K_{yP}	410	410	408	407	408 ± 1	408 ± 1
K_{yG}	410	410	413	411	415 ± 2	414 ± 2
K_e	720	780	$720(\pm 0)$	800 ± 20	720 ± 20	790 ± 20

Table 3.1: Eddy diffusivities for the two examples (tracer release in the middle of the jet (MJ) or between the jets (BJ)) of synthetic tracer release in conceptual jet model using a full dataset and sampling grids of 1° or 2°. Here, K_{xP} and K_{yP} are eddy diffusivities from weighted particle method, K_{xG} and K_{yG} - from Gaussian fit method, and K_e is an effective eddy diffusivity.

stations using a sparse 2° sampling grid. In comparison, when only 50% of the total tracer amount is found at the center of the patch, the deviations reach about 50% of the full field estimates. Furthermore, the sampling grid of 1° give similar results. We conclude that both Gaussian fit and weighted particle methods both yield good results for the homogeneous tracer patch as long as large enough region is sampled.

3.5.2 General circulation model (FLAME)

The uncertainty of the eddy diffusivity estimates and the best tracer patch sampling strategy might be different when applied on the more realistic example of the tracer patch evolution. The tracer released as a cloud of particles in the high resolution ocean circulation model (FLAME) allows to test the performance of each of the three eddy diffusivity computation methods on the partially sampled tracer field where tracer spread is not homogeneous.

3.5.2.1 Full dataset

Eddy diffusivity was first computed with the full dataset and fine grid for each of the 53 synthetic tracer releases in FLAME model (Figure 3.6). Both Gaussian fit and weighted particle methods result in noisy estimates at the early stages of tracer patch development, but after about 20 months the estimates converge. Averaged over the time period of 20 to 30 months (90-132 weeks) and combining

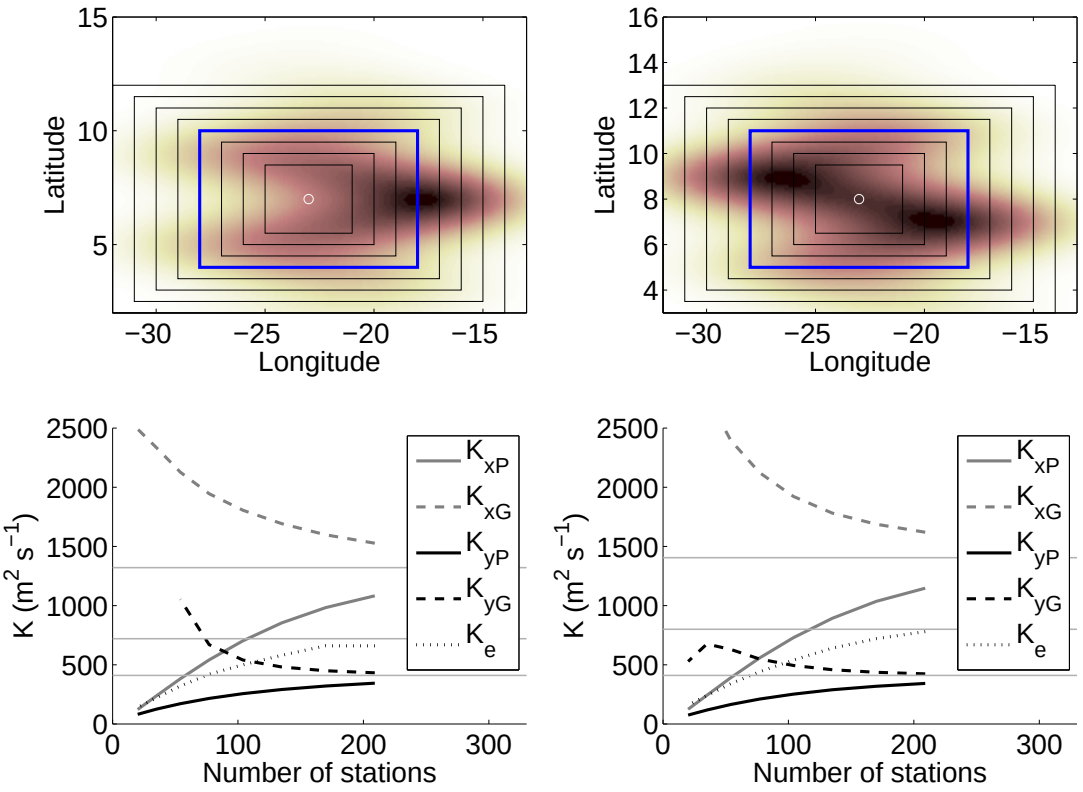

Figure 3.5: Eddy diffusivities versus the number of stations for the same two examples as in Figure 3.4, where a tracer is released in the middle of the zonal jet (left) and in between of two zonal jets (right). The sampling grid is 1°. The boundaries of the minimum size regions resulting in estimate deviations of less than 50% are marked in blue (top). Three paralel green lines, from tom to bottom, indicate the mean estimates of the full dataset of K_x, K_e, and K_y, respectively. Here, K_{xP} and K_{yP} are eddy diffusivities from the weighted particle method, K_{xG} and K_{yG} - from the Gaussian fit method, and K_e is an effective eddy diffusivity.

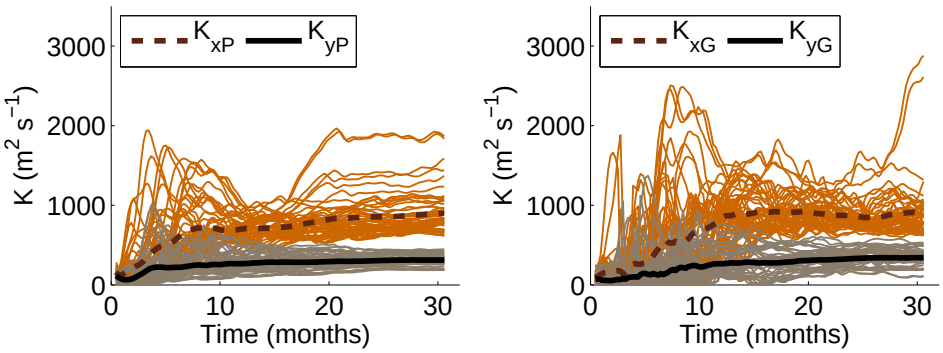

Figure 3.6: Zonal (K_x) and meridional (K_y) components of eddy diffusivity estimated at each one week time interval for each of the 53 different tracer releases in FLAME model and their mean. The estimates are computed either using weighted particle method (left figure, marked by P), or Gaussian fit method (right figure, marked by G).

the results of the two methods, the mean lateral diffusivity is obtained for the FLAME model: $K_x = 870 \pm 100$ m^2 s^{-1}, and $K_y = 320 \pm 30$ m^2 s^{-1} (see also Table 3.2). The much larger zonal diffusivity component infers to the effect of the zonal jets stretching the tracer patch.

The effective eddy diffusivity estimates for each of the 53 tracer release experiments are noisy at the earlier times, as well. The high variability in the estimates is a result of the discrete sampling grid of the patch (0.3°), when only very high concentrations or very low concentrations are observed. The results are slightly increasing with time and reach a plateau after about 20 months (Figure 3.7). Averaged over the time period of 20 to 30 months (90-132 weeks), the mean estimate is $K_e = 335 \pm 21$ m^2 s^{-1}. Here, differently than in the conceptual jet model experiments, K_e is similar to meridional eddy diffusivity component (K_y) and $K_e^2 \ll K_x K_y$. The well developed tracer patch, at time scales of 20 to 30 months, evolves similarly to the tracer patch of isotropic Gaussian distribution with a diffusion coefficient close to K_y. The mean advection only geometrically deforms the patch without significantly increasing mixing.

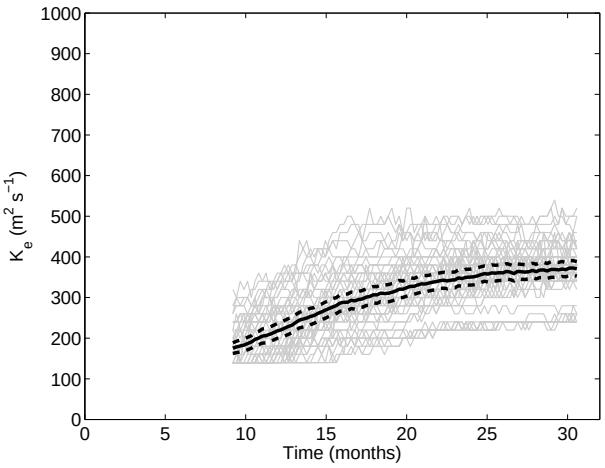

Figure 3.7: Effective eddy diffusivity estimated at each one week time interval for each of the 53 different tracer releases in FLAME model and their mean (black solid line). The error bars (black dashed line) are computed as a standard error at each time period of all 53 runs.

3.5.2.2 Partial dataset

The tracer patch evolution in FLAME model is less homogeneous than in the synthetic tracer release in conceptual jet model. We chose two random example runs out of 53 to explore the differences in diffusivity estimates with the sampling grid of 1° and 2° at a time period of 30 months (Figure 3.8). The diffusivity estimates in one example are similar to the ensemble mean, while in the other they are slightly larger (Table 3.2).

Both coarse sampling strategies yield the results little deviating from the fine grid diffusivity estimates. The uncertainties using 2° sampling grid are about twice larger than using 1° grid. Furthermore, the Gaussian fit method yields almost twice larger uncertainties and is associated with the additional error of the fit when the profiles deviate from the Gaussian distribution. Overall, the uncertainty of zonal diffusivity estimates (K_x) is found in the range of 300 m^2 s^{-1} and about 100 m^2 s^{-1} for the meridional estimates (K_y) (Table 3.2). The uncertainty ranges are in a similar range when computed for the other examples of the 53 experiments.

In both examples the effective eddy diffusivity closely agree with the meridional estimate (K_y). Moreover, even using a sparse 2° grid the method recovers

	Av. 53 runs	Ex1			Ex2		
(m^2 s^{-1})		Full	1°	2°	Full	1°	2°
K_{xP}	860 ± 76	1270	1410 ± 150	1340 ± 370	750	780 ± 100	770 ± 200
K_{xG}	880 ± 60	860	1050 ± 370	940 ± 620	790	800 ± 170	780 ± 400
K_{yP}	305 ± 19	450	440 ± 50	450 ± 120	350	360 ± 60	350 ± 120
K_{yG}	330 ± 28	500	430 ± 170	460 ± 340	420	430 ± 130	420 ± 230
K_e	335 ± 21	490	500 ± 70	490 ± 110	360	370 ± 60	370 ± 140

Table 3.2: Eddy diffusivities in FLAME model, either averaged over 53 runs and the time period of 20 to 30 months (87-132 weeks), or computed for the two examples and at the time period of 30 months (132 weeks). For the two examples, the diffusivities are computed for the full dataset, or after the tracer patch was sampled using the regular sampling grid of 1° or 2°. Here, K_{xP} and K_{yP} are eddy diffusivities from weighted particle method, K_{xG} and K_{yG} - from Gaussian fit method, and K_e is an effective eddy diffusivity.

the estimates of the full dataset within the uncertainty range of about 100 m^2 s^{-1}. Hence, the method is robust enough to yield relatively good estimates with the sparse sampling grid even for the less homogeneous tracer patches of FLAME model.

The transect analysis of the two examples was carried after the patches were sampled with 1° grid (Figure 3.8). The analysis shows large variability of K_x and K_y estimates along the transects. Despite the large variability, the transects near the release site, where tracer is expected to linger the longest, yield the results closer to the fine grid estimates. Hence, when the lateral diffusivity estimates must be judged from several transects alone, the ones near the center of mass of the tracer patch, in this case, near the release site, must be chosen.

In addition to reducing the sampling frequency, the smaller sampled region can help to limit the number of stations required to cover the region. The reduction of the sampled area, however, significantly increase the deviation of the estimates (Figure 3.9). Here again the two examples are analyzed with the 1° sampling grid. When the sampled region covers about $50 - 70\%$ of the total amount of the released tracer, the diffusivity estimates deviate about 50% from the full field estimates. Similar conclusion is drawn from the 2° sampling strategy. We conclude that in the field experiments the coarse grid of 2° yields good diffusivity results as long as most of the tracer patch is sampled.

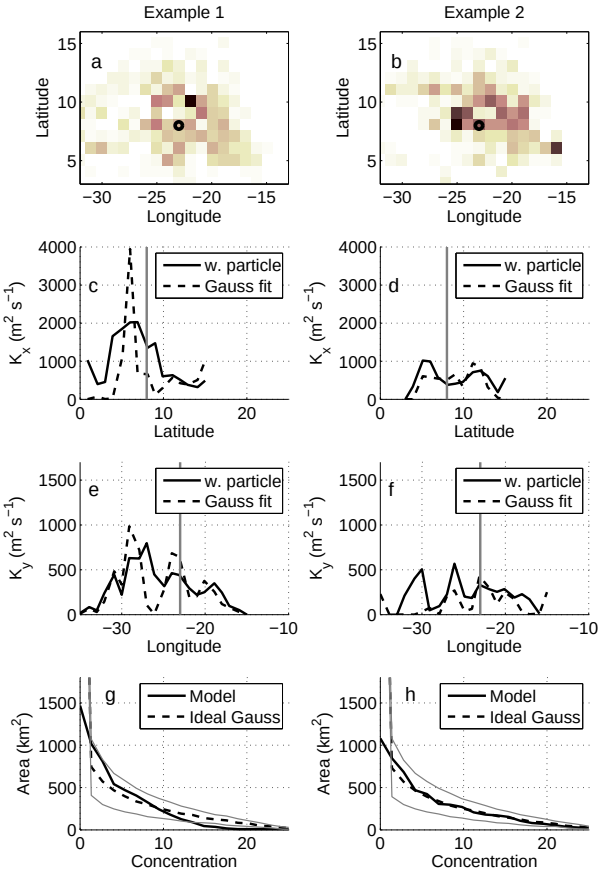

Figure 3.8: Two random examples from the 53 synthetic tracer releases in FLAME model at a time period of 30 months sampled with the grid of 1°. The tracer release position is marked by a black circle. The zonal (c - d) and meridional (e - f) components of the eddy diffusivity are computed along each transect line. Cumulative area-concentration function (g-h) computed for the synthetic tracer release (thick black line) and its best fit computed for the isotropic Gaussian distribution (dashed line). Thin gray lines indicate the 100 m^2 s^{-1} deviation from the best estimate.

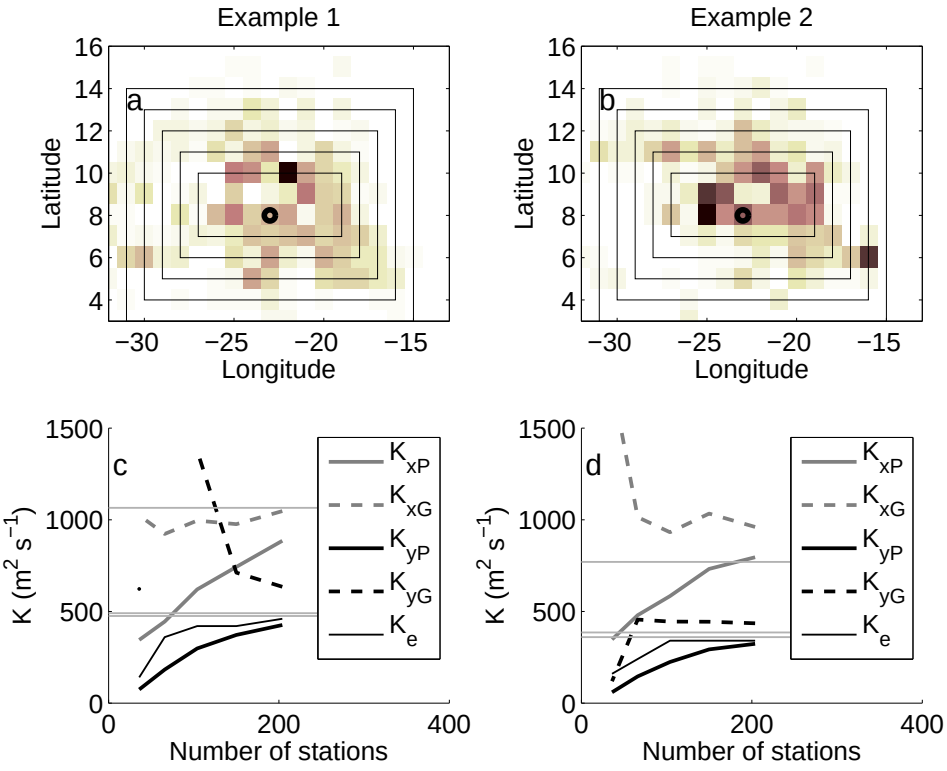

Figure 3.9: Eddy diffusivities computed when a sampled area is limited (black rectangles) for the same two examples as in Figure 3.8. The number of stations, using 1° sampling grid, are counted in each of the bounded areas. The paralel gray lines indicate the mean diffusivity estimates for the whole field and fine sampling grid. Three paralel green lines, from tom to bottom, indicate the mean estimates of the full dataset of K_x, K_e, and K_y, respectively. The eddy diffusivity computation methods are weighted particle (e.g. K_{xP}), Gaussian fit (e.g. K_{xG}), and area comparison (K_e).

3.5.3 The Guinea Upwelling Tracer Release Experiment

The 20 and 30 months surveys of GUTRE were analyzed in this study. We used irregularly sampled data either directly to compute the estimates, or after interpolating with Gaussian weights (contours in Figure 3.3). The interpolation procedure is described in section 3.4.3.

Meridional eddy diffusivity estimates, in non-interpolated data analysis, agree well between the two surveys (Table 3.3) being in the range of $K_y = 320$ m^2 s^{-1}. The zonal diffusivity component (K_x), on the other hand, is estimated much smaller in the third survey than in the second survey. The difference is a consequence of the limited westward extent of the patch in the third survey (Figure 3.3). In comparison, the second survey, which covered the zonal tracer expansion much better, resulted in a larger zonal diffusivity estimate of about $K_x = 1170$ m^2 s^{-1}.

The diffusivity estimates for the interpolated data are larger as a consequence of smoothing. However, the interpolated data fills the gaps in the sampled area, hence reduce noise in the estimates. The results are similar between the surveys for both zonal and meridional diffusivity components: $K_y \simeq 440$ m^2 s^{-1}, and $K_x \simeq 1100$ m^2 s^{-1}. In addition, the area comparison method can be applied to the interpolated data. The estimated effective diffusivity is about 1000 m^2 s^{-1} and is close to K_x estimate, instead of K_y.

To judge on the uncertainty of the calculated eddy diffusivity coefficients in GUTRE, its sampling strategy was applied to each of the 53 simulated tracer releases in FLAME model. For a non-interpolated dataset, the meridional diffusivities are about 40% smaller than the results obtained using the fine grid and full dataset (Figure 3.10 and Table 3.3) for both surveys. The zonal eddy coefficients are in a relatively good agreement with the full field estimates with the sampling strategy of the second survey in GUTRE. With the sampling strategy of the third survey, however, K_x estimates are about three times (65%) smaller then the full dataset estimates. Similarly, we expect that GUTRE results with the non-interpolated data are slightly underestimated, while K_x estimate in the third survey can be considered unreliable.

For an interpolated dataset, K_x and K_y estimates are almost in the range of

	20 m.	GUTRE	30 m.	GUTRE	20 m.	FLAME	30 m.	FLAME
(m^2 s^{-1})	NI	I	NI	I	NI	I	NI	I
K_{xP}	1110	1050	530	980	660 ± 40	980 ± 50	340 ± 20	680 ± 20
K_{xG}	1230	1230	290	1260	940 ± 70	1190 ± 80	270 ± 20	850 ± 40
K_{yP}	280	340	390	450	180 ± 20	320 ± 30	200 ± 20	270 ± 20
K_{yG}	310	440	320	530	220 ± 20	380 ± 40	180 ± 20	320 ± 20
K_e	–	1120	–	900	–	520 ± 30	–	450 ± 10

Table 3.3: Eddy diffusivities computed for GUTRE second (20 months) and third (30 months) surveys, from not interpolated (NI) and interpolated (I) data, in comparison to lateral diffusivities and their uncertainties computed using GUTRE sampling strategy for each of the 53 tracer release experiments in FLAME model, from interpolated (I) and not interpolated (NI) data. Here, K_{xP} and K_{yP} are eddy diffusivities from weighted particle method, K_{xG} and K_{yG} - from Gaussian fit method, and K_e is an effective eddy diffusivity.

uncertainties with the full field estimates. The effective eddy diffusivity (K_e), on the other hand, is about 35% and 25% overestimated for the second and third surveys, respectively (Figure 3.11). We therefore expect slight overestimation in GUTRE's K_e as well.

Furthermore, it is worth to take a look into the results of several transect profiles done in each survey. The model results indicate that transect analysis can both overestimate and underestimate the true eddy diffusivity parameters. Nevertheless, the results agree better when transects are crossing the center of the patch, which in GUTRE experiment can be considered the tracer release position, because the center of mass of the tracer is expected to move little over time. In this way, K_y estimates are found to vary between 200 to 600 m^2 s^{-1} in both surveys, while K_x estimates vary between 1000 to 2000 m^2 s^{-1} in the second survey (Figure 3.12 and 3.13).

In conclusion, the transect analysis and simulations using FLAME model indicate that the GUTRE eddy diffusivity estimates are in the range of $K_x = 1200$ m^2 s^{-1} $(600 - 1800)$ for zonal eddy diffusivity coefficient and $K_y = 500$ m^2 s^{-1} $(300 - 700)$ for meridional diffusivity coefficient. The best estimate of effective eddy diffusivity is $K_e = 700$ m^2 s^{-1} $(500 - 900)$. Here the uncertainty is double the size of the uncertainties computed with the regular sampling grid of 2° in FLAME model, because we expect that the uncertainty increase with the irregular

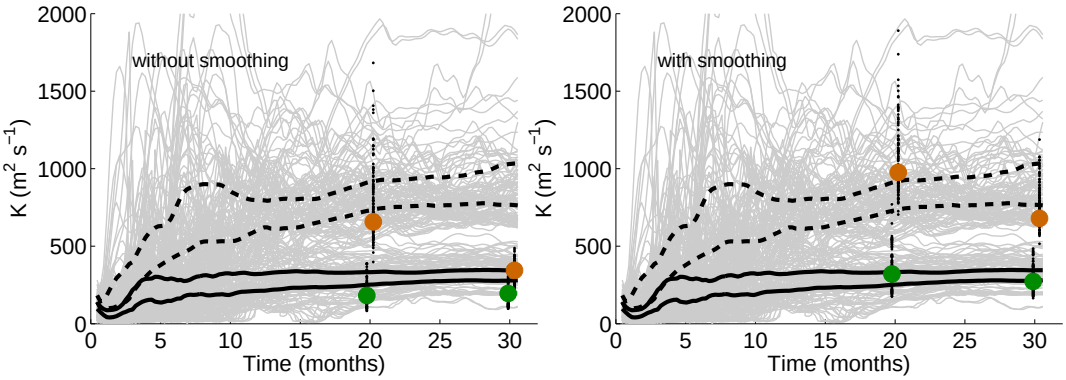

Figure 3.10: Eddy diffusivity estimates for each of the 53 tracer simulations in FLAME model, but with the sampling strategy of GUTRE at 20 and 30 months after tracer release: not interpolated dataset (left), interpolated dataset (right). The mean of each estimate is marked by a circle (brown for K_x estimates and green for K_y estimates) and slightly shifted in time. Both Gaussian fit and weighted particle methods are over-plotted. Thin gray lines mark K_x and K_y estimates for each run as in Figure 3.6. Black solid lines mark the uncertainty ranges of mean K_y estimate, while black dashed lines mark the uncertainty ranges of mean K_x estimate.

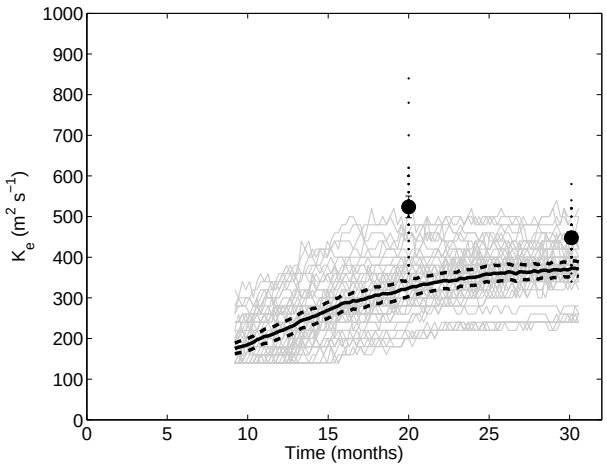

Figure 3.11: Effective eddy diffusivity for each of the 53 tracer simulations in FLAME model but with the sampling strategy of GUTRE after smoothing with Gaussian weights (black dots) and their mean (black circle). Thin gray lines mark K_e estimates for each experiment as in Figure 3.7.

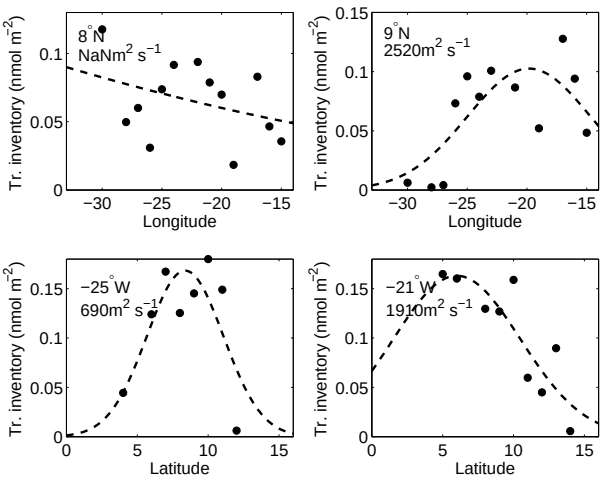

Figure 3.12: Gaussian distribution fit (dashed line) to four tracer patch transects along: 8°N, 9°N, 25°W, and 21°W (black dots), during the second GUTRE's survey (20 months).

sampling grid.

3.6 Conclusions and discussion

The Guinea Upwelling Tracer Release Experiment provides the first observational lateral diffusivity estimate in the thermocline of the northeastern tropical Atlantic. In comparison to the NATRE results, the meridional lateral diffusivity component in GUTRE is smaller by about $20-30\%$. This finding agrees with eddy diffusivity parametrizations which shows that smaller lateral eddy diffusivities are to be expected in the tropical Atlantic ocean at some distance from the equator [e.g., *Eden and Greatbatch*, 2008].

The zonal diffusivity component in GUTRE is also about $20-30\%$ smaller compared to the NATRE's K_x estimate of 1500 m^2 s^{-1} derived from float analysis. Moreover, comparing the effective eddy diffusivity (K_e) and meridional diffusivity component (K_y) we estimate an effective zonal diffusivity component of 1000 m^2 s^{-1} $(400-2700)$. In conclusion, the zonal jets do not just deform the patch, but actively increase mixing in the zonal direction by increasing tracer gradients.

The zonal and meridional components of lateral diffusivity are computed in

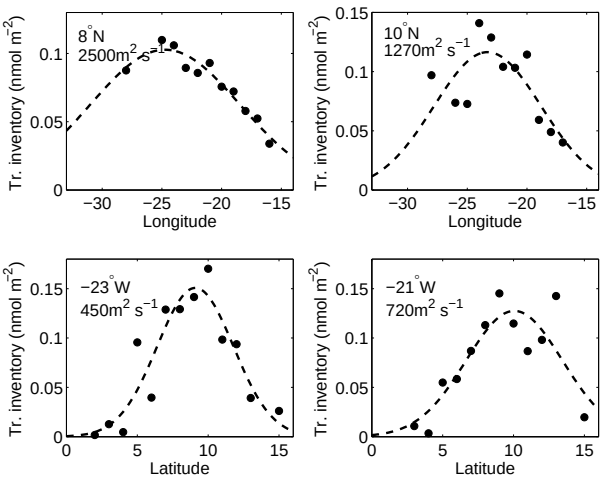

Figure 3.13: Gaussian distribution fit (dashed line) to four tracer patch transects along: 8°N, 10°N, 23°W, and 21°W (black dots), during the third GUTRE's survey.

this study. However, it is the meridional component (K_y), estimated across the mean zonal flow, which is associated with the turbulent lateral mixing by mesoscale eddies. More than twice larger zonal component (K_x) is a result of stretching of the patch by the mean flow. We employed the conceptual jet model (equation 3.1) to see how large jet velocities imply the observed K_x. With isotropic eddy mixing coefficient of $K = 500$ m^2 s^{-1}, we obtain the zonal velocities of about 0.015 m s^{-1} $(0.01 - 0.02)$. The estimated zonal jet velocities are slightly smaller than observed velocities. *Brandt et al.* [2010] reports zonal jet velocity estimates of about 0.03 m s^{-1} at about 400 m depth throughout the tropical Atlantic.

The partial sampling strategies were tested on the model data for a well developed tracer patch of 20 and 30 months old. We find that more than 70% of the tracer patch must be sampled to obtain diffusivity estimates with the uncertainty larger than 50%. The large region however can be covered with relatively sparse sampling grid of 2°. The results are more effected by contraction of the sampled field than by the reduction in the sampling frequency; in this study, only 1° and 2° sampling grid were compared.

3.7 Acknowledgments

We would like to thank all persons involved in the measurement of the tracer as well as the captains, crews and technicians on R/V *Maria S. Merian* and R/V *Meteor* and their home institutions for their support. Support for this work came from Deutsche Forschungsgemeinschaft as part of the Sonderforschungsbereich 754 "Climate-Biogeochemistry Interactions in the Tropical Ocean"

Chapter 4

Diapycnal oxygen supply to the tropical North Atlantic oxygen minimum zone

T. Fischer, D. Banyte, P. Brandt, M. Dengler, G. Krahmann, T. Tanhua, and M. Visbeck, submitted to *Biogeosciences Disc.*, October 2012

4.1 Abstract

The replenishment of consumed oxygen in the open ocean oxygen minimum zone (OMZ) off West Africa in the tropical North Atlantic Ocean is studied, with a focus on oxygen transport across density surfaces (diapycnal flux). The latter is obtained from a large observational set of oxygen profiles and diapycnal mixing data from years 2008 to 2010. Diapycnal mixing is inferred from different sources: a large scale tracer release experiment, microstructure profiles, and shipboard acoustic current measurements plus density profiles. The average diapycnal diffusivity in the study area is $1 \times 10^{-5}\,\mathrm{m^2\,s^{-1}}$. No significant vertical gradient of average diapycnal diffusivities exists in the depth interval from 150 to 500 m. The diapycnal flux is found to contribute substantially to the oxygen supply of the OMZ. Within the OMZ core, 1.5 μmol $\mathrm{kg^{-1}\ a^{-1}}$ of oxygen is sup-

plied via diapycnal mixing, contributing about a third of the total demand. The oxygen that is contributed via diapycnal mixing originates from oxygen that has been laterally supplied within the overlying Central Water layer by advective and eddy fluxes. Due to the existence of a separate shallow oxygen minimum at about 100 m depth throughout most of the study area, there is no direct net vertical oxygen flux from the surface layer of the study area into the Central Water layer. Thus all oxygen supply of the OMZ is associated with remote pathways.

4.2 Introduction

The open oceans host distinct permanent regions of low oxygen concentration (oxygen minimum zones OMZs), many of them situated at eastern boundaries in the tropics outside the equatorial belt. Tropical OMZs have common features in their coinciding with weak mean circulation and in their typical core depth range of 200 to 700 m, but their spatial extent and overall oxygen levels are diverse, with relatively high values in the Atlantic compared to the Indian and Pacific Oceans [*Karstensen et al.*, 2008; Paulmier and Ruiz-Pino, 2009]. OMZs are regions of diverse microbial and biochemical activity [Lam and Kuypers, 2011; *Wright et al.*, 2012], but pose a challenge or even lethal threat to certain marine animal species, with increasing numbers of threatened species the lower the oxygen level [Ekau et al., 2010; Prince et al., 2010; *Vaquer-Sunyer and Duarte*, 2008].

Being situated below the euphotic layer, the existence and position of oxygen minimum layers can be explained by a balance between oxygen loss by respiration of organic matter (consumption) and oxygen supply (excess of influx over outflux) that results from ventilation [*Wyrtki*, 1962]. Density coordinates subdivide oxygen flux into isopycnal and diapycnal components, i.e. along and across surfaces of constant density. In steady state there must be a balance between *consumption rate* and *divergence of isopycnal flux* and *divergence of diapycnal flux*. This balance is assumed to hold to first order despite some slow changes discussed below. The consumption rate may be seen as an external forcing exerted by sinking organic matter that originates in the surface layer, while parameters of ocean circulation like mean flow and eddy diffusivities set the system's reaction: the emanating shape of the oxygen concentration field and the size of associated

oxygen fluxes. In this view, feedbacks on organic matter supply by long-term changes in circulation parameters are ignored.

For the future in the wake of a warming ocean with increasing stratification, a net decline of the global ocean oxygen content is expected, and with it an expansion and intensification of OMZs is anticipated [*Keeling et al.*, 2010]. Consequences of oxygen decline for biogeochemical cycles, marine organisms and ecosystems are expected to be profound, particularly in regions that are already low in oxygen [Ekau et al., 2010; Gruber, 2011; *Wright et al.*, 2012]. Observations over the past decades indicate a recent decline in global subsurface ocean oxygen content [*Helm et al.*, 2011; *Stramma et al.*, 2010], with some exceptions particularly in the subtropical gyres [*Stramma et al.*, 2010], as well as a recent expansion of individual OMZs: outside the tropics [Bograd et al., 2008; *Whitney et al.*, 2007] and in the tropical Atlantic and Pacific Oceans [*Stramma et al.*, 2008]. Model simulations do not well reproduce the observed global oxygen distribution [*Duteil et al.*, 2011; Meissner et al., 2005; Najjar et al., 2007]; nonetheless they consistently predict global ocean oxygen loss under future climate scenarios [*Keeling et al.*, 2010]. What will happen to extent and intensity of individual OMZs in the future, is however less clear. Oxygen solubility, stratification, circulation, and organic export production are all processes that can be affected by climate change [*Bopp et al.*, 2002], and each of them, by their effect on ventilation and consumption, sensitively influences the extent and intensity of OMZs [Gruber, 2011]. Simulation efforts have resulted in projections of future global OMZ volume from expansion [*Matear and Hirst*, 2003; *Oschlies et al.*, 2008] to neutral [Gruber, 2011] to contraction [*Duteil et al.*, 2011]. The latter study found all three possible trends, with the sign of the predicted trend being sensitive to the amount of background diapycnal mixing. Supply path research is still rated a critical issue at the base of OMZ process understanding and the ability to predict OMZ fate [*Keeling et al.*, 2010]. Despite ongoing progress [e.g. *Banyte et al.*, 2012; *Brandt et al.*, 2010], uncertainties concerning size and relative importance of supply paths and processes remain.

Here we report on observed diapycnal mixing, and the corresponding diapycnal oxygen supply, in the tropical North Atlantic OMZ, i.e. an OMZ that has shown a noticeable oxygen decline during the last 5 decades [*Stramma et al.*,

2008, 2009]. In the framework of the German research programmes SFB754, SOPRAN, and NORTH ATLANTIC and the EU project EUROSITES, observation activities intensified in this region since 2008, with several cruises to the tropical North Atlantic OMZ. A large scale tracer release experiment (GUTRE, Guinea Upwelling Tracer Release Experiment) in the oxycline above the OMZ core provided an integrative view on diapycnal diffusivity [*Banyte et al.*, 2012]. An extensive grid of local measurements of diapycnal diffusivity performed by microstructure profiling and shipboard acoustic current profiling, together with oxygen profiles, provided an independent approach and statistical background information. Based on these data sources we constrain diapycnal mixing in the tropical North Atlantic OMZ, from which we are able to estimate the average diapycnal oxygen supply as a function of density. This in turn also provides some constraints to the isopycnal oxygen supply and OMZ supply paths.

4.3 Study site

4.3.1 Tropical North Atlantic oxygen minimum zone

The OMZ in the tropical North Atlantic Ocean (Fig. 4.1) approximately matches the Guinea Dome region [Siedler et al., 1992]. This coincidence is most likely caused by both, OMZ and Guinea Dome, being linked to the zone of weak circulation between North Equatorial Current (NEC at 20°N to 15°N) and North Equatorial Countercurrent/Undercurrent (NECC/NEUC at 5°N) [*Karstensen et al.*, 2008]. Vertical oxygen profiles in this region typically exhibit two oxygen minimum layers at core depths of about 100 m and 450 m (Fig. 4.4). The shallow minimum exists in about 80 to 90 % of our observations, with observations that lack a shallow minimum being scattered throughout the area, but becoming more frequent towards the southern edge of the OMZ. The oxygen minimum at about 450 m exists in all profiles in the region, and in the following we will only study this deeper, more voluminous and more intense oxygen minimum. Its core is at the interface between Antarctic Intermediate Water (AAIW) and the overlying Central Water [*Stramma et al.*, 2008b].

The vertical position of the core in the OMZ region does neither perfectly

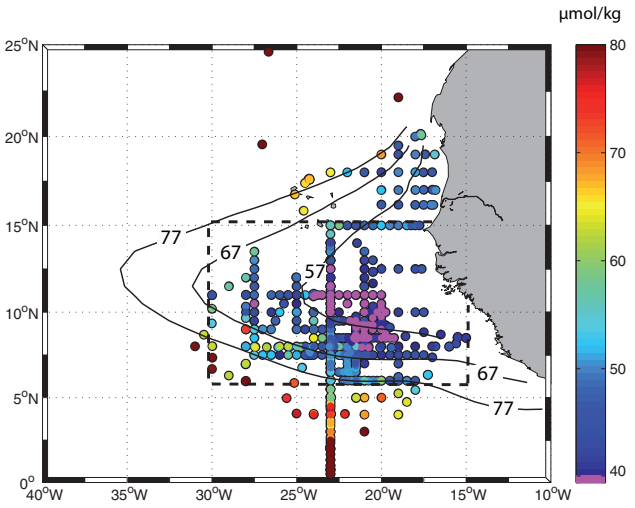

Figure 4.1: Oxygen concentrations (coloured dots) in the core of the deep oxygen minimum, which is situated at depths between 350 and 500 m. Oxygen data was collected during the time period 2008 through 2010 of the simultaneous tracer release experiment GUTRE, and stems from 7 ship cruises in total. Black labelled lines are oxygen core concentration isolines, the minimum concentrations derived from World Ocean Atlas WOA09 [Garcia et al., 2010] by vertical spline interpolation. The WOA 77 μmol kg^{-1} and 67 μmol kg^{-1} isolines roughly encircle the observed 60 μmol kg^{-1} and 50 μmol kg^{-1} core concentrations in 2008 to 2010, while the WOA 57 μmol kg^{-1} isoline does not well describe the 40 μmol kg^{-1} observations. The WOA 77 / 60 μmol kg^{-1} observations line is used here to define the extent of the OMZ. The dashed black line defines the analysis box (in depth interval 150 to 500 m) that comprises most of the available mixing data.

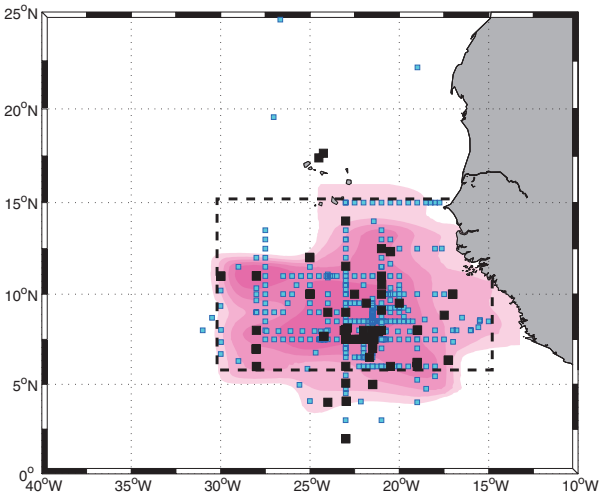

Figure 4.2: Minimum covered area of tracer patch after 30 months (magenta filled contour) as well as locations of microstructure measurements (black squares) and stations with shear data from 75 kHz vessel mounted ADCP (blue squares) during cruises in 2008 to 2010. The chosen analysis box is marked with a dashed black line.

follow isobaths nor isopycnals (Fig. 4.3). However it is better aligned to isopycnals: the standard deviation of the core vertical position in the OMZ is 60 m with respect to the mean core depth of 425 m, and 40 m with respect to the mean core isopycnal 27.03 kg m^{-3}. The position of the maximum oxygen gradient above the OMZ core (at about 300 m depth) will be called "deep oxycline" throughout this study, in order to distinguish it from the oxycline just below the mixed layer (Fig. 4.4).

We define horizontal OMZ extent by the 60 μmol kg^{-1} isoline of oxygen core concentration as observed between 2008 and 2010 (Fig. 4.1). The region encompassed by this isoline excludes better ventilated adjacent regimes, particularly those associated with the eastward flow of the NECC/NEUC in the South and with the subtropical gyre at Cape Verde front in the North. Meridional oxygen variations in the OMZ are found to be associated with a system of alternating zonal current bands, in which eastward currents coincide with higher oxygen concentration [*Brandt et al.*, 2010; *Stramma et al.*, 2008b].

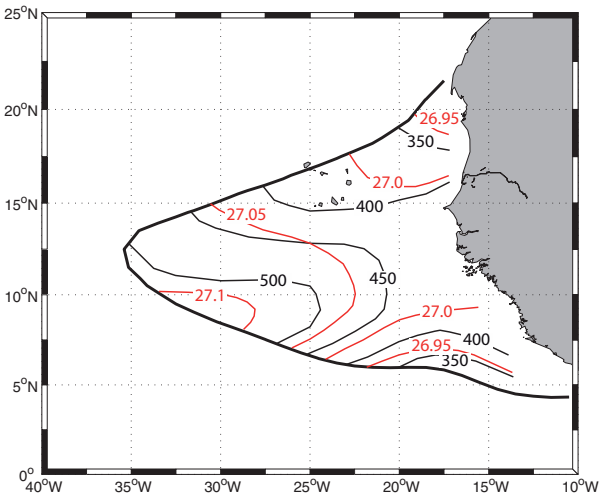

Figure 4.3: Vertical position of the deep oxygen minimum core in depth coordinates (black isolines, meters) and in potential density coordinates (red isolines, $\mathrm{kg\,m^{-3}}$). Isoline shapes are mostly derived from observations in 2008 to 2010. Where observational gaps were too large, isolines were completed by following the shapes of isolines based on World Ocean Atlas WOA09 [Garcia et al., 2010].

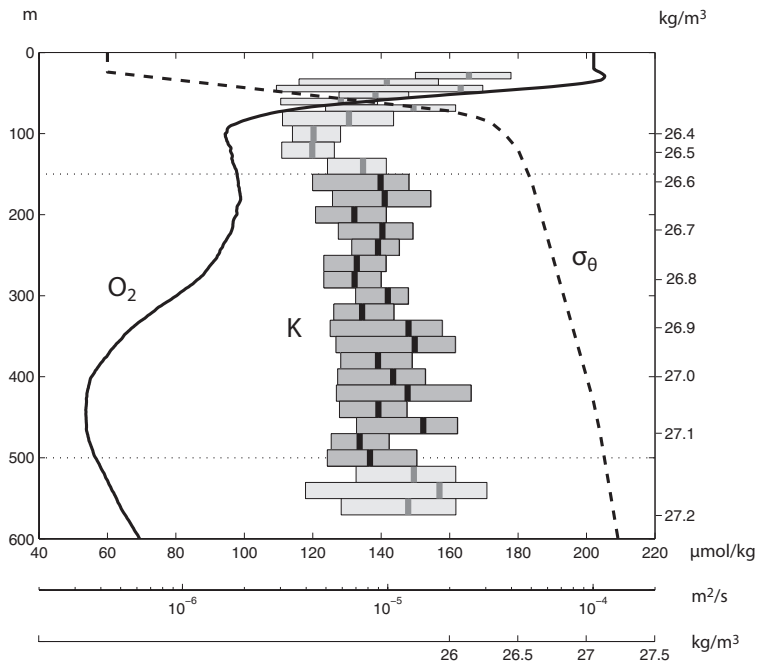

Figure 4.4: Profiles of oxygen concentration, diapycnal diffusivity K from microstructure measurements, and potential density, averaged across the entire chosen analysis box in the OMZ. Dotted lines mark the depth interval where diapycnal oxygen flux will be evaluated. This is the depth interval where the depth ranges covered by the different methods to infer K overlap.

4.3.2 Analysis box

For the analysis of diapycnal oxygen flux, a box is chosen from 6 to 15°N latitude, 30 to 15°W longitude, and 150 to 500 m depth. This analysis box covers large parts of the OMZ at its 60 μmol kg^{-1} isoline of core concentration, and it is centered at the location of the lowest observed core concentrations just below 40 μmol kg^{-1} (Fig. 4.1). Nevertheless it omits some parts of the OMZ: to the Northeast a region associated with upwelling, to the West a part where we expect core concentrations between 50 and 60 μmol kg^{-1}, and to the Southeast a part inside the shelf region and exclusive economic zones of some West African states. The chosen analysis box is the place where diapycnal mixing can be constrained best, because it was horizontally and vertically filled with tracer in the later phase of tracer release experiment GUTRE (after 20 and 30 months), and because most supplemental diapycnal mixing measurements that are suitable for our analysis were conducted during GUTRE surveys inside the analysis box (Fig. 4.2). The chosen depth interval extends from below the shallow oxygen minimum via the deep oxycline down to the core of the deep oxygen minimum (Fig. 4.4). Thus our analysis is confined to the upper half of the deep oxygen minimum layer, and diapycnal oxygen flux to the OMZ from the well oxygenated waters below the OMZ will not be considered in this study. Stratification (N^2) is near constant through the chosen depth interval for individual profiles but varies from 1×10^{-5} to 2×10^{-5} s^{-2} in the region with higher values found towards the Southeast [e.g. *Banyte et al.*, 2012].

4.4 Data and methods

4.4.1 Diapycnal diffusivity, diapycnal flux, diapycnal flux divergence and averaging

Diapycnal diffusivity K will be used to describe diapycnal mixing and to estimate the diapycnal flux of watermass properties. Due to the presence of turbulence in the ocean, diapycnal property fluxes are greatly enhanced compared to property fluxes in a non-turbulent fluid. Diapycnal diffusivities are thus strongly governed

by the turbulent flow characteristics of the oceanic region, albeit in principle K must be differentiated with respect to the watermass property in focus. As in our case the appropriate K_{oxygen} is inaccessible, approximate estimates had to be used. In this study, three different measurement methods are used to estimate K: from the diapycnal spreading of a tracer during GUTRE (Sect. 4.4.4), from direct measurements of the strength of turbulence using microstructure shear profiles (Sect. 4.4.5) and from vessel mounted Acoustic Doppler Current Profiler (vmADCP) data (Sect. 4.4.6). While GUTRE delivered an estimate of K_{tracer} (or K_{TRE}), with the tracer supposedly behaving similar to dissolved oxygen, microstructure and vmADCP measurements delivered an estimate of K_ρ, the diapycnal diffusivity of mass.

The diapycnal oxygen flux Φ can be estimated using Fick's first law of diffusion if simultaneous profiles of oxygen concentration (Sect. 4.4.3) and diapycnal diffusivity are available. The diapycnal flux is a down gradient flux perpendicular to density surfaces, driven by diapycnal diffusivity. The necessary diapycnal gradient of oxygen concentration to calculate Φ can be approximated by the vertical gradient of oxygen concentration, so that

$$\Phi = -\rho \, K_c \, \frac{\partial}{\partial z} c \tag{4.1}$$

with ρ water density in kg m^{-3}, K_c diapycnal diffusivity of oxygen in m^2 s^{-1}, c oxygen concentration in μmol kg^{-1} and resulting diapycnal flux Φ in μmol m^{-2} s^{-1}.

When regarding the oxygen budget in a volume enclosed by two isopycnal surfaces, the diapycnal influx across the first isopycnal surface does not need to be of the same magnitude as the diapycnal outflux across the second isopycnal surface. The difference of the two diapycnal fluxes is described by diapycnal flux divergence $\nabla\Phi$, which can be approximated by the vertical derivative of Φ, $\partial\Phi/\partial z$. $\nabla\Phi$ is in μmol kg^{-1} a^{-1}. A positive value means that the density layer loses oxygen via a diapycnal flux imbalance. In order to quantify net oxygen supply of the density layer caused by diapycnal processes, it is necessary to observe $-\nabla\Phi$.

Ultimately, the goal is to determine averaged profiles of diapycnal diffusivities, fluxes and flux divergences for the entire OMZ. Thus averaging along isopycnal

surfaces is a necessary processing step which will be denoted by brackets, e.g. as in $\langle K \rangle$. Unless otherwise specified the brackets mean arithmetic averaging after objective mapping on isopycnal surfaces. For the objective mapping, the decorrelation scale was determined to 0.5°. Additionally, averaging in diapycnal direction will occur and will be denoted by an overbar, e.g. as in $\overline{K}$, so that a total average for the entire analysis box in this example would be $\langle \overline{K} \rangle$.

4.4.2 Data overview

The data was collected during 4 cruises in November 2008 (R.V. Merian MSM10/1), November and December 2009 (R.V. Meteor M80/1 and M80/2) and October 2010 (R.V. Meteor M83/1), during the tracer surveys for GUTRE. Oxygen was measured using a Conductivity-Temperature-Depth profiler (CTD) with added Clark-type oxygen sensors (CTD-O_2). For most of the oxygen profiles, simultaneous estimates of diapycnal diffusivity K_ρ from microstructure profiles or vmADCP were available. In total, 400 complete profiles consisting of CTD-O_2 and diapycnal diffusivity were collected in the analysis box (Fig. 4.2). The tracer surveys delivered one additional independent space-time-averaged estimate of diapycnal diffusivity for the entire region for 2008 through 2010. Another 3 cruises in February, March, and April 2008 (R.V. L'Atalante GEOMAR/3 and GEOMAR/4, and R.V. Merian MSM08/1) delivered 110 additional oxygen profiles without simultaneous K estimates. These oxygen measurements helped in outlining the OMZ (Fig. 4.1), but did not enter the oxygen flux calculation.

4.4.3 Oxygen and CTD data calibration

Each ship station that is considered here comprises a CTD-O_2 profile, down to at least the deep oxygen minimum core at about 400 to 500 m. On the four cruises evaluated here (MSM10/1, M80/1, M80/2, and M83/1) similar CTD/rosette systems were used, consisting of a Seabird 911plus CTD equipped with dual Seabird temperature, conductivity, and oxygen sensors. During each of the cruises several hundred water samples were collected to calibrate the conductivity and oxygen sensors using a Guildline Autosal 8400B salinometer and a Winkler titration stand. The deviations between the in situ conductivity measured by the Seabird

CTD and the high accuracy on-board water sample measurements using salinometers were used to derive a correction to the CTD's conductivity linear in pressure, temperature, and CTD conductivity itself. After applying the corrections, the resulting absolute accuracy of the CTD salinity values was estimated to 0.005, 0.002, 0.002, and 0.003 for the cruises MSM10/1, M80/1, M80/2, and M83/1, respectively. Laboratory calibration suggests the accuracy of the temperature and pressure measurements to be better than 0.002 K and 1.5 dbar, respectively. Similar to conductivity, the deviations between the CTD and the on-board Winkler titrations were used to derive a correction to the CTD's oxygen measurements. The chosen correction was linear in pressure, temperature, and oxygen, and we estimate the absolute accuracy of the CTD's oxygen measurements to be better than 3, 1, 1, and 1 μmol kg^{-1} for the four cruises, respectively.

While these estimates of the CTD data's absolute uncertainty and their only slowly varying corrections are useful for comparisons with other observations, for our analysis of vertical oxygen gradients an estimate of the oxygen sensor noise and precision is more relevant. We found that the oxygen sensors had a typical instrument noise of less than 0.2 μmol kg^{-1}. The estimates of vertical oxygen gradients used here are based on 1 dbar averages of the CTD oxygen measurements, which were originally recorded at 24 Hz. This results in a noise-induced uncertainty of the vertical oxygen gradient of less than 0.03 μmol kg^{-1} m^{-1} when evaluated at 2 dbar intervals.

4.4.4 K estimated from GUTRE

The deliberate Guinea Upwelling Tracer Release Experiment (GUTRE) was performed in the deep oxycline in the tropical North Atlantic OMZ, in order to obtain a time- and space-integrated estimate of diapycnal diffusivity at the OMZ's upper limit. 92 kg of the halocarbonic compound SF_5CF_3 [*Ho et al.*, 2008] were released in April 2008 at 8°N 23°W at the isopycnal surface σ_θ = 26.88 kg m^{-3}. The expanding tracer patch was sampled during 3 survey campaigns (MSM10/1, M80 and M83/1) 7, 20 and 30 months after injection. After 20 and 30 months, the tracer essentially covered the analysis box horizontally and vertically. From the increase of the vertical extent of the isopycnally integrated tracer

distribution, the time-space-averaged diapycnal diffusivity was estimated to be $\langle\overline{K}\rangle_{TRE} = (1.19 \pm 0.18) \times 10^{-5}$ m^2 s^{-1} [*Banyte et al.*, 2012]. The uncertainty on 95 % confidence level is based on bootstrapping and measurement errors. During all 3 surveys the mean tracer concentration profile showed no significant skew.

4.4.5 K estimated from microstructure data

As an independent method from GUTRE, diapycnal diffusivities were also estimated using microscale shear recordings from a loosely-tethered microstructure profiler. During the tracer survey cruises, the microstructure profiler MSS90D (termed MSS in the following) of Sea and Sun Technology, Trappenkamp, Germany, was used immediately after certain CTD casts. Usually 3 profiles in a series down to 500 m at 0.5 m s^{-1} sink velocity were collected at these ship stations. In total, MSS data could be obtained on 45 ship stations in the analysis box.

On the way to estimate diapycnal diffusivities from MSS, the signal from 2 to 4 airfoil shear sensors at the profiler head was converted to profiles of microscale vertical shear. Then the dissipation rate ϵ of turbulent kinetic energy could be estimated from the power spectrum of microscale vertical shear, by using a vertical wavenumber range free of instrument vibrational noise and by assuming local isotropy [Oakey, 1982; Stips and Prandke, 2000]. The diapycnal diffusivity of mass, K_ρ, was inferred from the Osborn parametrization $K_\rho = \Gamma\, \epsilon\, N^{-2}$ [*Osborn*, 1980] with Γ the dimensionless dissipation ratio that is related to mixing efficiency. Γ was set 0.2, because simulation data by Shih et al. [2005] suggest this value to be appropriate for weak to moderate turbulence, what is what was found in the analysis box. The value 0.2 is further supported by findings of St. Laurent and Schmitt [1999], who report Γ between 0.15 and 0.25 in turbulence dominated regimes with weak mean shear, conditions that were also met in the analysis box. For the analyses of this study, vertical averages of ϵ and N^2 for the depth interval 150 m through 500 m were used to infer a single average $\overline{K}_{\rho,MSS}$ per ship station via the Osborn parametrization. The uncertainty of $\overline{K}_{\rho,MSS}$ was estimated from quantifiable errors (essentially from sensor uncertainties and spectral estimation) to be 60 % on a 95 % confidence level.

4.4.6 K estimated from vmADCP

The possibility to obtain additional estimates of K_ρ from current velocity profiles via vmADCP substantially enhanced the number of "complete" station data comprising CTD plus oxygen plus K, which could be used to infer diapycnal oxygen flux; the number rising from 45 to 400 inside the analysis box (Fig. 4.2). The method is based on the observation that finescale vertical shear with vertical wavelengths of order 10 m to some 100 m and dissipation rate ϵ of turbulent kinetic energy can be related [Gargett, 1976; Gregg, 1989]. It had been used before with Lowered ADCP data [*Kunze et al.*, 2006; Polzin et al., 2002]. The main processing strategy for the application to vmADCP data during ship stations was: (1) generate velocity profiles with noise low enough, so that vertical shear signals can still be detected which are on the order of the open ocean background level; (2) obtain spectra of vertical shear of horizontal velocity, in finescale vertical wavenumber range; (3) obtain dissipation rate ϵ from shear power spectral level Φ_S by a parametrization (see appendix), which uses MSS measurements for calibration; (4) obtain K_ρ from ϵ and CTD derived stratification by the Osborn parametrization as in Sect. 4.4.5.

Minutiae of processing were: During 3 survey cruises MSM 10/1, M80/2 and M83/1, an RDI Ocean Surveyor 75 kHz vmADCP continuously recorded currents down to 600 m depth at 8 m vertical bin size. The broadband mode that we used, a high ping frequency (36 min^{-1}), usually calm sea conditions, and a final two-dimensional filtering step of velocity fields in depth-time-space, resulted in one-minute-average velocity data of 1 $\mathrm{cm\,s}^{-1}$ precision at 95 % level (for technical details refer to *Fischer* [2011]). From the one-minute-averaged and filtered velocity profiles, spectra of vertical shear were calculated for 150 to 533 m depth and corrected following Polzin et al. [2002] for variance losses caused by ADCP binning, tilting and ping averaging. The resulting one-minute shear power spectra were usable in the wavenumber band from 1/128 cpm to 1/38.4 cpm. Power spectra were averaged over the duration of a ship station, and served to estimate a single value of shear power spectral level Φ_S for that ship station and the entire depth interval 150 to 500 m. Φ_S led to $\overline{\epsilon}_{ADCP}$ after using the parametrization Eq. (4.6), and to $\overline{K_\rho}_{,ADCP}$ after using the Osborn parametrization. The uncertainty

of $\overline{\epsilon}_{ADCP}$ was estimated to be 60 % on 95 % confidence level, resulting from measurement noise, discrete spectrum estimation, and error progression through the parametrization Eq. (4.6).

4.4.7 Implications of K derived from different sources

Apart from physical differences of the derived diapycnal diffusivities, the 3 applied methods delivered K estimates, which also differ in the grade to which they represent spatial and temporal averaged quantities. The immediate result of the MSS measurements were vertical profiles of K_ρ for each ship station at about 0.5 m depth resolution, the result of the vmADCP processing was a single vertical average $\overline{K_\rho}$ for each ship station, and the TRE delivered essentially one time-space-average $\langle\overline{K}\rangle$ for the entire analysis box during 2008 to 2010. For the further processing of K – i.e. to deliver estimates of $\langle\overline{K}\rangle$, a profile of diapycnal oxygen flux, $\langle\Phi\rangle$, and a profile of diapycnal flux divergence – we assume that K can be treated as vertically homogeneous through the used depth interval 150 to 500 m for timescales larger than several days. This assumption gets supported by the MSS derived average K_ρ profile $\langle K_\rho\rangle_{MSS}$, which shows no significant gradient in 150 to 500 m (Fig. 4.4), as well as by GUTRE tracer profiles, which showed no significant deviation from a Gaussian [*Banyte et al.*, 2012]. Vertical homogeneity in 150 to 500 m is also suggested by the majority of individual density profiles in the analysis box, which show a near constant stratification. The assumption of vertically homogeneous K implies that (1) vertical averaging of K for MSS data is equivalent to averaging of longer timeseries, which we lack; (2) $\overline{K}$ defines the level of the assumed constant K profile at each ship station; in that sense K and $\overline{K}$ are equivalent for the process of isopycnal averaging (e.g. to estimate $\langle\Phi\rangle$).

Another property of our dataset is the statistical independence of K_ρ resp. $\overline{K_\rho}$ from MSS/ADCP and the corresponding oxygen gradient, as shown in Fig. 4.5 for all depths between 150 and 500 m. The independence is expressed in the equivalence of $\langle K_\rho \times grad\, c\rangle$ and $\langle K_\rho\rangle \times \langle grad\, c\rangle$. This also means that $\langle\Phi\rangle$ may be calculated as $\langle\langle K\rangle \times grad\, c\rangle$, i.e. K may also be treated as if it was laterally homogeneous (but this time on the long timescale of the TRE duration). The estimates of this effective long-term largescale K will be denoted $\langle\overline{K}\rangle_{TRE}$

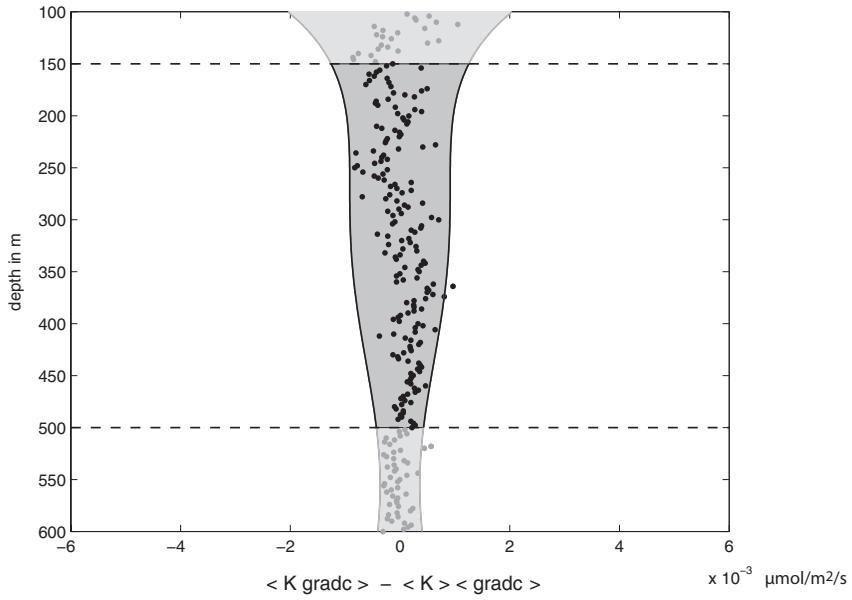

Figure 4.5: Difference between the horizontal average of local diapycnal fluxes, and the product of horizontally averaged diapycnal diffusivity and horizontally averaged oxygen gradient, as a function of depth. The difference is found to be smaller than the 95 % confidence interval of $\langle K \cdot grad\, c \rangle$ (grey shading) for most depth layers. Dashed lines mark the analysis depth interval. The evaluation outside the analysis depth interval assumes K values at each ship station to be constant through the 100 m to 600 m depth range.

and $\langle\overline{K}\rangle_{MSS/ADCP}$ (MSS and ADCP combined, because the ADCP method was calibrated with MSS measurements).

4.5 Results and discussion

4.5.1 Diapycnal diffusivities

Estimates of diapycnal diffusivity were derived from the deliberate tracer release experiment GUTRE and from MSS/ADCP methods. The different estimates are evaluated by comparing the box average $\langle\overline{K}\rangle_{MSS/ADCP}$, calculated from microstructure measurements enhanced by vessel mounted ADCP, to the GUTRE value $\langle\overline{K}\rangle_{TRE}$. From MSS/ADCP we find an average diapycnal diffusivity of mass of $\langle\overline{K}\rangle_{MSS/ADCP} = 0.95 \times 10^{-5}\,\mathrm{m^2\,s^{-1}}$ with 95 % confidence interval [0.91 1.08]$\times 10^{-5}\,\mathrm{m^2\ s^{-1}}$ which has been estimated by a bootstrap method. *Banyte et al.* [2012] report a tracer diapycnal diffusivity of $\langle\overline{K}\rangle_{TRE} = 1.19 \times 10^{-5}\,\mathrm{m^2\,s^{-1}}$ with 95 % confidence interval [1.01 1.37]$\times 10^{-5}\,\mathrm{m^2\,s^{-1}}$ (Sect. 4.4.4). The difference between $\langle\overline{K}\rangle_{MSS/ADCP}$ and $\langle\overline{K}\rangle_{TRE}$ is moderate but significant: the probability to find this or a greater difference is 2 %, when two independent measurement methods are applied to estimate the value of $\langle\overline{K}\rangle$, and these methods have uncertainties according to the two reported confidence intervals.

There are several possible physical reasons for the diffusivity of a passive tracer, K_{TRE}, and the diffusivity of mass, K_ρ, to be different. One fundamental difference between the two is related to double diffusive processes: in salt finger regimes, salt and other passive tracers are transported more effectively than buoyancy; thus tracer diffusivities are enhanced. In our case this would mean to get a low-biased value of $\langle\overline{K}\rangle$ when using $\langle\overline{K}\rangle_{MSS/ADCP}$ for an estimate. St. Laurent and Schmitt [1999] report for another TRE site in the subtropical North Atlantic (NATRE), that double diffusion can make up for the difference that was found here between K_{TRE} and K_ρ. In order to estimate the relative importance of double diffusion, double diffusive enhancement of K was estimated from CTD profiles following St. Laurent and Schmitt [1999], with salt-finger thermal diffusivity $k_\theta^{(f)}$ assumed to be $6 \times 10^{-6}\,\mathrm{m^2\,s^{-1}}$. Applying this method to the depth interval 150 to 500 m suggests that double diffusive enhancement could add $0.1 \times 10^{-5}\,\mathrm{m^2\,s^{-1}}$

to $\langle\overline{K}\rangle_{MSS/ADCP}$ in the upper part of the Central Water, then be negligible for $\pm$50 m above and below the deep oxycline, while sharply rising just at the OMZ core depth to $0.3\times10^{-5}\,\mathrm{m^2\,s^{-1}}$ and further rising to $0.5\times10^{-5}\,\mathrm{m^2\,s^{-1}}$ below the core depth. For the entire 150 to 500 m depth interval this would result in an effective enhancement of $\langle\overline{K}\rangle_{MSS/ADCP}$ by roughly $0.1\times10^{-5}\,\mathrm{m^2\,s^{-1}}$, which in turn would make the difference between $\langle\overline{K}\rangle_{MSS/ADCP}$ and $\langle\overline{K}\rangle_{TRE}$ insignificant.

Besides this possible explanation for the difference between $\langle\overline{K}\rangle_{MSS/ADCP}$ and $\langle\overline{K}\rangle_{TRE}$, the two methods to estimate $\langle\overline{K}\rangle$ further contain systematic biases of unknown amount that could not be accounted for in the methods uncertainties. Concerning the TRE this applies to (1) the fact that for each tracer survey about half of the tracer patch could not be sampled and thus the deduced diapycnal extent of the patch might be biased; (2) $\langle\overline{K}\rangle_{TRE}$ being biased towards the early TRE period in which the tracer did only cover a fraction of the entire region. Concerning MSS measurements this applies to (1) underlying assumptions in the train of calculating turbulent diffusivity (e.g. the value of dissipation ratio Γ in the Osborn parametrization), (2) seasonal bias, (3) some gaps in the sampling of the analysis box. We interpret the similarity of the two estimated $\langle\overline{K}\rangle$ values as indication that the unaccounted systematic biases are small. But we cannot decide which of the two $\langle\overline{K}\rangle$ estimates is better, and thus leave the two for further calculations, in their difference representing the additional uncertainty in estimated diapycnal diffusivity that results from applying different methods.

The average diapycnal diffusivity that we find for the analysis box is distinctly higher than expected for this latitude range. An internal wave field with background intensity and with stratification in the found range of 1 to 2 $\times10^{-5}\,\mathrm{s^{-2}}$ should exhibit a $\langle\overline{K}\rangle$ of only some $10^{-6}\,\mathrm{m^2\,s^{-1}}$ following the parametrization in *Gregg et al.* [2003]. The discrepancy in $\langle\overline{K}\rangle$ is coincident with rough bottom topography in the analysis box and an intensified internal wave field [*Fischer*, 2011].

4.5.2 Diapycnal oxygen flux in the analysis box

Diapycnal diffusivities and oxygen gradients are combined to an average profile of diapycnal oxygen flux as function of density for the analysis box (Fig. 4.6).

Here the depth interval 150 to 500 m, for which we know K, roughly corresponds to the potential density range of $\sigma_\theta = 26.55$ kg m^{-3} to 27.1 kg m^{-3} in a near linear relation. Main features of the diapycnal oxygen flux profile are two layers of zero flux which correspond to positions of zero oxygen gradient in the mean oxygen profile, and a maximum oxygen downflux at the deep oxycline inbetween. The lower layer of zero diapycnal flux at $\sigma_\theta = 27.03$ kg m^{-3} is in the OMZ core depth and means that the OMZ can be separated into an upper and a lower half and that oxygen supply can be assessed separately for these OMZ halves. The depth interval of our data only allows calculations for the upper half of the OMZ. The upper layer of zero diapycnal flux at $\sigma_\theta = 26.63$ kg m^{-3} is situated in the overlying Central Water that carries a relatively high oxygen concentration, and it exists because of the widespread presence of a shallow oxygen minimum above. The existence of the layer of zero diapycnal flux means that in the analysis box the oxygen supply to the OMZ has no direct link to the surface ocean. The diapycnal downflux of oxygen at the deep oxycline ($\sigma_\theta = 26.85$ kg m^{-3}) is about $(5 \pm 1) \times 10^{-3}$ μmol m^{-2} s^{-1}. This may be interpreted as a diapycnal supply of about 1.5 μmol kg^{-1} a^{-1} from the overlying Central Water to the upper half of the OMZ, or as a redistribution of oxygen inside the water body that is limited by the two layers of zero diapycnal flux.

4.5.3 Sensitivity to data processing

The processing of the diapycnal flux profile was performed in various ways, with respect to the measurement method for K and the sequence order of processing steps, in order to explore the sensitivity of the result to processing decisions. The reference method to obtain diapycnal flux, as defined by us, was calculating local flux profiles from local $K_{MSS/ADCP}$ and local oxygen gradients in small (2 m) intervals, then averaging local flux profiles isopycnally to an aggregated flux profile and finally smoothing vertically (in a symbolic notation: $\langle K_{MSS/ADCP} \times grad\, c \rangle_{smoothed}$). Other ways of processing were tested against this reference. Swapping isopycnal averaging and flux calculation ($[\langle K_{MSS/ADCP} \rangle \times \langle grad\, c \rangle]_{smoothed}$) has, as expected, little effect since $K_{MSS/ADCP}$ and $grad\, c$ are statistically independent in our dataset (Sect. 4.4.7). Thus using $\langle \overline{K} \rangle_{TRE}$ to

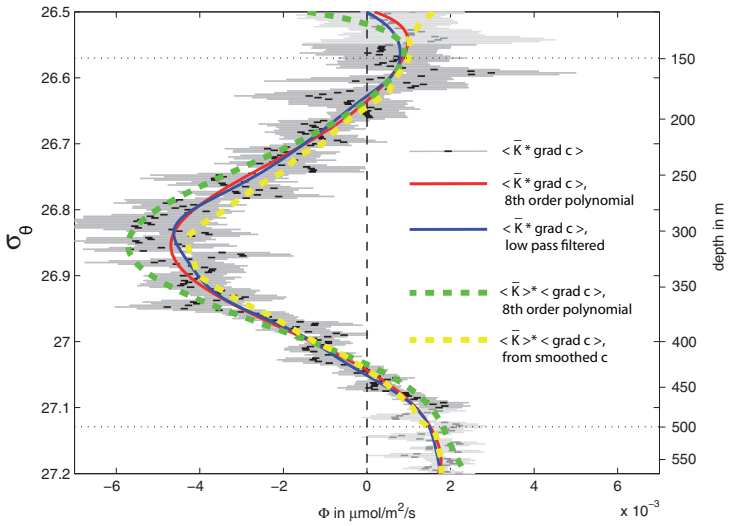

Figure 4.6: Diapycnal oxygen flux in density coordinates as determined by different methods. The given smoothed curves assume that fluctuations of smaller vertical scales are an artefact of imperfect sampling. Black dots with grey shading: local oxygen gradients over 2 m combined with local K from MSS/ADCP measurements to local diapycnal flux, then averaged horizontally along isopycnals. Red line: Corresponding fitted 8th order polynomial. Blue line: corresponding low pass filtered flux profile. Dashed green line: 8th order polynomial on flux profile that was derived from horizontally averaged oxygen gradient and integral K value from the Tracer Release Experiment. Dashed yellow line: flux profile derived from vertically smoothed oxygen gradient profiles that have been horizontally averaged along isopycnals before combined with the integral K value from the Tracer Release Experiment. Dotted black lines approximately mark the analysis depth interval 150 to 500 m for which K estimates exist. The deep OMZ core is located at about $\sigma_\theta = 27.03$ kg m^{-3} or 425 m. The deep oxycline is located at about $\sigma_\theta = 26.85$ $kg\,\mathrm{m}^{-3}$ or 310 m.

calculate diapycnal flux by $[\langle\overline{K}\rangle_{TRE} \times \langle grad\, c\rangle]_{smoothed}$ essentially differs from $\langle\overline{K}_{MSS/ADCP} \times grad\, c\rangle_{smoothed}$ by the factor $\langle\overline{K}\rangle_{TRE}\langle\overline{K}\rangle_{MSS/ADCP}$. The attempt to reduce measurement error by smoothing local oxygen gradient profiles before both calculating flux and averaging isopycnally (i.e. $\langle\overline{K}\rangle_{TRE} \times \langle grad\, c_{smoothed}\rangle$ vs. $[\langle\overline{K}\rangle_{TRE} \times \langle grad\, c\rangle]_{smoothed}$) not only reduces noise but also systematically reduces the gradient and thus the estimated diapycnal flux (Fig. 4.6).

4.5.4 Sensitivity to coordinate choice

It may be worthwhile asking what the diapycnal flux across other surfaces than isopycnals is, even though then diapycnal flux is no longer perpendicular to these surfaces and there also exists an isopycnal flux component across these surfaces. Obvious coordinate choices other than isopycnal could be isobaths or surfaces that are linked to features of the oxygen field. Such a different choice primarily changes the vertical shift with which profiles of oxygen gradient get aggregated in the process of averaging laterally (i.e. along the surfaces appropriate for the chosen coordinate system). We examined two cases: (1) diapycnal flux across isobaths, (2) diapycnal flux across a surface that connects the gradient maxima of the deep oxycline. For case (1) the resulting diapycnal flux profile is similar in shape to the diapycnal flux profile of Fig. 4.6, but flux values are reduced by about 30 %; the downward diapycnal flux at the deep oxycline is about 3×10^{-3} to $4 \times 10^{-3}\,\mu\mathrm{mol\,m^{-2}\,s^{-1}}$. A coordinate choice like in case (2) leads to the maximum possible estimate of downward diapycnal flux at the deep oxycline; here the resulting flux is about 6×10^{-3} to $7 \times 10^{-3}\,\mu\mathrm{mol\,m^{-2}\,s^{-1}}$.

4.5.5 Diapycnal flux divergence and OMZ oxygen budget

Looking at the oxygen budget for individual isopycnal layers of the OMZ (Fig. 4.7) allows further insight into oxygen supply than just quantifying the oxygen flux across particular surfaces. The contribution to oxygen supply by diapycnal processes, i.e. diapycnal surplus in units of moles oxygen per volume and time, is described by a negative diapycnal flux divergence (Sect. 4.4.1). Maximum diapycnal contribution happens at about the OMZ core, zero diapycnal contribution at the maximum oxygen gradients above and below the OMZ core. The overlying

Central Water loses oxygen to the OMZ below by diapycnal mixing, but also upwards towards the shallow oxygen minimum layer. Concerning the other terms of the oxygen budget – consumption rate and isopycnal supply –, consumption rate estimates may be taken from literature, while isopycnal supply is the difference of consumption rate and diapycnal supply, assuming steady state. Reported consumption rate profiles are diverse and uncertain [*Keeling et al.*, 2010], but their principal shape is typically assumed to be exponential with depth [*Karstensen et al.*, 2008; *Martin et al.*, 1987]. *Karstensen et al.* [2008] estimated an exponential consumption rate profile specific for the Atlantic and Pacific OMZ regions from apparent oxygen utilization and estimated water ages. This profile is used here: consumption rate in $\mu\mathrm{mol\,kg^{-1}\,a^{-1}}$ is $-0.5 + 12 \cdot exp(-0.0021 \cdot z)$ with z depth in meters. The uncertainty of the consumption rate was estimated to be 40 % (95 % confidence level) from the scatter of *Karstensen et al.* [2008]'s reported oxygen utilization rates. Thus the resulting uncertainty of the deduced profile of isopycnal supply is large, but the main pattern seems clear: the profile of isopycnal oxygen supply resembles a step function, with large isopycnal supply in the Central water layer above the deep oxycline, and little isopycnal supply in the OMZ layer below the deep oxycline. The contribution of diapycnal supply to the OMZ core may be estimated to be about a third of the demand, with large uncertainty.

4.6 Conclusions

The tracer release experiment and the MSS/ADCP measurements complement each other and delivered consistent estimates of diapycnal diffusivity K. For the 400 stations in the analysis box, which covers large parts of the OMZ in the depth interval 150 to 500 m in the thermocline, we found statistical independence of local diapycnal diffusivity and local vertical oxygen gradient. This feature allows to estimate average diapycnal flux in the analysis box from the regional average of diapycnal diffusivity and the regional average of the oxygen gradient profile, given that these averages are representative for the analysis box. If such an independence of K and the concentration gradients is also valid for other regions and substances, regional diapycnal fluxes may be estimated from datasets which

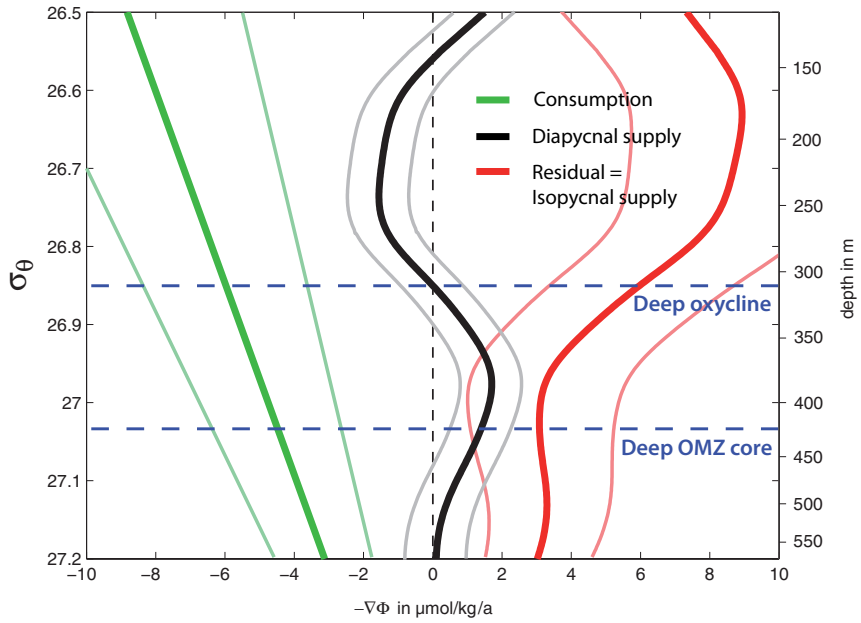

Figure 4.7: Terms of the oxygen budget (diapycnal supply + isopycnal supply + consumption rate = 0) as a function of density. Diapycnal supply = negative diapycnal flux divergence (black) was determined in this study (here we chose a smooth line compromising between divergences of the polynomial and the low pass smoothed fluxes from TRE and MSS, as of Fig. 4.6). Oxygen consumption rate (green) was estimated according to *Karstensen et al.* [2008]; the exponential decrease in depth coordinates turns out to be hardly discernible from linear when transformed to isopycnal coordinates in the depth interval 150 to 500 m. The residual that closes the budget must account for isopycnal supply (red). Uncertainties are 95 % confidence limits.

comprise non-simultaneous measurements.

The estimated oxygen budget suggests that diapycnal mixing contributes substantially to oxygen supply of the tropical North Atlantic OMZ. In the layers of the analysis box associated with the OMZ core, about a third of total oxygen supply is diapycnal. Such a rating of importance however depends on perspective and the chosen boundaries, and potentially is subject to some adjustments when better estimates of isopycnal supply and consumption rate become available. It might be equally valid to assign the oxygen supply entirely to lateral processes: if choosing a layer bounded by isopycnal surfaces $\sigma_\theta = 26.63$ kg m^{-3} and 27.03 kg m^{-3} (each with zero diapycnal flux), the supply of the water column inbetween must be completely isopycnal and the role of diapycnal mixing would reduce to just generating internal oxygen redistribution. But even with this latter perspective, the role of diapycnal mixing is substantial. If diapycnal mixing was less intense than observed, the oxygen distribution in the analysis box would certainly be another: given the other parameters kept constant, the vertical oxygen gradient would most likely become sharper and the oxygen concentration in the OMZ core would become lower. In sum we conclude that the higher than expected level of diapycnal mixing in the study region (Sect. 4.5.1) plays a substantial role in shaping the oxygen concentration field and supposedly also in causing relatively high levels of oxygen in the core of the tropical North Atlantic OMZ compared to other OMZs.

The importance of diapycnal flux to supply the lower half of the deep OMZ with oxygen from AAIW can only hardly be evaluated with the present data, which mostly did not reach the necessary depths. But there are indications that the diapycnal influence is substantial as well. Although gradient and curvature of oxygen concentration are known to be lower in the lower half than in the upper half of the OMZ, turbulent diffusivity below the OMZ core is found equal or larger than above (Fig. 4.4), and is enhanced by double diffusion here (adds 50 % if following the method of St. Laurent and Schmitt [1999]). The resulting total diapycnal oxygen flux from below might even reach similar values as from above, while the oxygen consumption rate to be balanced is lower than above. A scheduled TRE starting by the end of 2012 aims at estimating isopycnal and diapycnal diffusivity around the OMZ core and will elucidate the relative impor-

tance of supply processes; together with ADCP and microstructure profiles down to 1000 m.

Local profiles of consumption rate are still difficult to obtain [e.g. *Keeling et al.*, 2010], but are important for closing the budget. Nevertheless, the general tendency of consumption rate to diminish with depth seems described well enough by the fitted exponential of *Karstensen et al.* [2008], and moderate deviations from that profile would not change the main features of the deduced isopycnal oxygen supply profile as of (Fig. 4.7). In fact, some deviation from an exponential shape seems even probable, e.g. caused by active organic matter transport during diel vertical migration of zooplankton [Angel, 1985; Steinberg et al., 2002]. The local importance of the latter process for the OMZ region is unknown, but acoustic evidence of strong migrant activity suggests enhanced oxygen consumption at about 300 m and diminished oxygen consumption at about 200 m depth. This is a shape not uncommon in reported consumption profiles ([*Feely et al.*, 2004] for the Pacific), but on their reported level the effect would just be shifting the jump in the isopycnal supply profile of Fig. 4.7 slightly downwards, while not changing the profile's principal shape.

Concerning the shape of the deduced isopycnal supply profile, the sharp decline at the depth of the deep oxycline (Fig. 4.7) could principally originate from diffusive and/or advective supply. However we do not expect lateral diffusivities having a jump at the deep oxycline, nor expect a vertical jump of proper sign in the second derivative of isopycnal oxygen distribution (supported by WOA09 climatological data [Garcia et al., 2010]). This makes eddy processes an improbable reason for the sharp decline. Further we do not expect mean current velocities having a jump in magnitude or direction at the depth of the deep oxycline. Thus it is suggested that the main contribution to the shape of isopycnal oxygen supply is due to mean advection of water with oxygen profiles of greater than average vertical oxygen gradient when entering the OMZ region and with oxygen profiles of weaker than average vertical oxygen gradient when leaving the OMZ region (and depth-dependent consumption plus downward redistribution of oxygen happening inside the region). The western boundary circulation characterized by strong vertical shear is a likely candidate for generating sharp vertical oxygen gradients that could be transported within eastward current bands into the OMZ.

4.7 Acknowledgements

This study benefitted from cruises, infrastructure and financial support by the German Federal Ministry of Education and Research through the co-operative projects SOPRAN and NORTH ATLANTIC, and by German Science Foundations Sonderforschungsbereich SFB754 "Climate Biogeochemistry Interactions in the Tropical Ocean". We acknowledge the support of the European Commission (FP7-EuroSITES grant agreement No. 202955). The support of captains, crews and scientific crews of Meteor cruise 80, Meteor cruise 83/1, Merian cruise 08/1, Merian cruise 10/1, L'Atalante cruises GEOMAR/3 and GEOMAR/4 is highly appreciated. We thank Johannes Karstensen for fruitful discussions.

The service charges for this open access publication
have been covered by a Research Centre of the
Helmholtz Association.

4.8 Appdx. Dissipation rate from vmADCP data

There is a widely known parametrization of dissipation rate ϵ for the open ocean [*Gregg et al.*, 2003; *Polzin et al.*, 1995], which is based on the concept of breaking internal waves causing turbulence, dissipation and mixing. Important needed parameters to use this parametrization are finescale vertical shear and finescale vertical strain; "finescale" in this context comprises vertical wavenumbers of order 10 to order 100 m. In this study, we had access to vertical shear via vmADCP data (Sect. 4.4.6), but for strain we lacked simultaneous data of satisfying quality. For remedy we fitted another parametrization with fewer parameters, using own data from the tropical North Atlantic Ocean, plus using data from midlatitudes, which were reported by *Polzin et al.* [1995] and formed the base of their parametrization.

Here two variables were used which have commonly been identified to influence mixing intensity in the open ocean: (1) the intensity of velocity vertical shear in the vertical wavelength band of tens to hundreds of meters, as providing the forcing, (2) the characteristic slope of internal waves, which influences their probability to break and cause turbulence, dissipation and mixing. The predic-

tors Ψ_1 and Ψ_2 we defined for the parametrization were derived from these two variables, having been inspired by the Garrett-Munk (GM) internal wave model [*Garrett and Munk*, 1975; Munk, 1981]. Ψ_1 was chosen proportional to the power spectral level Φ_S of vertical finescale shear as

$$\Psi_1 = N^2 \cdot G, \tag{4.2}$$

with N buoyancy frequency and G a nondimensional number describing the power spectral level of shear, Φ_S, in relation to its GM background level $\Phi_{S,GM} = const. \cdot N^2$. G was estimated from vmADCP data by

$$G = \frac{\Phi_S^{k_{min}...k_{max}}}{\Phi_{S,GM}^{k_{min}...k_{max}}}, \tag{4.3}$$

and both $\Phi_S^{k_{min}...k_{max}}$ and $\Phi_{S,GM}^{k_{min}...k_{max}}$ were calculated in the vertical wavenumber range $k_{min} = 1/128\,\mathrm{cpm}$ to $k_{max} = 1/38.4\,\mathrm{cpm}$ by weighted averaging as $\Sigma((9-i)/8 \cdot \Phi_{S,i})/\Sigma((9-i)/8)$ for the appropriate $\Phi_{S,i}$ at wavenumbers $k_i = (2+i)/384\,\mathrm{cpm}$. This way to estimate G is specific to the used vmADCP configuration and the used depth interval for the analysis of 150 to 500 m. But G is not expected to be sensitive to the particular choice of k_i in the finescale range. Ψ_2 was chosen as

$$\Psi_2 = \frac{f}{N}, \tag{4.4}$$

with f the Coriolis parameter, because the characteristic slope of the internal wave field approximately is a power of $f \cdot N^{-1}$ when assuming the GM model.

In order to fit a regression model we took the existing 45 stations with simultaneous microstructure profiles, CTD profile and vmADCP measurements, plus data from the High Resolution Profiler collected at several midlatitude locations as reported by *Polzin et al.* [1995]. Predictor Ψ_1 relied on vmADCP data for G and CTD data for N^2, predictor Ψ_2 needed latitude and CTD data for N, and predictand ϵ was provided by microstructure data. In order to avoid a skewed distribution in parameter space we did linear regression in logarithmic space, i.e. the regression model was $\log \epsilon = a_0 + a_1 \cdot \log \Psi_1 + a_2 \cdot \log \Psi_2$. The best model fit

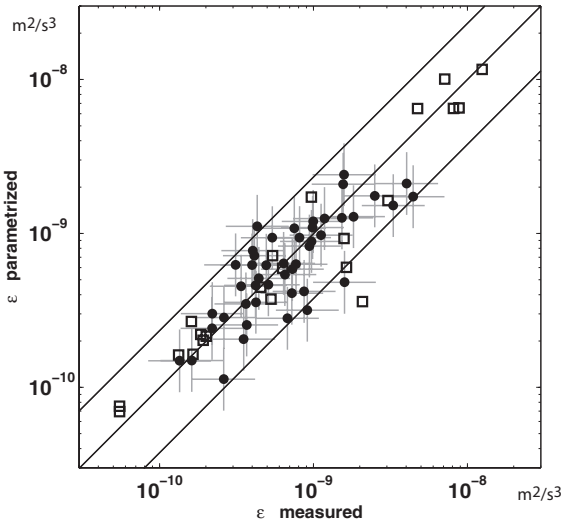

Figure 4.8: Predicted versus measured turbulent dissipation rates. Predictions by parametrization $\epsilon = 1/100 \cdot f^{5/9} \cdot N^{19/9} \cdot G^{4/3}$ that resulted from a two-parameter-fit in $\Psi_1 = N^2 \cdot G$ (vertical shear power) and $\Psi_2 = f \cdot N^{-1}$ (internal wave slope). Measurements by microstructure profiler MSS90D in the region of the tropical North Atlantic OMZ (black dots) and values reported by *Polzin et al.* [1995] performed with the High Resolution Profiler in different midlatitude locations (squares). 95 % of predictions lie within a factor 2.5 from measured values.

(Fig. 4.8) can be written as

$$\epsilon = \frac{1}{100} \cdot \Psi_1^{4/3} \cdot \Psi_2^{5/9} \tag{4.5}$$

with multiple correlation $R^2 = 0.80$. This relation translates to

$$\epsilon = \frac{1}{100} \cdot f^{5/9} \cdot N^{19/9} \cdot G^{4/3}. \tag{4.6}$$

Chapter 5

Outlook

The main motivation behind the research described in the three manuscripts of this thesis was an interest in the oxygen supply pathways into the oxygen minimum zone of the tropical North Atlantic Ocean. We have investigated the supply pathways by estimating diapycnal and along isopycnal mixing from the tracer release experiment.

The Guinea Upwelling Tracer Release Experiment was designed primarily to obtain the diapycnal mixing coefficient, integrated over time and space. The method allowed to achieve the estimate of the diapycnal mixing coefficient with the uncertainty of up to 15%. The result was later used to obtain an accurate estimate of the diapycnal oxygen supply component through the vertical boundary and into the oxygen minimum zone. The resulting uncertainty of the diapycnal oxygen supply component, averaged over a region of $6° - 15°$N, $15° - 30°$W, was obtained of up to 20%.

The comparison of diapycnal oxygen supply to lateral oxygen supply into the oxygen minimum zone is non-trivial. We applied the conceptual oxygen consumption function over depth [*Karstensen et al.*, 2008] to constrain the lateral oxygen supply component from the estimated diapycnal component. In this case, the diapycnal oxygen supply was found to be significant: about two times smaller than the lateral supply. It must be noted, however, that depth related oxygen consumption was derived from the whole Atlantic data set to which a non-linear minimization fit to a logarithmic function was applied. There could be local differences found in the eastern tropical ocean. Direct estimates of oxygen con-

sumption with depth in the tropical Atlantic are, however, not yet available.

In addition, the lateral oxygen supply could be estimated directly by applying the lateral mixing coefficients computed from the tracer release experiment and the lateral oxygen gradients. In this case, the lateral oxygen influx can not be directly computed at the center of the oxygen minimum zone, because the tracer was released at a depth of about 100 m above the absolute oxygen minimum - at a position coinciding with the largest oxygen gradient. However, direct application of the along isopycnal mixing coefficient estimated from the GUTRE could serve as a quality test for the currently used oxygen consumption function of *Karstensen et al.* [2008]. Overall, the lateral diffusivities are shown to significantly decrease with depth [*Ferrari and Polzin*, 2005]. Thus, the lateral diffusivities at the center of the oxygen minimum could be over 30% smaller than the values found in GUTRE. The tracer release experiment performed at the core of the oxygen minimum zone could be a good complementary study to quantify the oxygen balance in the oxygen minimum zone.

However, in general, tracer release experiments are primarily used to obtain the diapycnal, instead of lateral, mixing coefficient. The main reason for this is that the average over tens of vertical tracer profiles converge to a Gaussian shape in open ocean thermocline experiments, such as NATRE or GUTRE. The use of tracer release experiments to estimate lateral mixing coefficients is much more challenging. One reason is that the lateral spread of the tracer is analyzed from the spatial distribution of vertical tracer inventories, which requires good vertical sampling of the tracer - same as with diapycnal mixing estimates. The other reason is that more than a hundred profiles are required to cover the largest part of the tracer patch when trying to achieve estimate of greater than 50% precision. In this thesis, I show that models can be used to improve the confidence of the estimates, especially when a non-regular sampling grid is chosen for the field experiment. In order to decrease the uncertainties of the estimates, however, it is important to check how the results change when using different ocean models. We expect, however, that the uncertainties of the estimates can only be reduced by enhancing the sampling frequency as well as the sampling region.

Despite the challenge of estimating lateral mixing coefficients from tracer release experiments, the method has the same advantages as are valid for the di-

apycnal mixing coefficients: the value is an average over a long time period. Furthermore, it allows the parametrization of the effect of zonal jets. This is because the estimates are an average over a large spatial scale, i.e. the region occupied by the tracer patch. Overall, the zonal jets defined by the mean of the variable velocity field not only advect the tracer, but also enhance mixing by increasing lateral tracer gradients. The combined effect of advection and mixing induced by the zonal jets might be difficult to assess, but the integrative manner of the tracer experiment is one of the best methods to parametrize their effect.

Finally, I would like to shortly address an application of isopycnal coordinates and the associated thickness weighted averaging operator introduced in the diapycnal mixing calculations. The tracer spread across isopycnals was shown to be affected by the stratification, or the thickness of the density layers. The thickness weighted tracer concentration was defined as a mass of tracer in the isopycnic volume, i.e. the volume between isopycnals of thickness z_ρ and a unit area. The quantity assures that with varying isopycnal thickness from one region to another, the volumetric tracer concentration stays the same. The GUTRE has shown that the tracer concentration multiplied by the thickness of the isopycnals varied the least between the regions of stratification. Similar considerations apply to the oxygen concentrations. The large number of oxygen profiles gathered during the three tracer sampling surveys allows to check the correlation between oxygen concentrations and the thickness of density layers. The difference between oxygen concentrations and thickness-weighted concentrations averaged along isopycnals is expected to be greatest at the shallower levels where both oxygen and 'thickness' variability was found to be the largest. It is not expected that thickness-weighted averaging would significantly change the results of diapycnal oxygen supply estimates. However, the differences can appear in the regional estimates, as was shown for the diapycnal mixing coefficient in two coordinate systems.

Bibliography

Angel, M. V. (1985), Vertical migrations in the oceanic realm: possible causes and probable effects, in: Migration: Mechanisms and Adaptive Significance, *Contributions in Marine Science*, *27*, edited by: Rankin, M. A., et al., Marine Science Institute, Austin, Texas, 45–70 96

Banyte, D., T. Tanhua, M. Visbeck, D. W.R. Wallace, J. Karstensen, G. Krahmann, A. Achneider, L. Stramma, and M. Dengler (2012), Diapycnal diffusivity at the upper boundary of the tropical North Atlantic oxygen minimum zone, *J. Geophys. Res.*, *117*, C09016 45, 52, 74, 75, 80, 84, 86, 88

Barnier, B., L. Siefridt, and P. Marchesiello (1995), Thermal forcing for a global ocean circulation model using a three year climatology of ECMWF analysis, *J. Mar. Syst.*, *6(4)*, 363–380

Brandt, P., and C. Eden (2005), Annual cycle and interannual variability of the middepth tropical Atlantic Ocean, *Deep Sea Res. Part I*, *52*, 199–219 51

Brandt, P., V. Hormann, B. Bourles, J. Fischer, F. A. Schott, L. Stramma, and M. Dengler (2008), Oxygen tongues and zonal currents in the equatorial Atlantic, *J. Geophys. Res.*, *113*, C04012 7, 16

Brandt, P., V. Hormann, A. Körtzinger, M. Visbeck, G. Krahmann, and L. Stramma (2010), Changes in the ventilation of the oxygen minimum zone of the tropical North Atlantic, *J. Phys. Oceanogr. 40*, 1784–1801 4, 13, 69, 74, 77

Bryden, H. L. and R. A. Heath (1985), Energetic eddies at the northern edge of the Antarctic Circumpolar Current, *Progress in Oceanogr. 14*, 65–87 3

Bograd, S. J., Castro, C. G., Di Lorenzo, E., Palacios, D. M., Bailey, H., Gilly, W., and Chavez, F. P. (2008), Oxygen declines and the shoaling of the hypoxic boundary in the California Current, *Geophys. Res. Lett.*, *35*, L12607 74

Bopp, L., C. Le Quere, M. Heimann, A. C. Manning, and P. Monfray (2002), Climate-induced oxygen fluxes: implications for the contemporary carbon budget, *Glob. Biogeochem. Cycles*, *16*, 1022 9, 74

Boyer, T., and S. Levitus (1997), Objective analysis of temperature and salinity for the world ocean of a 1/4 degree grid, technical report, *NOAA*, Washington, D.C.

Bullister, J. L., and R. F. Weiss (1988), Determination of CCl_3F and CCl_2F_2 in seawater and air, *Deep-Sea Res. 35*, 839–853 19

Bullister, J. L., and D. P. Wisegarver (2008), The shipboard analysis of trace levels of sulfur hexafluoride, chlorofluorocarbon-11 and chlorofluorocarbon-12 in seawater, *Deep-Sea Res. I 55*, 1063–1074 19

Bullister, J. L., D. P. Wisegarver, and R. E. Sonnerup (2006), Sulfur hexafluoride as a transient tracer in the North Pacific Ocean, *Geophys. Res. Lett. 33*, L18603 16

Curry, R., B. Dickson, and I. Yashayaev (2003), A change in the freshwater balance of the Atlantic Ocean over the past four decades, *Nature 426*, 826–829 18

Dengg, J., C. Böning, U. Ernst, R. Redler, and A. Beckmann (1999), Effects of an improved model representation of overflow water on the subpolar North Atlantic, *Int. WOCE Newsl.*, *37*, 10–15 51

Davis, R. (1991), Observing the general circulation with floats, *Deep-Sea Res.*, *38A*, 531–571 3

de Szoeke, R. A., and A. F. Bennett (1993), Microstructure fluxes across density surfaces, *J. Phys. Oceanogr. 23*, 2254–2264 23, 24, 40

Duteil, O. and A. Oschlies (2011), Sensitivity of simulated extent and future evolution of marine suboxia to mixing intensity, *Geophys. Res. Lett.*, *38*, L06607 9, 74

Eckart, C. (1948), An analysis of the stirring and mixing processes in incompressible fluids, , *J. Mar. Res.*, *7*, 265–275 2, 45

Ekau, W., Auel, H., Pörtner, H.-O., and Gilbert, D. (2010), Impacts of hypoxia on the structure and processes in pelagic communities (zooplankton, macroinvertebrates and fish), *Biogeosciences 7*, 1669–1699 73, 74

England, M. H. (1995), The age of water and ventilation timescales in a global ocean model, *J. Phys. Oceanogr.*, *25*, 2756–2777 6

Eden, C., and C. Böning (2002), Sources of eddy kinetic energy in the Labrador Sea, *J. Phys. Oceanogr.*, *32*, 3346–3363 51

Eden, C., and R. J. Greatbatch (2008), Towards a mesoscale eddy closure, *Ocean Modell.*, *20*, 223–239 47, 68

Eden, C., R. J. Greatbatch, and J. Willebrand (2007), A diagnosis of thickness fluxes in an eddy-resolving model, *J. Phys. Oceanogr.*, *37*, 727–742 47

Feely, R. A., C. L. Sabine, R. Schlitzer, J. L. Bullister, S. Mecking, and D. Greeley (2004), Oxygen utilization and organic carbon remineralization in the upper water column of the Pacific Ocean, *J. Oceanogr.*, *60*, 45–52 6, 96

Ferrari, R., and K. L. Polzin (2005), Finescale structure of the T-S relation in the eastern North Atlantic, *J. Phys. Oceanogr.*, *35*, 1437–1454 101

Fischer, T. (2007), Simulating a tracer release experiment in the tropical east Atlantic ocean, Diploma thesis, Christian-Albrechts Univ., Kiel, Germany 52

Fischer, T. (2011), Diapycnal diffusivity and transport of matter in the open ocean estimated from underway acoustic profiling and microstructure profiling, PhD thesis, Dep. of Math. and Natural Sc., Christian-Albrechts Univ., Kiel, Germany. 42, 85, 89

Fischer, T., D. Banyte, P. Brandt, M. Dengler, G. Krahmann, T. Tanhua, and M. Visbeck (2012 submitted), Diapycnal oxygen supply to the tropical North Atlantic oxygen minimum zone, *Biogeosciences Disc.* 46

Garcia, H. E., Locarnini, R. A., Boyer, T. P., Antonov, J. I., Baranova, O. K., Zweng, M. M., and Johnson, D. R. (2010), World Ocean Atlas 2009 Volume 3 (Dissolved Oxygen, Apparent Oxygen Utilization, and Oxygen Saturation), NOAA Atlas NESDIS 70, edited by: Levitus, S., US Government Printing Office, Washington, DC, 344 pp. 76, 78, 96

Gargett, A. E. (1976), An investigation of the occurrence of oceanic turbulence with respect to finestructure,*J. Phys. Oceanogr. 6*, 139–156 85

Garrett, C. (1983), On the initial streakiness of a dispersing tracer in two- and three-dimensional turbulence, *Dyn. of Atmosph. and Oceans*, *7*, 265–277 45, 47

Garrett, C., and W. Munk (1975), Space-Time Scales of Internal Waves: A Progress Report, *J. Geophys. Res. 80*, 291–297 98

Glover, D. M., W. J. Jenkins, and S. C. Doney (2011), *Modeling methods for marine science*, Cambridge University Press 25

Gnanadesikan, A., J. L. Russell, and F. Zeng (2007), How does ocean ventilation change under global warming?, *Ocean Sci.*, *3*, 43–53 9

Gregg, M. C. (1987), Diapycnal mixing in the thermocline, *J. Geophys. Res. 92*, 5249–5289 14

Gregg, M. C. (1989), Scaling turbulent dissipation in the thermocline, *J. Geophys. Res. 94*, 9686–9698 85

Gregg, M. C., C. S. Cox, and P. W. Hacker (1973), Vertical microstructure measurements in the central North Pacific, *J. Phys. Oceanogr. 3*, 458–469 3, 13

Gregg, M. C., T. B. Sanford, and D. P. Winkel (2003), Reduced mixing from the breaking of internal waves in equatorial waters, *Nature 422*, 513–515 3, 13, 15, 41, 89, 97

Gruber, N. (2011), Warming up, turning sour, losing breath: ocean biogeochemistry under global change, Philos. *T. Roy. Soc. A 369*, 1980–1996 74

Helm, K. P., N. L. Bindoff, and J. A. Church (2011), Observed decreases in oxygen content of the global ocean, *Geophys. Res. Lett.*, *38*, L23602 7, 74

Henyey, F. S., J. Wright, and S. M. Flatte (1986), Energy and Action Flow Through the Internal Wave Field: an Eikonal Approach, *J. Geophys. Res. 91*, 8487–8495 15, 41

Ho, D. T., J. R. Ledwell, and W. M. Smethie Jr. (2008), Use of SF_5CF_3 for ocean tracer release experiments, *Geophys. Res. Lett. 35*, L04602 16, 83

Holtermann, P. L., L. Umlauf, T. Tanhua, O. Schmale, G. Rehder, and J. J. Waniek (2012), The Baltic Sea Tracer Release Experiment: 1. Mixing rates, *J. Geophys. Res. 117*, C01021 16

Hüttl, S., and C. Böning (2006), Mechanisms of decadal variability in the shallow subtropicaltropical circulation of the Atlantic Ocean: A model study, *J. Geophys. Res.*, *111*, C07011 51

Hüttl-Kabus, S., and C. Böning (2008), Pathways and variability of the offequatorial undercurrents in the Atlantic Ocean, *J. Geophys. Res.*, *113*, C10018 51

Jenkins, W. J. (1987), ^{3}H and ^{3}He in the Beta-Triangleobservations of gyre ventilation and oxygen utilization rates, *J. Phys. Oceanogr.*, *17*, 763–783 6, 46

Joos, F., G. K. Plattner, T. F. Stocker, A. Körtzinger, and D. W. R. Wallace (2003), Trends in marine dissolved oxygen: implications for ocean circulation changes and carbon budget, *Eos, Trans. Am. Geophys. Union*, *84*, 197

Kalnay, E., et al. (1996), The NCEP/NCAR 40 year reanalysis project, *Bull. Am. Meteorol. Soc.*, *77(3)*, 437-471

Karstensen, J., L. Stramma, and M. Visbeck (2008), Oxygen minimum zones in the eastern tropical Atlantic and Pacific oceans, *Prog. Oceanogr.*, *77*, 331–350 5, 6, 46, 73, 75, 93, 94, 96, 100, 101

Keeling, R. F., A. Körtzinger, and N. Gruber (2010), Ocean deoxygenation in a warming world, *Annu. Rev. Marine Sci.*, *2*, 199–229 5, 7, 9, 74, 93, 96

Kirchner, K., M. Rhein, C. Martens, C. Böning, and S. Hüttl (2008), Observed and modeled meridional overturning circulation related flow into the Caribbean, *J. Geophys. Res.*, *113*, C03028 51

Kirchner, K., M. Rhein, S. Hüttl, and C. Böning (2009), On the spreading of South Atlantic Water into the Northern Hemisphere, *J. Geophys. Res.*, *114*, C05019 51

Klocker, A., R. Ferrari, J. LaCasce, and S. Merrifield (2012), Reconciling float-based and tracer-based estimates of eddy diffusivities, *J. Mar. Res.*, in press. 4, 47, 49

Kunze, E., and T. B. Sanford (1996), Abyssal mixing: Where it isn't., *J. Phys. Oceanogr. 26*, 2286–2296 14, 42

Kunze, E., E. Firing, J. M. Hummon, T. K. Chereskin, and A. M. Thurnherr (2006), Global abyssal mixing inferred from lowered ADCP shear and CTD strain profiles, *J. Phys. Oceanogr. 36*, 1553–1576 3, 13, 14, 15, 41, 85

Lam, P. and Kuypers, M. M. M. (2011), Microbial nitrogen cycling processes in oxygen minimum zones, *Annu. Rev. Mar. Sci. 3*, 317–345 73

LaCasce, R. (2008), Statistics from Lagrangian observations, *Progress in Oceanogr.*, *77*, 1–29 3

Law, C. S., and A. J. Watson (2001), Determination of Persian Gulf Water transport and oxygen utilisation rates using SF_6 as a novel transient tracer, *Geophys. Res. Lett. 28*, 815–818 16

Law,C. S., A. J. Watson, and M. I. Liddicoat (1994), Automated vacuum analysis of sulfur hexafluoride in seawater: derivation of the atmospheric trend (1970-1993) and potential as a transient tracer, *Mar. Chem. 48*, 57–69 20

Ledwell, J. R., and A. Bratkovich (1995), A tracer study of mixing in the Santa Cruz Basin, *J. Geophys. Res. 100*, 20,681–20,704 35

Ledwell, J. R., and A. J. Watson (1991), The Santa Monica Basin tracer experiment: A study of diapycnal and isopycnal mixing, *J. Geophys. Res. 96*, 8695–8718 17, 35

Ledwell, J. R., A. J. Watson, and C. S. Law (1993), Evidence for slow mixing across the pycnocline from an open-ocean tracer-release experiment, *Nature 364*, 701–703 14

Ledwell, J. R., A. J. Watson, and C. S. Law (1998), Mixing of a tracer in the pycnocline, *J. Geophys. Res. 103*, 21499–21529 4, 14, 19, 21, 22, 28, 36, 41, 45, 46, 47, 48, 52

Ledwell, J. R., E. T. Montgomery, K. L. Polzin, L. C. St. Laurent, R. W. Schmitt, and J. M., Toole (2000), Evidence for enhanced mixing over rough topography in the abyssal ocean, *Nature 403*, 179–182 14

Ledwell, J. R., L. C. St. Laurent, J. B. Girton, and J. M. Toole (2011), Diapycnal mixing in the Antarctic circumpolar current, *J. Phys. Oceanogr. 41*, 241–246 17, 41

Levitus, S., and T. P. Boyer (Eds.) (1994), World Ocean Atlas 1994, vol. 4, Temperature, NOAA Atlas NESDIS, vol. 4, *NOAA, Silver Spring*, 129pp.

Luyten, J. R., J. Pedlosky, and H. Stommel (1983), The ventilated thermocline, *J. Phys. Oceanogr. 13*, 292–309 6, 13, 46

Meissner, K. J., Galbraith, E. D., and Völker, C. (2005) Denitrification under glacial and interglacial conditions: A physical approach, *Paleoceanography*, *20*, PA3001 74

Marshall, J. E., J. H. Shuckburgh, and C. Hill (2006), Estimates and implications of surface eddy diffusivity in the Southern Ocean derived from tracer transport, *J. Phys. Oceanogr.*, *36*, 1806–1821 4, 49

Martin, J. H., G. A. Knauer, D. M. Karl, and W. W. Broenkow (1987), Vertexcarbon cycling in the northeast Pacific, *Deep-Sea Res. I*, *34*, 267–285 6, 93

Matear, R. J. and A. C. Hirst (2003), Long-term changes in dissolved oxygen concentrations in the ocean caused by protracted global warming, *Glob. Biogeochem. Cycles*, *17*, 1125 8, 9, 74

McCreary, J. P. Jr. and P. Lu (1994), Interaction between the subtropical and equatorial ocean circulations: the subtropical cell, *J. Phys. Oceanogr.*, *24*, 466–497 6

Munk, W. H. (1981), Internal waves and small-scale processes, in: Evolution of Physical Oceanography; Scientific Surveys in Honor of Henry Stommel, edited by: Warren, B. A. and Wunsch, C., MIT press, Cambridge and London, 264–291 98

Munk, W., and C. Wunsch (1998), Abyssal recipes II: Energetics of tidal and wind mixing, *Deep-Sea. Res. I 45*, 1977–2010 14

Najjar, R. G., et al., (2007), Impact of circulation on export production, dissolved organic matter, and dissolved oxygen in the ocean: results from phase II of the Ocean Carbon-cycle Model Intercomparison Project (OCMIP-2), *Global Biogeochem. Cy.*, *21*, GB3007 74

Nakamura, N. (1996), Two-dimensional mixing, edge formation, and permeability diagnosed in area coordinates, *J. Atmosph. Sc.*, *53*, 1524–1537. 49

Naqvi, S. W. A., H. W. Bange, L. Farias, P. M. S. Monteiro, M. I. Scranton, and J. Zhang (2010), Marine hypoxia/anoxia as a source of CH_4 and N_2O, *Biogeosciences*, *7*, 2159–2190 8

Oakey, N. S. (1982), Determination of the rate of dissipation of turbulent energy from simultaneous temperature and velocity shear microstructure measurements, *J. Phys. Oceanogr.*, *12*, 256–271 84

Ono, T., T. Midorikawa, Y. W. Watanabe, K. Tadokoro, and T. Saino (2001), Temporal increases of phosphate and apparent oxygen utilization in the subsurface waters of western subarctic Pacific from 1968 to 1998, *Geophys. Res. Lett.*, *28*, 3285–3288 7

Osborn, T. R. (1980), Estimates of the local rate of vertical diffusion from dissipation measurements, *J. Phys. Oceanogr. 10*, 83–89 3, 13, 84

Osborn, T. R., and C. S. Cox (1972), Oceanic fine structure, *Geophys. Fluid Dyn. 3*, 321–345 24

Oschlies, A., K. G. Schultz, U. Riebesell, and A. Schmittner (2008), Simulated 21st centurys increase in oceanic suboxia by CO2 -enhanced biotic carbon export, *Glob. Biogeochem. Cycles*, *22*, GB4008 9, 74

Pacanowski, R., (1995), MOM2 documentation, users guide and reference manual, technical report, 329 pp., Geophys. Fluid Dyn. Lab., Princeton, N. J. 51

Paulmier, A. and Ruiz-Pino, D. (2009), Oxygen minimum zones (OMZs) in the modern ocean, *Prog. Oceanogr.*, *80*, 113–128 73

Polzin, K. L., J. M. Toole, and R. W. Schmitt (1995), Finescale parameterizations of turbulent dissipation, *J. Phys. Oceanogr. 25*, 306–328 3, 14, 97, 98, 99

Polzin, K. L., J. M. Toole, J. R. Ledwell, and R. W. Schmitt (1997), Spatial variability of turbulent mixing in the abyssal ocean, *Science 276*, 93–96 14, 41, 42

Polzin, K., Kunze, E., Hummon, J., and Firing, E. (2002), The finescale response of lowered ADCP velocity profiles, *J. Atmos. Ocean. Tech.*, *19*, 205–224 85

Prince, E. D. and C. P. Goodyear (2006), Hypoxia-based habitat compression of tropical pelagic fishes, *Fish. Oceanogr.*, *15*, 451–464 8

Prince, E. D., Luo, J., Goodyear, C. P., Hoolihan, J. P., Snodgrass, D., Orbesen, E. S., Serafy, J. E., Ortiz, M., and Schirripa, M. J. (2010), Ocean scale hypoxia-based habitat compression of atlantic istiophorid billfishes, *Fish. Oceanogr.*, *19*, 448–462 73

Rye, C. D., M. J. Messias, J. R. Ledwell, A. J. Watson, A. Brousseau, and B. A. King (2012), Diapycnal diffusivities from a tracer release experiment in the deep sea, integrated over 13 years, *Geophys. Res. Lett. 39*, L04603 41

Schafstall, J., M. Dengler, P. Brandt, and H. Bange (2010), Tidal-induced mixing and diapycnal nutrient fluxes in the Mauritanian upwelling region, *J. Geophys. Res. 115*, C10014 3, 13

Shih, L. H., Koseff, J. R., Ivey, G. N., and Ferziger, J. H. (2005), Parameterization of turbulent fluxes and scales using homogeneous sheared stably stratified turbulence simulations, *J. Fluid Mech.*, *525*, 193–214 84

Schmitt, R. W. (1994), Double Diffusion in Oceanography, *Ann. Rev. Fluid Mech.*, *26*, 255-285 3

Schmittner, A., A. Oschlies, H. D. Matthews, and E. D. Galbraith (2008), Future changes in climate, ocean circulation, ecosystems, and biogeochemical cycling simulated for a business-as-usual CO2 emission scenario until year 4000 AD, *Glob. Biogeochem. Cycles*, *22*, GB1013 8

Schneider, A., T. Tanhua, A. Körtzinger, and D. W.R. Wallace (2012), An evaluation of tracer fields and anthropogenic carbon in the equatorial and the tropical North Atlantic, *Deep Sea Res. Part I 67*, 85–97 46

Siedler, G., Zangenberg, N., and Onken, R. (1992) Seasonal changes in the tropical Atlantic circulation: observation and simulation of the guinea dome, *J. Geophys. Res.*, *97*, 703–715 75

Steinberg, D. K., Goldthwait, S. A., and Hansell, D. A. (2002), Zooplankton vertical migration and the active transport of dissolved organic and inorganic nitrogen in the Sargasso Sea, *Deep-Sea Res. I*, *49*, 1445–1461 96

Stips, A. and Prandke, H. (2000), Recommended Algorithm for Dissipation Rate calculation within PROVESS, European Commission, JRC, Space Applications Institute, Technical Note No. 1.00.116, available at: `www.pol.ac.uk/provess/bodc/doc/dissi_algo.pdf`, last access: 10 October 2012 84

St. Laurent, L. and Schmitt, R. W. (1999), The contribution of salt fingers to vertical mixing in the North Atlantic Tracer Release Experiment, *J. Phys. Oceanogr.*, *29*, 1404–1424 84, 88, 95

St. Laurent, L. C., and A. M. Thurnherr (2007), Intense mixing of lower thermocline water on the crest of the Mid-Atlantic Ridge, *Nature 448*, 680–683 14, 42

Stramma, L., S. Hüttl, and J. Schafstall (2005), Water masses and currents in the upper tropical Northeast Atlantic off northwest Africa, *J. Geophys. Res. 110*, C12006 6, 16, 46, 52

Stramma, L., G. C. Johnson, J. Sprintall, and V. Mohrholz (2008), Expanding oxygen-minimum zones in the tropical oceans, *Science*, *320*, 655–658 5, 46, 74

Stramma, L., P. Brandt, J. Schafstall, F. Schott, J. Fischer, and A. Körtzinger (2008), Oxygen minimum zone in the North Atlantic south and east of the Cape Verde Islands, *J. Geophys. Res. 113*, C04014 17, 75, 77

Stramma, L., M. Visbeck, P. Brandt, T. Tanhua, and D. Wallace (2009), Deoxygenation in the oxygen minimum zone of the eastern tropical North Atlantic, *Geophys. Res. Lett. 36*, L20607 15, 75

Stramma, L., S. Schmidtko, L. A. Levin, and G. C. Johnson (2010), Ocean oxygen minima expansions and their biological impacts, *Deep-Sea Res. I*, *57*, 587–595 7, 74

Stramma, L., E. D. Prince, S. Schmidtko, J. Luo, J. P. Hoolihan, M. Visbeck, D. R. W. Wallace, P. Brandt, and A. Körtzinger (2012), Expansion of oxygen minimum zones may reduce available habitat for tropical pelagic fishes, *Nature Climate Change*, *2*, 33–37 8

Stramma, L., A. Oschlies, and S. Schmidtko (2012), Anticorrelated observed and modeled trends in dissolved oceanic oxygen over the last 50 years, *Biogeosciences Disc.*, *9*, 4595–4626 7

Sundermeyer, M. A., and J. F. Price (1998), Lateral mixing and the North Atlantic Tracer Release Experiment: Observations and numerical simulations of Lagrangian particles and a passive tracer, *J. Geophys. Res. 103*(C10), 21,481–21,497 45, 47

Sundermeyer, M. A., and M. P. Lelong (2005), Numerical simulations of lateral dispersion by the relaxation of diapycnal mixing events, *J. Phys. Oceanogr. 35*(C10), 2368–2386 47

Sverdrup, H. U. (1938), On the explanation of oxygen minima and maxima in the oceans, *J. Conseil Int. pour lExploration de Mer*, *13*, 163–172 5

Tanhua, T., K. A. Olsson, and E. Fogelqvist (2004), A first study of SF_6 as a transient tracer in the Southern Ocean, *Deep Sea. Res., II 51*, 2683–2699 16

Taylor, G. I. (1921), Diffusion by continuous movements, *Proc. London Math. Soc. 20*, 196-211

Toole,J. M., R. W. Schmitt, and K. L. Polzin (1994), Estimates of Diapycnal Mixing in the Abyssal Ocean, *Science 264*, 1120–1123 3, 13

Vaquer-Sunyer, R. and C. M. Duarte (2008), Thresholds of hypoxia for marine biodiversity, *Proc. Natl. Acad. Sci. USA*, *105*, 15452–15457 7, 73

Watanabe, Y. W., M. Wakita, N. Maeda, T. Ono, and T. Gamo (2003), Synchronous bidecadal periodic changes of oxygen, phosphate and temperature between the Japan Sea deep water and the North Pacific intermediate water, *Geophys. Res. Lett.*, *30*, 2273 7

Watson,A. J., and J. R. Ledwell (2000), Oceanographic tracer release experiments using sulphur hexafluoride, *J. Geophys. Res. 105*, 14,325–14,337 4, 14

Watson,A. J., M. J. Messias, E. Fogelqvist, K. A. Van Scoy, T. Johannessen, K. I. C. Oliver, D. P. Stevens, F. Rey, T. Tanhua, K. A. Olsson, F. Carse, K. Simonsen, J. R. Ledwell, E. Jansen, D. J. Cooper, J. A. Kruepke, and E. Guilyardi (1999), Mixing and convection in the Greenland Sea from a tracer-release experiment, *Nature 401*, 902–904 41

Whitney, F. A., H. J. Freeland, and M. Robert (2007), Persistently declining oxygen levels in the interior waters of the eastern subarctic Pacific, *Prog. Oceanogr.*, *75*, 179–199 7, 74

Wright, J. J., K. M. Konwar, and S. J. Hallam (2012), Microbial ecology of expanding oxygen minimum zones, *Nat. Rev. Microbiol.*, *10(6)*, 381–394 8, 73, 74

Wyrtki, K. (1962), The oxygen minima in relation to ocean circulation, *Deep-Sea Res.*, *9*, 11–23 5, 73

Wu, L., Z. Jing, S. Riser, and M. Visbeck (2011), Seasonal and spatial variations of Southern Ocean diapycnal mixing from Argo profiling floats, *Nature Geoscience 4*, 363–366 3, 13